

**SURFACE PROPERTIES OF NANOPORE-STRUCTURED METALS AND
OXIDES**

A Dissertation

by

SUNGHAN KIM

Submitted to the Office of Graduate and Professional Studies of
Texas A&M University
in partial fulfillment of the requirements for the degree of

DOCTOR OF PHILOSOPHY

Chair of Committee,	Hong Liang
Co-Chair of Committee,	Andreas A. Polycarpou
Committee Members,	Jun Zou
	Partha P. Mukherjee
Head of Department,	Andreas A. Polycarpou

May 2015

Major Subject: Mechanical Engineering

Copyright 2015 Sunghan Kim

ABSTRACT

The importance of understanding the properties of textured surfaces is growing with their potential wide engineering applications. In this thesis research, nanopore structures of metals and oxides were examined to determine the interactions between environmental objects and the textured surfaces. The major applications of nanopore structures are micro/nanoelectromechanical systems (MEMS/NEMS), energy devices, sensors, and environmental devices. In order to achieve better performance in each, it needs to consider three critical surface properties such as surface forces, electrochemical performances, and wettability. In this research, the surface properties of nanopore structures have been explored with understanding the essence of contact. This research uses experimental approach combined with basic analysis in physical principles.

Experiments include fabrication of nanopore structures, investigation of surface force, electrochemical evaluation, and wetting/electrowetting studies of nanopore structures. Metallic nanopore structures (MNSs) of nickel were characterized by using an atomic force microscope (AFM) and a triboscope. The mechanisms of bacteria desorption were examined by alumina nanopore structures (ANSs) with various pore sizes. The kinetics of ion-transfer on MNSs was studied using Electrochemical Impedance Spectroscopy (EIS) and Cyclic Voltametry (CV). The (electro-) wetting behavior of MNSs were examined using a droplet shape measurement system.

A physics based analysis was conducted in order to understand the principles of the nanopore effects on environments suitable for various applications. Results lead to

the successful identification of critical geometrical factors. A contact model has been established to understand properties of textured surfaces. Specific design factors, which are related to the geometry of the textured surfaces has been identified. This research revealed fundamental mechanisms of contact and establish a relationship between morphology/geometry and surface properties. The findings in this thesis research afford new approach to optimize applications of textured surface. The proposed contact models are beneficial to the surface design and application of sustainable micro/nanodevices.

This thesis includes eight chapters. The first chapter introduces the background and fundamental knowledge related to current research in order to understand the basics. Followed by the chapter two of motivation and objectives, chapter three discusses materials and experimental details, chapter four and five cover the surface forces, chapter six studies the electrochemical performances, chapter seven investigates the (electro-)wettability, and the conclusions and future recommendations are presented in chapter eight.

DEDICATION

To my beloved wife and to my parents.

ACKNOWLEDGEMENTS

First of all, I would like to thank my committee chair; Dr. Hong Liang for her dedicated help, guidance, encouragement and advice for all through my PhD courses. Her advice leads to all achievements of my research. All of my thought, critical ideas and scientific writing skill have been developed with her guide and support. I would also like to thank my co-chair; Dr. Andreas A. Polycarpou for his careful advice, consultation and support during my graduate study. He always gave me good comment for my future career plan. His advice and comment led me to achieve fruitful results. I am grateful to my committee members; Dr. Jun Zou and Dr. Partha Mukherjee for their valuable recommendation and support to my research.

I would also like to acknowledge the financial support from Texas A&M University, Texas Engineering Experiment Station, The Bill and Melinda Gates Foundation, and the National Institutes of Health. I am thankful to the Microscopy Image Center (MIC) at Texas A&M University for their material characterization service. Assistance provided by Dr. Jeffrey D. Cirillo is also greatly appreciated.

And I wish to thank all of my colleagues Dr. Joo, Dr. He, Dr. Xiao, Dr. Zhou, Mr. Hyunho Choi, and Mr. Kyungjun Lee for their assistance and help in my experiments. I also want to acknowledge all the members in Surface Science Group and in Micro Tribology Dynamics Research Group for their precious time for discussion in my study and research.

My appreciations also go to my friends and the department faculty members and

staff members for making my time at Texas A&M University a significant experience.

I would like to express my gratitude to my beloved wife, Jaeun Lee, for her dedicated and devoted support. Her understanding, encouragement, and consideration could have accomplished all my study. My beloved and precious sons, Hajoong and Euijoon, who make me happy and smile, I love you all.

I am deeply grateful to my parents for their endless love, confidence and pray for me and my family. I am also thank to all other family members for their support, encouragement, and warm words.

Finally, thank you God for your guidance and leading in my whole life. All of my purpose and life belong to you. You are my Lord, thank you God.

NOMENCLATURE

Acronyms

AFM	Atomic force microscope
ANS	Alumina nanopore structure
CV	Cyclic voltammetry
EIS	Electrochemical impedance spectroscopy
ESA	Effective surface area
FESEM	Field emission scanning electron microscopy
LB	Luria-Bertani
LbL	Layer-by-layered
LFM	Lateral force microscope
MNS	Metallic nanopore structure
NEMS	Nanoelectromechanical systems
OD	Optical density
PS-HPC	Polystyrene-based hierarchical porous carbon
TEM	Transmission electron microscopy
ZTC	Zeolite template carbon

Symbols

Chapter I

P	Applied load
K	Indentation modulus

A	Contact area
β	Conversion factor by type of indenter tip

Chapter IV

A_{eq}	Equivalent contact area
d	Pore diameter
a	Inter-pore distance
R	Radius of tip
E_1, E_2	Moduli of elastic
ν_1, ν_2	Poisson's ratios
c	Contact radius
P	Applied load
K	Indentation modulus
A	Hertzian contact area
P.O.	Surface porosity

Chapter V

$f(r)$	Ratio of unit area
l	Pore to pore (interpore) distance
r	Radius of a pore
S	Bottom area of bacteria
$F(r)$	Contact area
a	Semi-minor axis of bacteria cell
b	Semi-major axis of bacteria cell

Chapter VI

Γ	Effective surface area
r	radius of the pore
h	thickness of MNS
d	interpore distance

Chapter VII

θ^*	Apparent contact angle between a MNS and liquid droplet
S_1	Area of liquid-solid interface on a flat surface
S_1^*	Area of liquid-solid interface on a MNS
f_{l-s}	Area of liquid-solid from a nanopore shape
θ	Intrinsic contact angle between a flat surface and liquid droplet
S_2	Area of liquid-vapor interface on a flat surface
S_2^*	Area of liquid-vapor interface on a MNS
f_{l-v}	Area of liquid-vapor in a nanopore shape
r	Radius of a liquid droplet on a flat surface
r^*	Radius of a liquid droplet on a MNS
z	Shape correction factor
a	Pore-to-pore distance
d	Pore diameter
h	Absorption depth of a liquid droplet in the pore

t	Distance from the top to the bottom of the crown shape
P_0	Atmospheric pressure
γ	Surface tension of a substrate
L	Pore depth
V_{flat}	Volume of a liquid droplet on a flat nonporous surface
$V_{nanopore}$	Volume of a liquid droplet on a MNS
α	Volume correction factor
θ_e	Apparent contact angle with applied electrical potential
θ_0	Contact angle without applied electrical potential
C	Capacitance of the dielectric layer
V	Applied electrical potential
Ψ	$\cos\theta_e$
c_1	Constant which relates to both the capacitance of the dielectric layer and the surface tension of the MNS
κ, α, β	Coefficients which correspond to the pore size of the MNS

TABLE OF CONTENTS

	Page
ABSTRACT	ii
DEDICATION.....	iv
ACKNOWLEDGEMENTS	v
NOMENCLATURE	vii
LIST OF FIGURES.....	xiv
LIST OF TABLES.....	xviii
CHAPTER I INTRODUCTION	1
1.1.Nanopore structures of materials.....	1
1.1.1.Morphology of material surfaces	2
1.1.2. Definition of nanopore structures.....	2
1.1.3. Fabrication.....	3
1.1.4. Properties and applications.....	4
1.2. Characteristics of nanopore structure	6
1.2.1. Surface force	6
1.2.1.1. Measurement of adhesive (pull-off) force by AFM	8
1.2.1.2. Measurement of friction force by AFM	9
1.2.1.3. Indentation modulus for surface force	10
1.2.1.4. Bacterial adhesion	11
1.2.2. Electrochemical behavior	12
1.2.2.1. Surface morphology effect to electrochemical behavior.....	13
1.2.2.2. Modification surface area for electrochemical behavior	13
1.2.3. Wettability	14
1.2.3.1. Wetting models.....	14
1.2.3.2. Electrowetting effect	15
1.3. Summary	17
CHAPTER II MOTIVATION AND OBJECTIVES	18
2.1. Investigation of the surface forces of ANS-based nanopore structures	19
2.2. Evaluation and understanding of electrochemical performance of nanopore structures	20
2.3. Determining the wetting/electrowetting mechanism of nanopore structures.....	20
2.4. Defining essential geometrical factors to optimize the surface properties of	

nanopore structures.	21
CHAPTER III MATERIALS AND METHODS	22
3.1. Fabrication of materials.....	22
3.1.1. Alumina based nanopore structure (ANS)	22
3.1.2. Metallic nanopore structure (MNS)	24
3.2. Characterization	26
3.3. Surface force investigation.....	27
3.4. Electrochemical evaluation	29
3.5. Wetting/electrowetting study	31
CHAPTER IV SURFACE FORCES, PART I: ELECTRICAL-POTENTIAL INDUCED TRIBOLOGICAL PERFORMANCE	32
4.1. Effect of electrical potential on surface morphology	32
4.2. Effect of electrical potential on tribological performance.....	37
4.3. Effects of electrical potential on indentation modulus.....	43
4.4. Summary	47
CHAPTER V SURFACE FORCE PART II: INFLUNCE OF NANOPORES ON BACTERIA.....	48
5.1. Morphological characteristics	48
5.2. Contact area calculation between bacteria and ANS.....	51
5.3. Number of bacterial cells on ANS.....	54
5.4. Analysis of bacterial adhesion and repelling force.....	55
5.5. Summary	59
CHAPTER VI ELECTROCHEMICAL PROPERTIES OF NANOPORE STRUCTURES AND THEIR INFLUENCE ON ION-TRANSFER	60
6.1. Morphological analysis	60
6.2. Cyclic voltammetry (CV) study	61
6.3. Identifying electrochemical double layer on MNS	63
6.4. Calculation effective surface area	65
6.5. Electrochemical impedance spectroscopy (EIS) analysis	68
6.6. Summary	75
CHAPTER VII (ELECTRO-)WETTING BEHAVIOR.....	76

7.1. Wettability of MNS via pore size	76
7.2. Numerical analysis of wettability on MNS	78
7.3. Electrowettability of MNS via pore size	84
7.4. Summary	94
CHAPTER VIII CONCLUSIONS AND FUTURE WORKS	96
8.1. Conclusions	96
8.2. Future works.....	99
REFERENCES	100

LIST OF FIGURES

	Page
Figure 1.1. SEM images of alumina nanopore structure (ANS): (a) SEM top view image of ANS, (b) SEM cross section view image of ANS.	4
Figure 1.2. Major categories application and three critical surface properties of nanopore structure.	5
Figure 1.3. Adhesive force (pull-off force) characterization by AFM: (a) schematic diagram of AFM, (b) schematic process of adhesive force (pull-off force) experiment by AFM.....	8
Figure 1.4. Friction signal investigation by AFM: (a) schematic diagram of LFM mode, (b) typical friction signal measurement diagram.	9
Figure 1.5. Schematic diagram of typical load-displacement curve during an indentation experiment.	10
Figure 1.6. Schematic diagram of electrowetting effect: a) before applying electrical potential and b) after applying electrical potential.	16
Figure 2.1. Research flow chart.	19
Figure 3.1. Overall process schemes for ANS fabrication.	23
Figure 3.2. Fabrication process of a MNS by using ANS.	26
Figure 3.3. Schematic electrical circuit set-up for applying electrical potential into the metallic nanopore structure. Reproduced from ‘S. Kim, A.A. Polycarpou, and H. Liang, Active control of surface forces via nanopore structures, APL materials, Vol. 1, Issue 3, 2013’ with permission from AIP (Copyright © 2013).	28
Figure 3.4. Schematic diagram of experimental set-up for bacterial repelling experiment.....	29
Figure 3.5. Schematic experimental setup for electrochemical evaluation of MNSs.	30
Figure 3.6. Illustration experimental setup for wetting/electrowetting on MNS: a) scheme of the liquid droplet shape measurement system, b) schematic electrowetting experiment setup by using MNS.	31

Figure 4.1. AFM height images about MNS with various electric potential energy from 0 to 800 mV. White circles highlight the same area in various electric potential conditions and white lines are for profile checking regions. Horizontal scanning distance is 5.55 μm . The scale bar represents height level of MNS from 0 to 600 nm.	33
Figure 4.2. MNS profiles which are represented by white lines in Figure 2 with 0 mV and 800 mV applied electrical potential conditions.	34
Figure 4.3. Percent of over 350 nm height region with electrical potential applying from AFM height image.	35
Figure 4.4. AFM phase images about MNS with various electric potential energy from 0 to 800mV. Horizontal scanning distance is 5.55 μm . The scale bar represents phase-shift signal of MNS from 0 to 6000 mV.	36
Figure 4.5. Electrical potential activated pull-off force with various MNS samples. Each bar represents average value of pull-off force and error bars show standard deviation with one sigma.	38
Figure 4.6. Electrical potential activated friction signal with various MNS samples. Each bar represents average value of friction signal and error bars show standard deviation with one sigma.	41
Figure 4.7. SEM images of the conical indenter tip: a) top view of the conical tip, b) side view of the conical tip.	44
Figure 4.8. Load and indentation depth curves for MNSs with various pore sizes.	45
Figure 4.9. Indentation modulus against application of electrical potential in MNSs with various pore sizes.	46
Figure 5.1. Atomic force microscope (AFM) images of alumina nanopore structure (ANS) with various pore diameters: The pore diameters are about: (a) 35 nm, (b) 55nm, (c) 70 nm, and (d) 80 nm.	49
Figure 5.2. Atomic force microscope (AFM) images of bacterial cells on alumina nanopore structure (ANS, pore diameter: 55 nm) (a) 2-dimensional height mode AFM image of bacterial cells on the ANS, (b) zoomed in 3-dimensional height mode AFM image of single bacterial cell on the ANS, (c) 2-dimensional phase mode AFM image of bacterial cells on the ANS, and (d) 3-dimensional phase mode AFM image of bacterial cells on the ANS.	51

Figure 5.3. Schematic diagram to define the contact area between a bacterial cell and alumina nanopore structure (ANS). The extracted atomic force microscope (AFM) image of ANS (pore diameter: 80 nm) shows the hexagonal shape unit area.	53
Figure 5.4. Optical microscope images of bacterial cells on the alumina nanopore structure (ANS) with various pore diameters. Black color represents bacterial cells. Top images stem from before repelling experiment and bottom images stem from after repelling experiment. The scale bar in each image represents 100 μm	54
Figure 5.5. Percentage of adhered bacterial cells on alumina nanopore structure (ANS) and the contact angle via pore size. The inset graph shows a relation between the pore size and the contact area. The contact area decreased with pore size increase. Left side y-axis represents the result of bacteria repelling experiment. Right side y-axis indicates the result of contact angle measurement. Arrows designate each assigned y-axis. Error bars show standard deviation with one sigma.	57
Figure 6.1. SEM images of MNS with various pore diameters: the pore diameter are about (a) 168 nm, (b) 253 nm, (c) 348 nm. The cross section view of 348 nm pore size MNS is on image (d).	61
Figure 6.2. Cyclic voltammetry curves of MNS with various pore size: 168 nm, 253 nm, and 348 nm 1M potassium hydroxide (KOH) as an electrolyte.	62
Figure 6.3. Schematic diagram of electrochemical double layer at the MNS and electrolyte interface.	65
Figure 6.4. Schematic diagram of the effective surface area (Γ : ESA) for electrochemical reaction on the MNS.	67
Figure 6.5. Electrochemical impedance spectroscopy (EIS) data with Nyquist plots of MNS with various pore size: 168 nm, 253 nm, and 348 nm in the 1M potassium hydroxide (KOH) as an electrolyte.	69
Figure 6.6. Electrochemical impedance spectroscopy (EIS) data with both a) bode impedance plots and b) bode phase plots of the MNS with various pore diameters: 168 nm, 253 nm, and 348 nm.	71
Figure 6.7. TEM images of single pore in (a) porous alumina and (b) MNE.	72
Figure 6.8. Nyquist plots of aluminum based metallic micropore electrode with various pore size: 120 μm , 240 μm , and 350 μm in the 1M potassium hydroxide (KOH) as an electrolyte. (Inset image scale bar: 300 μm).	73

Figure 6.9. Observed current-voltage curves of the MNS with various pore diameters: 168 nm, 253 nm, and 348 nm in the 1M sodium chloride (NaCl) electrolyte.	74
Figure 7.1. SEM images of MNS with various pore sizes: (a) 154 nm pore size, (b) 258 nm pore size, and (c) 379 nm pore size.....	77
Figure 7.2. Intrinsic contact angle of MNS with 2ul water droplet on top surface of MNS. Error bars show standard deviation with one sigma. Error bars show standard deviation with one sigma.	78
Figure 7.3. Schematic diagram of a liquid droplet's geometries (a) on a flat nonporous surface, (b) on a MNS, and (c) in a MNS; (d) represents the unit area of the MNS.....	80
Figure 7.4. SEM image and schematic diagram for calculating the area of the liquid-solid interface at the nanopore shape and the area of liquid-vapor interface in the nanopore shape. The SEM image in a) shows a cross-section of a MNS, and b) is the geometry of cross-section of a pore shape.	81
Figure 7.5. Comparison of the simulation and experiment results for contact angle determination across various pore sizes.	84
Figure 7.6. The contact angle alteration with applying electrical potential in various pore size of MNS. Error bars show standard deviation with one sigma.....	85
Figure 7.7. Ψ ($\cos \theta$) using contact angle of water droplet on the MNS as a function of the applied electrical potential. Each solid dot represents the results from experiments and each dash line demonstrates the calculated results by using modified electrowetting equation for MNS.	89
Figure 7.8. Schematic expression the electrowetting mechanism of MNS. a) electrowetting experiment on flat (no pore) surface, b) electrowetting experiment on MNS surface, and c) the electrowetting balance model at the pore.	91
Figure 7.9. The depth of water droplet penetration with applying electrical potential for various pore size of MNS.....	92
Figure 7.10. The plot of contact diameter against the applied electrical potential with various pore size.	94
Figure 8.1. Various contact modes in nanopore structures.	97

LIST OF TABLES

	Page
Table 1.1. List of typical models and equations about the surface properties.	7
Table 5.1. Average (Avg) pore diameter of alumina nanopore structure (ANS) and the corresponding Contact area with unit area ratio.	53
Table 5.2. Percentage of adhered bacterial cells before and after repelling experiment on various pore size of the ANS	56
Table 6.1. Calculated effective surface area (Γ : ESA) and corresponding total surface area of MNS with various pore diameters.....	68
Table 7.1. Value of variables for determining the contact angle of a MNS.....	83
Table 7.2. Value of κ , α and β coefficients for determining the MNS's modified electrowetting equation in terms of pore size of MNS.	87

CHAPTER I

INTRODUCTION

This chapter introduces the basic knowledge behind the current research. This thesis research focuses on design, performance, and potential applications of nanopore structures. The background of nanopore structures is briefly discussed in the first part. The fundamental principles of surface properties of nanopore structures are discussed in the second part. It covers basic knowledge in surface forces, electrochemical behaviors, and the fundamental of wettability. This chapter closes including short summary and brief introduction of following chapters.

1.1. Nanopore structures of materials

Nanostructures, including nanoscale features in microscale structures, have attracted great attention in recent years. This is because nanostructures have the potential to be sufficient the basis for various engineering applications due to their favorable strength, remarkable catalytic properties, and excellent electrical properties¹⁻³. In terms of shape of nanostructure, three-dimensional nanopore structures are particularly interesting due to their unique properties and numerous engineering applications⁴⁻⁷. In this section, fundamental properties and applications of nanopore structure will be introduced.

1.1.1. Morphology of material surfaces

As structured materials' properties can be modified according to their features, surface morphology is a critical parameter in determining materials' surface properties⁸⁻¹⁰. Because it is possible to manipulate the surface properties of materials by altering the surface morphology¹¹⁻¹³, it is important to understand the correlation between a surface's morphology and its properties when designing and fabricating materials for specific purposes.

In order to systematically control surface properties, the surface morphology of a material should be designable and adjustable. In other words, materials with methodically alterable surface morphology are suitable to use as base materials for optimizing surface properties.

1.1.2. Definition of nanopore structures

Nanopore structures have nanoscale pores in their surfaces. Nanopore structures are extensively studied in various research areas, in keeping with their unique and critical properties: a size comparable to nanoscale structures, porous materials having a high surface-area-to-volume ratio, and a type of three-dimensional structure that features architectural rigidity [14-16].

1.1.3. Fabrication

During the last decade, there have been many advances in designing and fabricating nanopore structures. In terms of conceptual design, the shape of nanopore structures could be controlled and uniformly distributed. Yet, it was difficult to uniformly control the shape of nanopore in large areas. This issue could be overcome by developed nanofabricating technologies such as electron beam lithography, nanoimprinting, focused ion beam milling, etc ¹⁴⁻²¹. However, most of developed fabricating technologies have some drawbacks; they are expensive, difficult and complicated, have a low productivity. Alumina nanopore structures (ANS) have been widely used to overcome the challenges. The ANS has benefits for its applications. The advantages of ANS are: a simple fabrication process, highly productive and costly effective, isolated straight channels with high aspect ratios, a tunable pore diameter and depth with large area, etc. It is possible to fabricate highly ordered nanopore structures that are called ANS using a two-step, aluminum, anodizing method ^{22, 23}. The pore diameter of ANS can be manipulated from 10 nm to 450 nm. The interpore distance can be tuned from 25 nm to 500 nm. The thickness of ANS can be extended up to 700 μm . The morphology of the ANS surface can be systematically controlled by electrochemical conditions. Figure 1.1 shows typical shape of the ANS. The ANS is used as a typical nanopore structure itself. It can also be used as a template to fabricate other types of nanopore structures. Using ANS as a template, it is possible to fabricate highly-ordered three-dimensional metallic nanopore structure (MNS). Due to the advantageous features of the ANS, this research focuses on ANS-based nanopore structures. Two types

of ANS-based nanopore structures have been used for this research. One is the ANS itself and the other one is MNS. In such ANS and MNS structures fabricated from ANS have the potential to provide a satisfactory basis for various engineering applications.

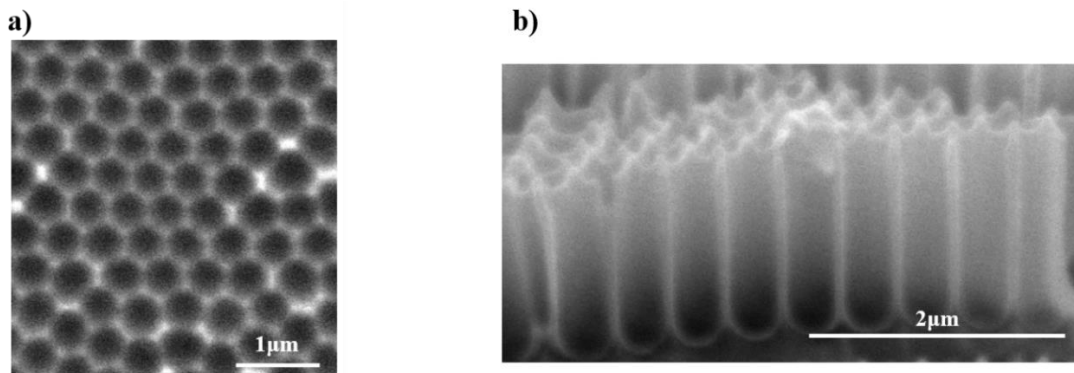


Figure 1.1. SEM images of alumina nanopore structure (ANS): (a) SEM top view image of ANS, (b) SEM cross section view image of ANS.

1.1.4. Properties and applications

Four major categories in application of nanopore structures are summarized as shown in Figure 1.2²⁴⁻³⁰. Those are energy devices, sensors, environmental devices, and MEMS/NEMS. For better performance of each application, three critical surface properties need to be considered: surface force, electrochemical performance and wettability.

The durability of nanopore structures has been a problem for further improvement due to their unexpected interfacial failures. To eliminate such interface failures, the surface forces, which are pull-off force, friction force, and wear (scratch)

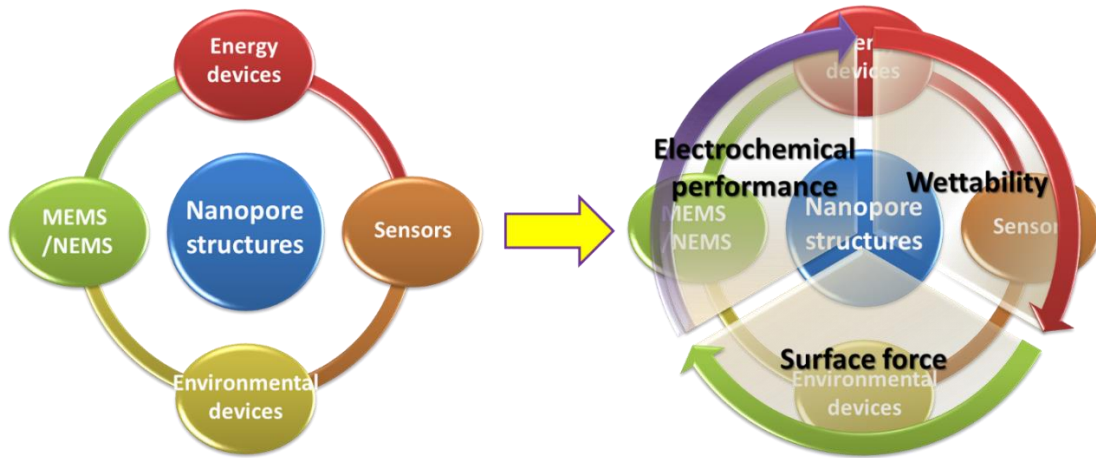


Figure 1.2. Major categories application and three critical surface properties of nanopore structure.

resistance, of nanopore structure should be studied ³¹⁻³⁵. In terms of biocompatibility, the cell adhesion on surfaces should be investigated as one type of surface force ³⁶⁻³⁸. In order to establish enhanced electrochemical performance, the electrochemical property of nanopore structures should be considered. Electrochemical behavior such as charge density and ion transfer can characterize the performance of electrochemical reaction for energy storages, double layer capacitors, etc ³⁹⁻⁴¹. Wettability is a critical surface property for identification surface energy that is an important design parameter for sensors and environmental devices ⁴²⁻⁴⁴. According to the Young-Dupre's equation, the contact angle can represent the level of surface energy; a lower contact angle indicates higher surface energy and a higher contact angle signifies lower surface energy ⁴⁵. Understanding surface properties is important for better design and fabrication of nanopore structures.

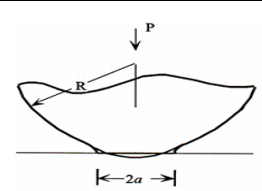
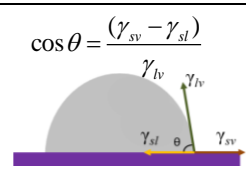
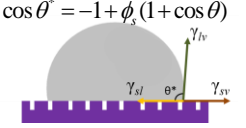
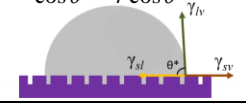
1.2. Characteristics of nanopore structure

There are classic theories and equations for each surface property. Since Hertz contact theory introduced the typical contact model for understanding surface forces ⁴⁶, a variety of modified contact theories such as JKR theory ⁴⁷ and DMT theory ⁴⁸ have been developed. The correlation between a surface energy and a contact angle is defined by Young's equation ⁴⁹, the Cassie-Baxter model ⁵⁰, and the Wenzel model ⁵¹ to characterize a surface wettability. Using the Cottrell equation ⁵² and the Randles–Sevcik equation ⁵³, it is possible to estimate the electrochemical property of a target material ⁵⁴⁻⁵⁷. Table 1.1 shows the list of typical models and equations about surface properties. These typical models are useful to predict and comprehend the performance of each surface property.

1.2.1. Surface force

The durability of nanostructure-based devices has been a bottleneck for further development due to their unexpected interfacial failures. To eliminate such interface failures, the tribological properties of nanostructured devices are needed for design and fabrication [26-28, 30, 50, 51]. The atomic force microscope (AFM) and nanotriboscope are commonly used for measuring tribological properties such as adhesion and friction at the nanometer scale [52-55]. Moreover, understanding the bacterial adhesion is important to fabricate biocompatible structures, the behavior of bacterial adhesion has been widely examined through a shear stress experiment ^{58, 59}.

Table 1.1. List of typical models and equations about the surface properties.

Surface Property	Typical theory	Representative equation	Terminology	
Surface Force	Hertz contact theory	$a^3 = \frac{PR}{K} \frac{1}{R} = \frac{1}{R_1} + \frac{1}{R_2} \frac{1}{K} = \frac{3}{4} \left[\frac{1-\nu_1^2}{E_1} + \frac{1-\nu_2^2}{E_2} \right]$	 <p> R_1, R_2: radius of each object ν_1, ν_2: Poisson's ratios of each object E_1, E_2: elastic modulus of each object P: applied force P_s: adhesive force γ: surface energy </p>	
	JKR theory	$a^3 = \frac{R}{K} \left[P + 3\pi R\gamma + \sqrt{6\pi R\gamma P + (3\pi R\gamma)^2} \right]$		
	DMT theory	$P_s = -\frac{3}{2}\pi R\gamma$ $a^3 = \frac{(P + P_s)R}{K}$ $P_s = -2\pi R\gamma$		
Wettability	Young's equation	$\cos \theta = \frac{(\gamma_{sv} - \gamma_{sl})}{\gamma_{lv}}$ 	γ_{sv} : surface energy of solid–vapor phase γ_{sl} : surface energy of solid–liquid phase γ_{lv} : surface energy of liquid–vapor phase	
	Cassie-Baxter model	$\cos \theta^* = -1 + \phi_s (1 + \cos \theta)$ 		θ^* : apparent contact angle θ : equilibrium contact angle ϕ_s : the fraction of the solid in contact with the liquid
	Wenzel model	$\cos \theta^* = r \cos \theta$ 		
Electrochemical Property	Cottrell equation	$i = \frac{nFAc_j^0 \sqrt{D_j}}{\sqrt{\pi t}}$	i = current n = number of electrons F = Faraday constant A = area of the (planar) electrode c_j^0 = initial concentration of the reducible analyte j D_j = diffusion coefficient for species j t = time i_p = current maximum in amps	
	Randles-sevcik equation	$i_p = 0.4463 nFAc \left(\frac{nFvD}{RT} \right)^{1/2}$	n = number of electrons transferred F = Faraday constant A = area of the (planar) electrode T = temperature D = diffusion coefficient for species j C = concentration v = scan rate	

1.2.1.1. Measurement of adhesive (pull-off) force by AFM

The adhesive force at the interface between two objects can be measured by the force-displacement curve using AFM. Figure 1.3 shows a schematic diagram of AFM and a plotted graph of a typical force-displacement curve.

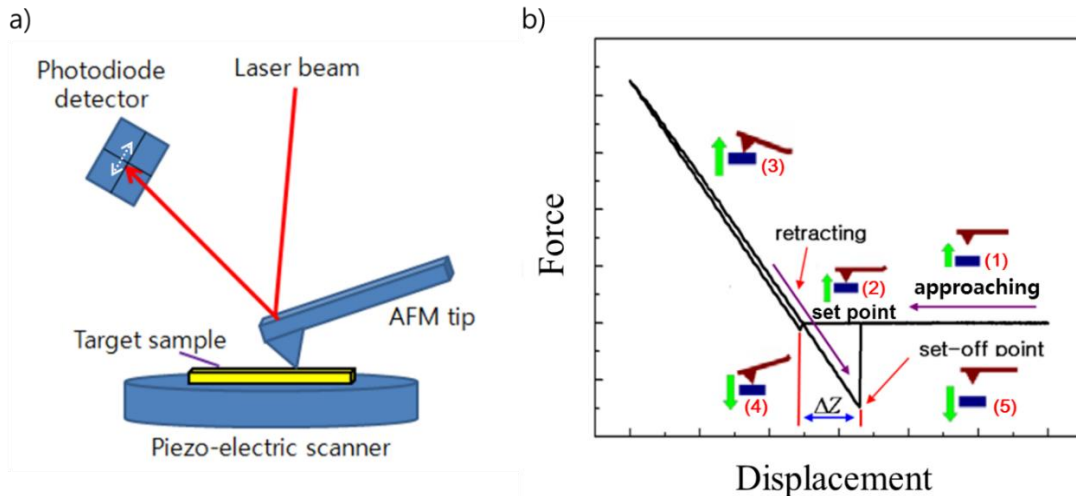


Figure 1.3. Adhesive force (pull-off force) characterization by AFM: (a) schematic diagram of AFM, (b) schematic process of adhesive force (pull-off force) experiment by AFM.

While performing the force-displacement experiment function, a laser beam is reflected onto the AFM tip and then detected by the photodiode detector in one direction (top to bottom). The process by which the substrate and the AFM tip approach one another involves an increase in force from steps (1) to (3). After the approaching process, retraction proceeds with a decreasing force value from steps (4) to (5). During these approaching and retracting processes, it is possible to measure the displacement (ΔZ) between the AFM tip set point and set-off point. The adhesive force (pull-off force) can be evaluated according to the product of the ΔZ and the spring constant of AFM

cantilever.

1.2.1.2. Measurement of friction force by AFM

By using lateral force microscope mode (LFM) in AFM, the friction behavior of nanostructure can be examined. Figure 1.4 represents the schematic of LFM mode and the typical friction signal measurement diagram. During lateral scanning from left-to-right, the AFM cantilever can be twisted due to a sudden peak in the surface structure. This twisting motion can generate two lateral force signals: trace and retrace. These signals are recorded by the photodiode detector of AFM in one direction (left to right). Using the gap of friction signal between trace and retrace ($\Delta F.S$), it is possible to determine the frictional force of the surface ⁶⁰.

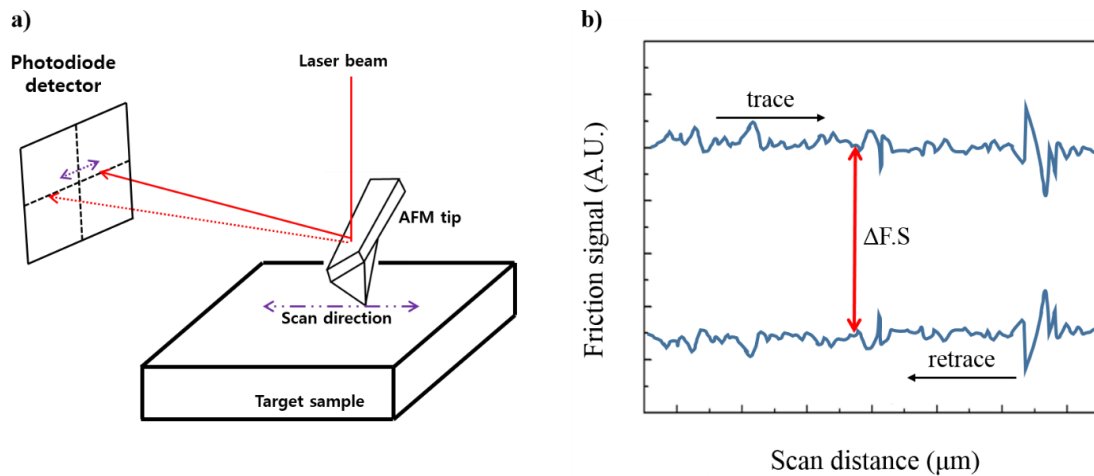


Figure 1.4. Friction signal investigation by AFM: (a) schematic diagram of LFM mode, (b) typical friction signal measurement diagram.

1.2.1.3. Indentation modulus for surface force

In order to understand the surface forces of nanostructures, the indentation modulus should be considered in defining the contact area between two surfaces. Previously presented contact models are focused on defining the contact area, including the indentation modulus. The indentation modulus can be obtained through indentation experiments ⁶¹. Figure 1.5 demonstrates a typical load-displacement curve during an indentation experiment.

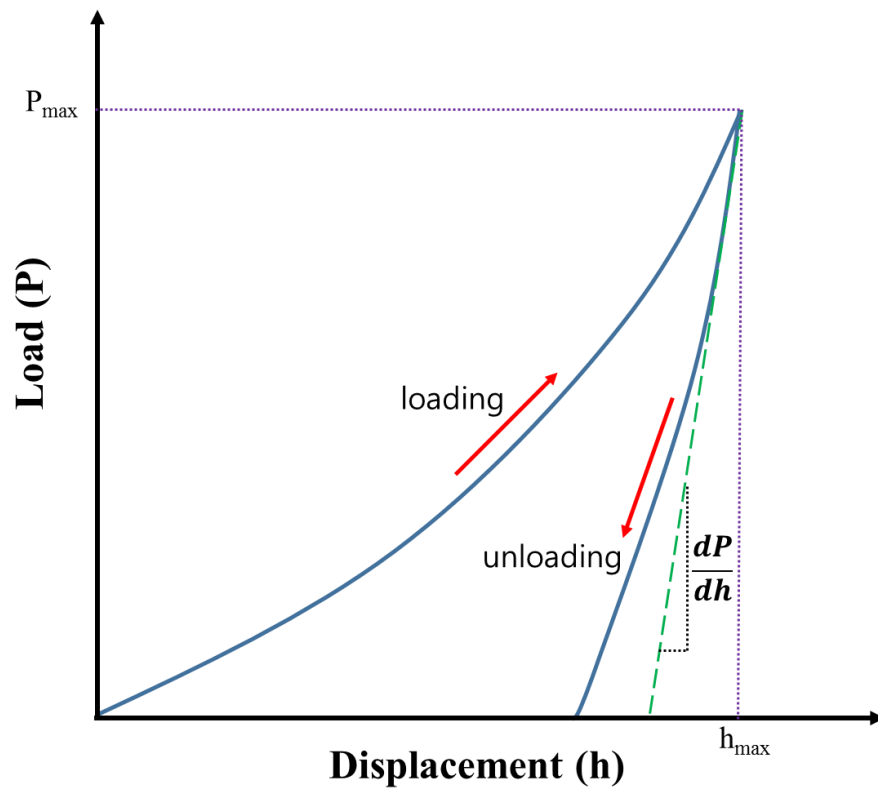


Figure 1.5. Schematic diagram of typical load-displacement curve during an indentation experiment.

The indentation modulus can be determined from the unloading stiffness. The unloading stiffness is expressed by following equation:

$$K = \frac{1}{\beta} \frac{\sqrt{\pi}}{2} \frac{\left(\frac{dP}{dh}\right)}{\sqrt{A}} \quad (1-1)$$

where P is the applied load, h is the indentation displacement, K is the indentation modulus, and A is the contact area. From the equation (1-1), the indentation modulus is specified by following equation:

$$\frac{dP}{dh} = \frac{2}{\sqrt{\pi}} K \sqrt{A} \quad (1-2)$$

where β is the conversion factor by type of indenter tip; $\beta = 1.000$ for flat and cylindrical indenter tips, $\beta = 1.012$ for Vickers indenter tip, $\beta = 1.034$ for Berkovich indenter tip, and $\beta = 1.08$ for conical indenter tip⁶²⁻⁶⁶.

1.2.1.4. Bacterial adhesion

Bacterial cells persist in numerous environments where humans live, including our food and bodies, among many others. They attach to various kinds of surfaces and grow well on them. Having bacterial free surfaces is an important component of not only keeping our daily life healthy and clean^{67, 68} but also providing better medical treatments^{69, 70}. Infection is often due to bacterial adhesion on medical implant materials such as orthopedic joint prosthetics and artificial dental implants. Minimizing the risk of infection is a hot issue for medical professionals^{71, 72}. In the case of surgery, bacterial

adhesion is also serious. A surgeon can spread bacterial cells due to their adherence to surgical instruments and the patient during surgery^{73,74}. Many research groups state that surface texturing can manipulate the cell adhesion⁷⁵⁻⁷⁷. Jiang et. al. reported that increasing surface area can assist cell contact and it can enhance the cell adhesion on the substrate⁷⁸. Xu et al. demonstrated that a surface having a sub-bacterial size texturing can decrease a prevalence of bacterial cells on the surface due to the decrease in the accessible surface area⁷⁹. The adhesive force between bacteria cell and surface could be reduced by decreasing the area of contact⁸⁰.

1.2.2. Electrochemical behavior

The electrochemical behavior of the nanostructure can be investigated by various types of nanostructures. The evaluation of electrochemical behavior; ion transfer and energy storage can be examined by electro-potential stat. These experiments can be characterized using a three-electrode cell setup including a reference electrode, a counter electrode, and a working electrode in an electrolyte. The cyclic voltammetry (CV) measurement has been widely used for kinetics studies in electrochemical reactions⁸¹⁻⁸³. The CV diagrams represent ion formation in electrode and migrate to electrolyte and vice versa. The anodic and cathodic limits shown in the CV diagrams will be observed in an ionic liquid due to the electrochemical reaction^{84,85}. In order to understand the impedance data of the nanostructure as the working electrode, the Nyquist plot and Bode plot can be obtained from electrochemical impedance spectroscopy (EIS) measurement. The Nyquist and Bode plots can be used to determine electrochemical impedance

through the plotted curve ⁸⁶⁻⁸⁸. The potentiodynamic experiment can determine the relation between the applied potential and the responding current density (Tafel curve).

1.2.2.1. Surface morphology effect to electrochemical behavior

Understanding the surface morphology of solid electrodes is important for designing better electrochemical devices such as electrochemical double layer capacitors, batteries, fuel-cells and sensors ^{41, 89-91}. Through manipulating the surface morphology, it is possible to enhance the kinetics of electrochemical reactions at the interface between the electrode and the electrolyte solution. One of the major factors affecting the kinetics of the electrochemical reaction is ion transfer at the interface of an electrode and the electrolyte. Improving ion (or charge) transfer is desirable to enhance the performance of electrochemical devices ⁹²⁻⁹⁴. Modification of the surface of electrodes continues to be a major challenge ⁹⁵. Increasing the surface area of electrodes through surface modification makes it possible to reduce their resistance ⁹⁶⁻¹⁰⁰. This can boost the ion transfer by making the redox behavior more reactive at the interface.

1.2.2.2. Modification surface area for electrochemical behavior

Reports have been found in specific modification of the surface area ¹⁰¹⁻¹⁰³. Fabrication of electrodes with large surface area has been seen promising. Lee et al. ¹⁰⁴ reported that the layer-by-layered (LbL) carbon-based-nanostructured electrodes can enhance the power of batteries by reducing the ion transfer resistance resulting reduced ion-diffusion time. Nishihara et al. ¹⁰⁵ showed that zeolite template carbon (ZTC) which

has three-dimensionally-ordered-microporous structure can reduce ion transfer resistance. Xu et al.¹⁰⁶ reported that polystyrene-based hierarchical porous carbon (PS-HPC) is able to facilitate fast ion transfer with larger ion accessible surface area. Moreover, many researchers make great effort to fabricate the porous type electrodes, which have high surface area for enhancing electrochemical reactions¹⁰⁷⁻¹⁰⁹. The large surface area can improve the electrochemical response at the interface between the electrode and electrolyte; it can reduce the resistance of ion transfer. Once the pores form on the electrode, the overall surface area of electrode is increased but there is no fundamental design criteria for obtaining the largest surface area.

1.2.3. Wettability

Understanding the wetting characteristic of surfaces is important for microfluidics, self-cleaning surfaces, anti-icing surfaces, bio-sensors, and filtrations¹¹⁰⁻¹²⁰. A substrate which has low surface energy will have a high contact angle with deionized water, and a high surface energy of certain substrate will have a small contact angle¹²¹. This means that the contact angle can represent the degree of surface energy of a substrate. From the contact angle measurement on the nanostructure, it is possible to see how the type of nanostructure affects to the surface wettability¹²².

1.2.3.1. Wetting models

Young's wetting model explains wettability of flat surface including a liquid

droplet⁴⁹. The surface roughness is crucial factor to explain the wetting characteristic of surfaces. Cassie-Baxter and Wenzel model have been widely used to anticipate the wetting characteristic^{50, 51, 123}. Cassie-Baxter model is mainly suitable to clarify heterogeneous wetting state which has air gap between a liquid droplet and a surface. Wenzel model is applicable to figure out the homogeneous wetting state that has full liquid-solid contact without air gap.

To characterize a surface wettability, the correlation between a surface energy and a contact angle is defined by those three wetting models: Young's model, the Cassie-Baxter model, and the Wenzel model. According to both the Cassie-Baxter model and the Wenzel model, the contact angle is determined by the surface fraction of the solid in contact with the liquid and the surface roughness. It means that the two parameters, contact angle and apparent contact area, can be affected by surface morphology. The relationship between contact angle and apparent contact area in terms of surface morphology can be used as a critical design parameter for surface wettability. In order to define the wetting behavior of a nanostructure, the wettability should be characterized by contact angle measurement with a liquid droplet on the top surface of the nanostructure.

1.2.3.2. Electrowetting effect

Based on the electrowetting effect, it is possible to control surface wettability by applying electrical potential to a metallic electrode or dielectric material coated electrode¹²⁴. Figure 1.6 shows typical electrowetting effect on a surface. This electrowetting

technology has been used to manipulate the surface tension for controlling the contact angle between a liquid droplet and a surface in various applications: pH-filters ¹²⁵, oil-water mixtures ¹²⁶, liquid droplet actuators ^{127, 128}, liquid lenses ¹²⁹, and display devices ¹³⁰.

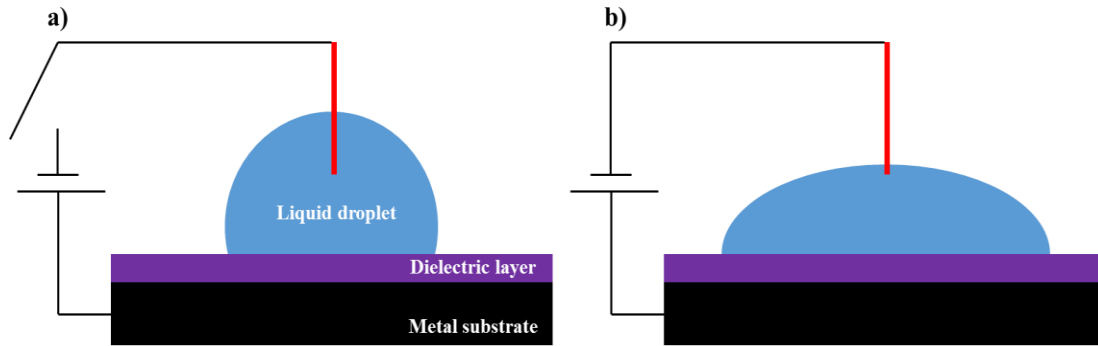


Figure 1.6. Schematic diagram of electrowetting effect: a) before applying electrical potential and b) after applying electrical potential.

The electrowetting effect has long been demonstrated on planar surfaces, but recently many researchers have performed electrowetting research on micro/nanotextured surfaces ¹³¹⁻¹³³. Under electrowetting conditions, it is possible to switch the wettability from hydrophobic to hydrophilic by texturing surfaces characterized by hydrophobicity ¹³⁴. Most textured surfaces for electrowetting applications are micro/nanoscale pillar shape-based structures ^{131, 133, 135}. Hydrophobicity of micro/nanoscale pillar structures results from decreasing the contact diameter between a liquid droplet and a surface structure, creating an air gap under the liquid droplet ^{131, 135}. The fundamental mechanism of electrowetting on textured surfaces has been

reported in studies on pillared structures¹³⁴. Young–Lippmann model is widely used to understand electrowettability¹³⁶⁻¹³⁸. In electrowetting conditions, the wettability between a liquid droplet and hydrophobic surface can be altered by applying electrical potential from the Cassie-Baxter model to the Wenzel model^{131, 135, 139}. These typical models are useful in predicting and comprehending the performance of any given surface’s wetting/ electrowetting property.

1.3. Summary

Fundamental background on surface properties and the applications of nanopore structures have been discussed, including classic theories and models. The advantages of nanopore structures and fabrication methods have also been discussed. The fundamental information on major surface properties such as surface force, electrochemical behavior, and wettability has been reviewed for deeper understanding of nanopore structures’ characteristics.

The following chapters will discuss this research in detail. Chapter 2 deals with the motivation behind this research and its objectives. The materials and experimental methods will be described in Chapter 3, along with theoretical background. The surface forces of nanopore structure will be demonstrated in Chapters 4 and 5. Chapter 6 will examine the performance of ion-transfer, one of the electrochemical properties of nanopore structures. Wettability and electrowettability of nanopore structures will be examined in Chapter 7. Finally, Chapter 8 will summarize the findings of this study and suggest future tasks and research directions.

CHAPTER II

MOTIVATION AND OBJECTIVES

As discussed in Chapter I, the surface properties of materials are largely dependent on their morphology. Nanopore structures can be fabricated by using alumina nanostructures (ANSs), which have a controllable fabrication process. Although ANSs could be widely used to fabricate highly ordered nanopore structures, knowledge of the correlation between ANS and surface properties is still lacking. Furthermore, critical design factors for ANS-based devices are still not well understood. In order to develop beyond the current status quo, geometrical factors able to optimize and functionalize ANS-based nanopore structures need to be established.

It is hypothesized here that, with the development of the requisite geometrical factors and a fuller understanding of the surface properties, nanopore structures could be used in the development of biological, electrochemical, environmental and tribological applications. Towards this goal, this research study will focus on ANS-based nanopore structures and three of their critical surface properties: surface force, electrochemical performance, and wettability. This thesis has four crucial objectives. To achieve these objectives, the research approaches in the research flow chart shown below in Figure 2.1 will be followed.

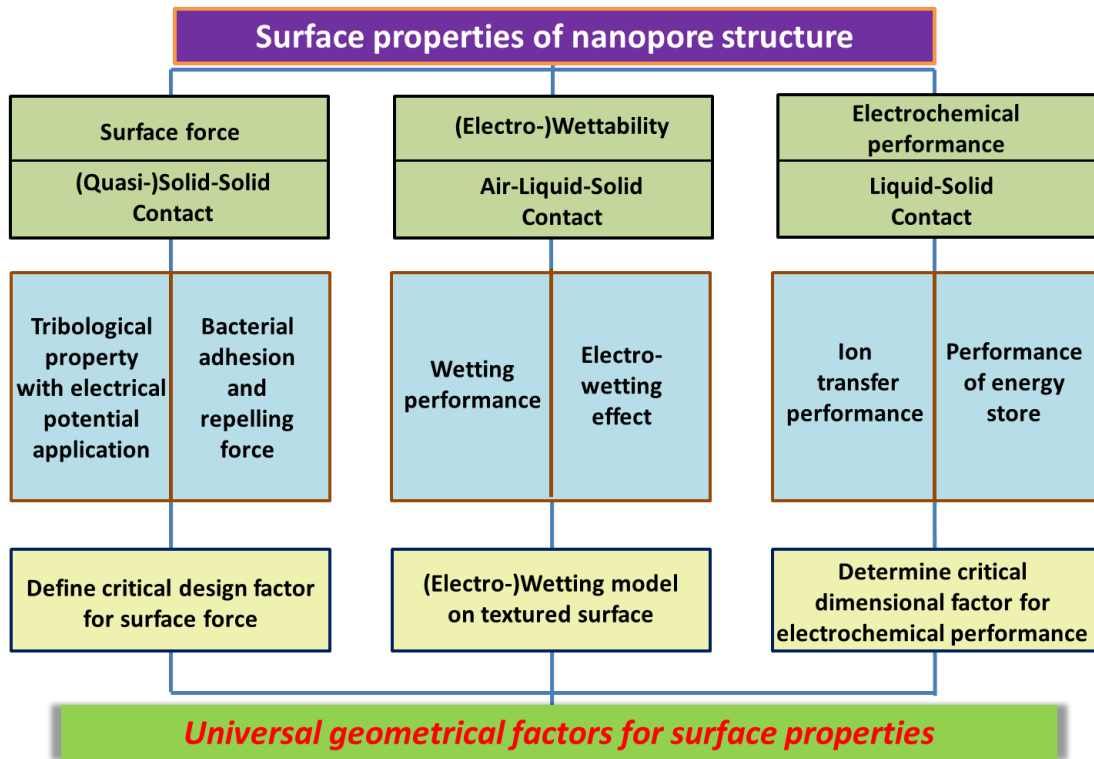


Figure 2.1. Research flow chart.

2.1. Investigation of the surface forces of ANS-based nanopore structures

Effects of an applied electrical potential on the surface structure and forces will be studied in this research. This study can determine the critical mechanism for active control of surface forces of the MNS. Surface forces such as pull-off (adhesive) force and friction force will be investigated by applying electrical potential into the MNS. With this study, the behavior of electrical potential induced surface forces will be developed.

Adhered cells introduce diseases and infections to humans, through biomaterials such as implants and surgical tools. Bacteria desorption is crucial for reducing bacterial

infections in biomaterial such as artificial joints and implants. The mechanisms of bacteria adhesive force and repelling force will be studied using ANS. The critical design factors for fabricating bacteria repelling surfaces will be studied as well.

2.2. Evaluation and understanding of electrochemical performance of nanopore structures

Improving ion transfer is one of the key factors to store energy effectively. This research will examine the feasibility using nanopore structured electrodes to enhance ion transportation. An analytical approach to design the most efficient electrode is necessary for improving electrochemical response. In order to comprehend electrochemical performance of the MNS as an electrode, the performance of ion (charge) transfer and capability of energy store of the MNS will be determined. The fundamental principles and relationship between surface structure and ion transfer will be investigated through predesigned MNS.

2.3. Determining the wetting/electrowetting mechanism of nanopore structures

Wettability is a critical factor for the design and fabrication of micro- and nanoscale structures. Manipulating surface wettability using physical methods such as electrowetting is advantageous for many engineering applications. This study will examine the intrinsic wettability and the effects of an electrical potential on the wettability of nanopore structures. In the interest of extending the scope of electrowetting applications, this work will propose further insights into how a nanopore

structure's surface wettability and structural characteristics, including various pore sizes, correlate with externally applied electrical potential.

2.4. Defining essential geometrical factors to optimize the surface properties of nanopore structures.

As a final goal, new and requisite geometrical factors of nanopore structures will be established. By understanding in effects of nanopore structures on surface properties, it will be possible to determine the critical design parameters of nanopore structures for their applications. A surface-morphology dependent design parameter will be developed by combining three major surface properties (surface force, electrochemical performance, and wettability) of ANS-based nanopore structures. Understanding effects of nanoscale contact is critical for design and development of in nanodevices. Thus, the fundamental contact phenomena on the ANS-based nanopore structures will be revealed to help the development of material's design and manufacturing for application fields in sustainable micro/nanodevices.

CHAPTER III

MATERIALS AND METHODS

This chapter addresses materials and methods which were used to perform this research. The information about the materials including fabrication process is discussed in the first part of this chapter. The characterization approach is demonstrated in the second part. Experimental details of tribological, electrochemical, and wetting/electrowetting experiment are described in the following sections.

3.1. Fabrication of materials

In the present study, two types of nanopore structures were fabricated to conduct this research. Alumina based nanopore structure (ANS) and nickel based metallic nanopore structure (MNS) were fabricated and prepared for the research. As stated in Chapter I, nanopore structures are extensively studied in various research areas due to their unique and critical properties. ANS can be used not only as a typical nanopore structure itself, but also as a template to fabricate other types of structures. Using ANS as a template, it is possible to fabricate the highly-ordered three-dimensional MNS. Fabrication details are depicted in following sections.

3.1.1. Alumina based nanopore structure (ANS)

ANSs were used to perform the bacterial adhesive and repelling force

experiment. The pore sizes of ANSs for the experiment were in the range of 30 to 80 nm. The self-assembled ANS was fabricated using a two-step aluminum anodizing method¹⁴⁰. Figure 3.1 illustrates the process steps of ANS fabrication. The pure aluminum (99.999%, thickness: 1mm) foil was used as a substrate to fabricate ANS.

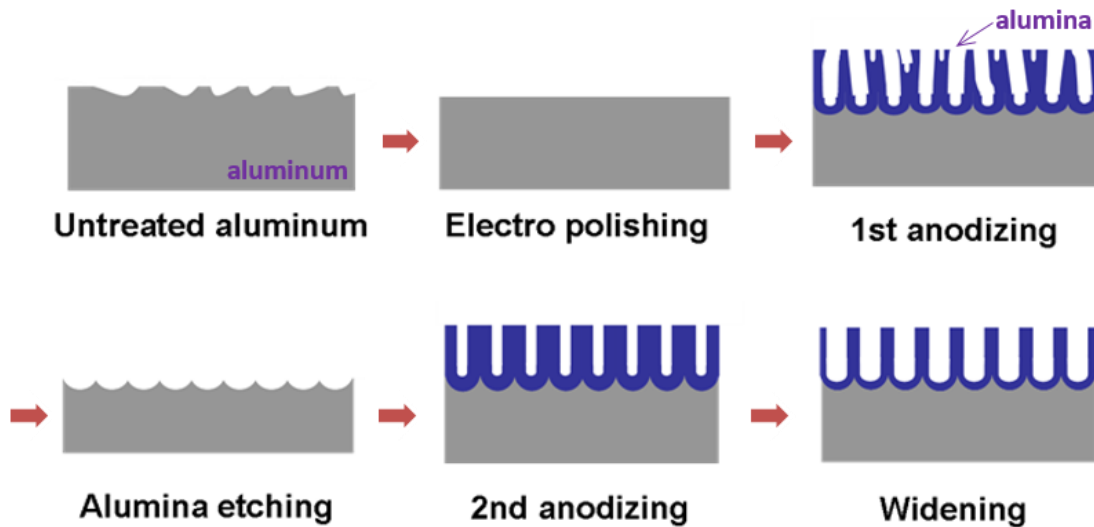


Figure 3.1. Overall process schemes for ANS fabrication.

The thickness of the aluminum foil was 1mm. Electropolishing was performed with a mixture of ethanol and perchloric acid (C₂H₅OH: HClO₄=4:1 by volumetric ratio) to eliminate the oxidation film and surface defects by applying DC type 20 V and constant 7°C temperature. As a pre-requisite process to get highly ordered nanopore structure, the electropolished aluminum substrate should be treated firstly by anodizing with applying 40 V (DC) in oxalic acid (0.3 M) at 15 °C. It was possible to get randomly formed alumina nanopore film having highly ordered nanodimple structure as a substrate after the first anodizing process. A mixture of chromic acid (1.8 wt %) and phosphoric

acid (6 wt %) applied for 6 h at 65 °C dissolved the alumina nanopore film. The highly-ordered ANS could not be obtained from the first anodizing process. The pore realms were originated at the bottom of the anodized layer, whereas the pores were created randomly at the top surface of anodized layer. Due to the volume expansion of the aluminum substrate during oxidation, the mechanical stress, which can affect repulsive force among each pore structure, is generated and this mechanical stress leads to have highly-ordered nanodimple arrays at the bottom of the layer ¹⁴¹. Using the aluminum substrate having nanodimple structures, the uniformly shaped highly ordered ANS was fabricated through the performing second aluminum anodizing process in an identical manner with first one. The initial pore diameter of ANS from the second anodizing process is about 35 nm. The pore diameter of ANS was controlled by 0.1M phosphoric acid in rate of 0.6 nm / min at 30 °C. All samples were rinsed with deionized water and ethanol.

3.1.2. Metallic nanopore structure (MNS)

Highly-ordered MNSs are fabricated through ANSs ¹⁴². The MNSs are composed of nickel including nanopored shape while the ANSs are made of alumina. By using the MNSs, electrical potential induced surface forces, electrochemical performance, and wetting/electrowetting experiments were conducted. The pore sizes of MNSs were in the range of 150 to 380 nm. Figure 3.2 shows schemetic process of MNS fabrication. ANSs were used as a template to fabricate MNSs. In order to fabricate the ANS, a pure aluminum (99.999%) foil, which thickness was about 1mm, was prepared as a base

material. To remove the oxide film and surface irregularities, electropolishing was conducted with a mixture of perchloric acid and ethanol ($\text{HClO}_4 : \text{C}_2\text{H}_5\text{OH} = 1:4$ by volumetric ratio). A DC type 20 V was applied and the temperature was maintained at 7°C during the electropolishing process. The electropolished aluminum was then rinsed using deionized water and ethanol. After rinsing, a first anodization was conducted by treating the aluminum with applying 195 V (DC) in 0.1 M phosphoric acid for 8 hours at 0°C . During this process, nanoporous were randomly formed on the top and uniform dimpled aluminum substrate formed on the bottom. To get a uniform nanodimpled aluminum substrate, the randomly formed nanoporous alumina was removed by putting it in mixed chemicals: 1.8 wt% chromic acid and 6 wt% phosphoric acid for 5 hours at 65°C . After rinsing with deionized water and ethanol, a second anodizing step was performed by applying 195 V (DC) on the substrate submerged in 0.1 M phosphoric acid for 10 minute at 0°C . After this process, the highly-ordered nanoscale porous alumina structure was fabricated. The pore-to-pore distance was about 500 nm, the initial pore size was about 100 nm, and the thickness was of about 1 μm . It is possible to widen the pore diameter through widening process with 0.1 M phosphoric acid at 30°C . The pore widening rate was about 0.6 nm / min.. In order to get the final MNE, nickel was evaporated on top of the porous alumina structure by using E-beam evaporator with 4 As^{-1} deposition rate in a vacuum of 5×10^{-6} Torr. Various pore sizes of nickel-based highly ordered MNS formed on top surface of ANSs with different pore sizes. The aluminum substrate was eliminated by saturated mercuric-chloride solution. After removing the porous alumina structure by a mixed chemical solution of 6 wt%

phosphoric acid and 1.8 wt% chromic acid at 65°C for 5 h, it is possible to get the nickel based MNS.

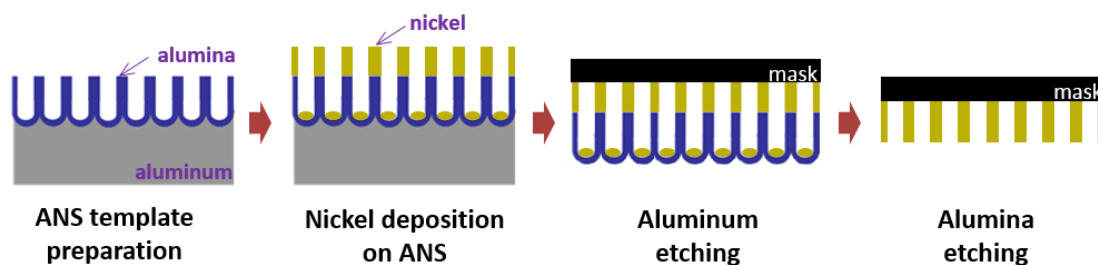


Figure 3.2. Fabrication process of a MNS by using ANS.

3.2. Characterization

The surface morphology of both ANSs and MNSs were characterized using an atomic force microscope (AFM: Nano-R, Pacific Nanotechnology, Inc.). To scan the surface of each sample, non-contact AFM mode was used with silicon nitride (Si_3N_4) based cantilever tip. The tip diameter is about 30 nm and the normal spring constant of the tip is 0.2 N/m. The top surface of each material was scanned by AFM tip. Both the height and the phase images of the materials obtained from non-contact mode of AFM.

A field emission scanning electron microscopy (FESEM: Quanta 600) was used to scan MNSs for examining pore size. The surfaces of the MNSs were coated by platinum (Pt-80%) and palladium (Pd-20%) with 5 nm thickness. The detailed of scanning conditions are: the working distance was between 9.4 μm and 10.4 μm , the accelerating voltage was 10.0 kV, and image acquisition mode was secondary electron mode.

Using a digital optical microscope (VHX-2000, Keyence), images of bacteria cells were acquired from each ANS. Software ImageJ (NIH, Bethesda, MD) was used in order

to calculate the percentage of bacteria present.

In order to check the detail shape of single pore of both ANS and MNS, a transmission electron microscopy (TEM: JEOL-1200). The TEM was operated with following detailed conditions: the accelerating voltage was 100.0 kV, image acquisition mode was transmitted image mode with CCD at -10°C, and 200 mesh-flashed copper grid was used to hold the ANS and MNS samples.

3.3. Surface force investigation

The effects of an electrical potential on the tribological properties of nickel-based MNS using an AFM. In order to study the effects of electrical potential on the tribological performance, an electrical circuit configuration was built and attached to the AFM, as illustrated in Figure 3.3. This electrical circuit configuration includes both a multimeter (Wavetek Meterman 35XP) and an ampere meter (Keithley 486 picoammeter) for checking the magnitude of the electrical potential and current signal, it also contains a DC type adjustable power source that can apply an electrical potential to the MNS during scanning. The AFM probe tips were made of silicon nitride (Si_3N_4). One AFM tip which was for contact mode tribology test has a tip diameter of 950 nm and another AFM tip which was for non-contact mode image scan has a tip diameter of 30 nm. During scanning, the electrical potential applied was from 0 mV to 800 mV. AFM test was done by repeating over 15 times. The pull-off force was measured using the AFM under an applied electrical potential. Using force-distance measurements from AFM and knowing the spring constant and deflection distance from the initial set point of the

cantilever, one can readily calculate the pull-off force at a point of contact of the AFM tip and the sample. The friction properties of the sample are measured using the lateral force microscope (LFM) mode of the AFM.

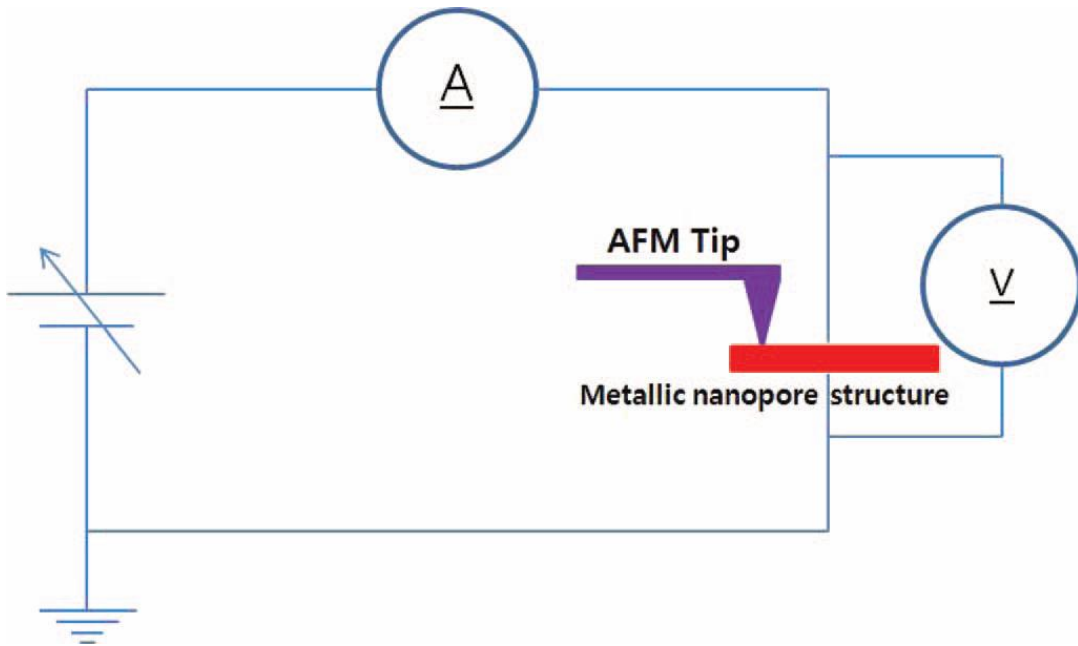


Figure 3.3. Schematic electrical circuit set-up for applying electrical potential into the metallic nanopore structure. Reproduced from ‘S. Kim, A.A. Polycarpou, and H. Liang, Active control of surface forces via nanopore structures, APL materials, Vol. 1, Issue 3, 2013’ with permission from AIP (Copyright © 2013).

Bacterial repelling experiment was conducted to understand the behavior of bacteria desorption in the room temperature with centrifugal force. The centrifugal force was applied to bacterial cells using the rotator (Model 616, EG&G PARC). The ANS with bacterial cells was attached on the Teflon plate. The rotational speed can be set by a magnetic motor. Figure 3.4 shows that schematic diagram for bacterial repelling experimental set-up. All attached ANS samples were rotated with 2000 rpm for 10

minute at room temperature. After being rotated, each of the ANS was taken off from the Teflon plate and all were rinsed with deionized water 3 times. Extra water was carefully removed by using a Kimwipe. Using a digital optical microscope (VHX-2000, Keyence), adhered bacterial cell images were acquired from each ANS.

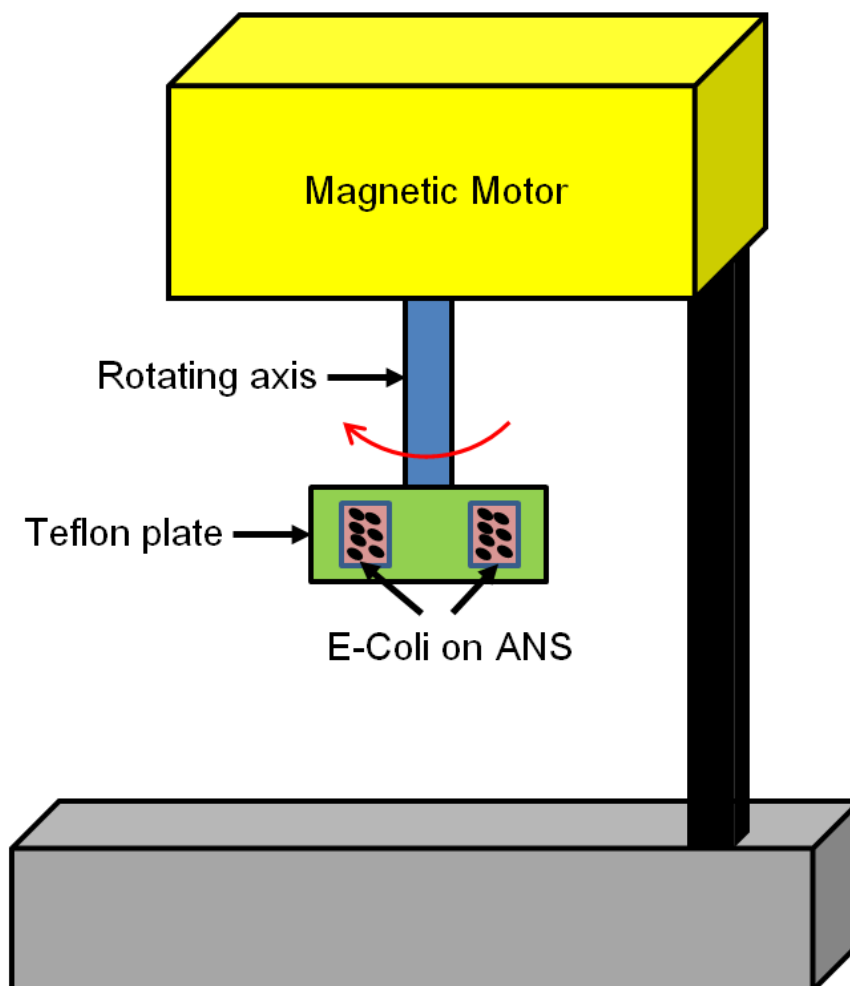


Figure 3.4. Schematic diagram of experimental set-up for bacterial repelling experiment.

3.4. Electrochemical evaluation

The electrochemical performances of the MNS were investigated by various

pore diameters in this research. Electrochemical Impedance Spectroscopy (EIS) and Cyclic Voltametry (CV) experiments were performed using an electro potential stat (Reference 600, Gamry Instruments) in 1M potassium hydroxide (KOH) as an electrolyte. These experiments were conducted using a three-electrode cell setup, Ag/AgCl as a reference electrode, Pt as a counter electrode, and MNS as the working electrode as shown in figure 3.5. For EIS experiments, AC type voltage was applied with 10 mV amplitude at the frequency ranged from 1 MHz to 100 mHz. CV experiments were conducted with the scan rate of 100 mVs^{-1} and scan range from -0.8 V to 0.8 V . The apparent area of working electrode in the cell is 0.25 cm^2 . Electrochemical experiments were conducted at the room temperature.

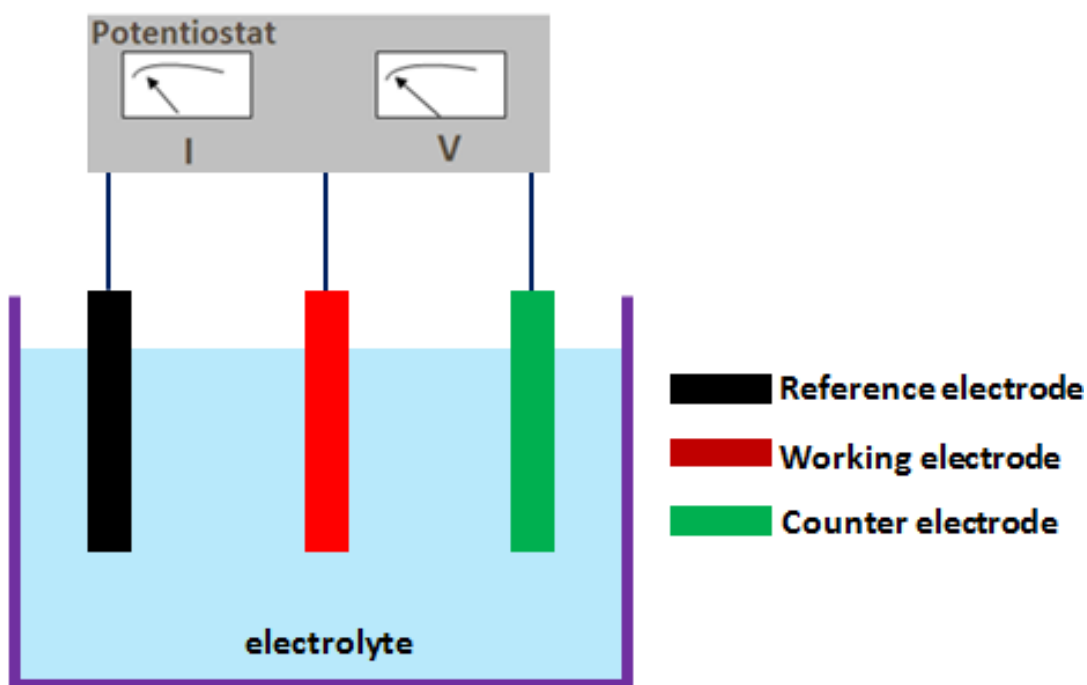


Figure 3.5. Schematic experimental setup for electrochemical evaluation of MNSs.

3.5. Wetting/electrowetting study

The wettability and electrowettability were characterized by contact angle measurement with a water droplet on the top surface of the MNS with various pore sizes. A wetting/electrowetting experimental setup is depicted in Figure 3.6. A shape of water droplet was taken by a droplet shape measurement system with a digital camera (Canon PowerShot SD750). The electrowetting experiment was performed to carry out the effect of electrical potential to the wettability of the MNS. Contact angles between water droplets and MNSs were measured from a volume of each 2 μl -deionized-water droplet. The intrinsic contact angle was measured without applying the electrical potential. In order to study the electrowetting behavior of MNS, the anode was connected with the water droplet and the cathode was connected with the aluminum substrate. Various electrical potentials were applied between the water droplet and the MNS substrate. The application range of electrical potential was from 0 V to 20 V.

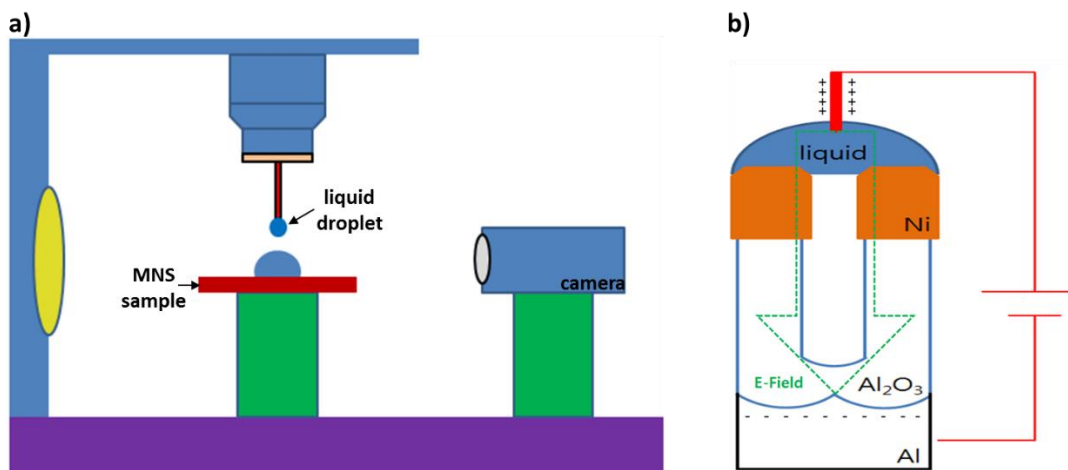


Figure 3.6. Illustration experimental setup for wetting/electrowetting on MNS: a) scheme of the liquid droplet shape measurement system, b) schematic electrowetting experiment setup by using MNS.

CHAPTER IV

SURFACE FORCES, PART I:

ELECTRICAL-POTENTIAL INDUCED TRIBOLOGICAL PERFORMANCE*

The effect of electrical potential on surface morphology and friction has been reported in various materials¹⁴³⁻¹⁴⁶. To date, however, the tribological performance of nanodevices under the influence of an applied electrical potential has not been well-studied. An understanding of the effects of electrical potential on the tribological performance at the nanoscale is important for the design and reliability of nanoelectromechanical systems (NEMS). The effect of electrical potential on surface morphology and on tribological performance of MNS will be discussed in this chapter.

4.1. Effect of electrical potential on surface morphology

MNSs were prepared by evaporating nickel as a metal source on ANSs as described in Chapter III. The MNS pore diameter is controlled by changing the pore diameter of ANS, which in this work varied from 150 nm to 350 nm (zero nm pore implies dense surface with no pores). By using AFM, the surface morphology of MNS were scanned with applying electrical potential.

Figure 4.1 depicts AFM height images of the MNS under various applied electrical potentials from 0 to 800 mV. As shown in the figure, the higher regions (peaks) become

* Part of this chapter reprinted with permission from “Active control of surface forces via nanopore structures” by Sunghan Kim, et al., APL materials, Vol. 1, Issue 3, 2013 (Copyright © 2013, AIP Publishing LLC)

larger as the applied electrical potential increases. The lower regions (valleys), on the other hand, become deeper with increased electrical potential. The circle in the figure represents a unit wall of the MNS. It is seen to expand with increasing electrical

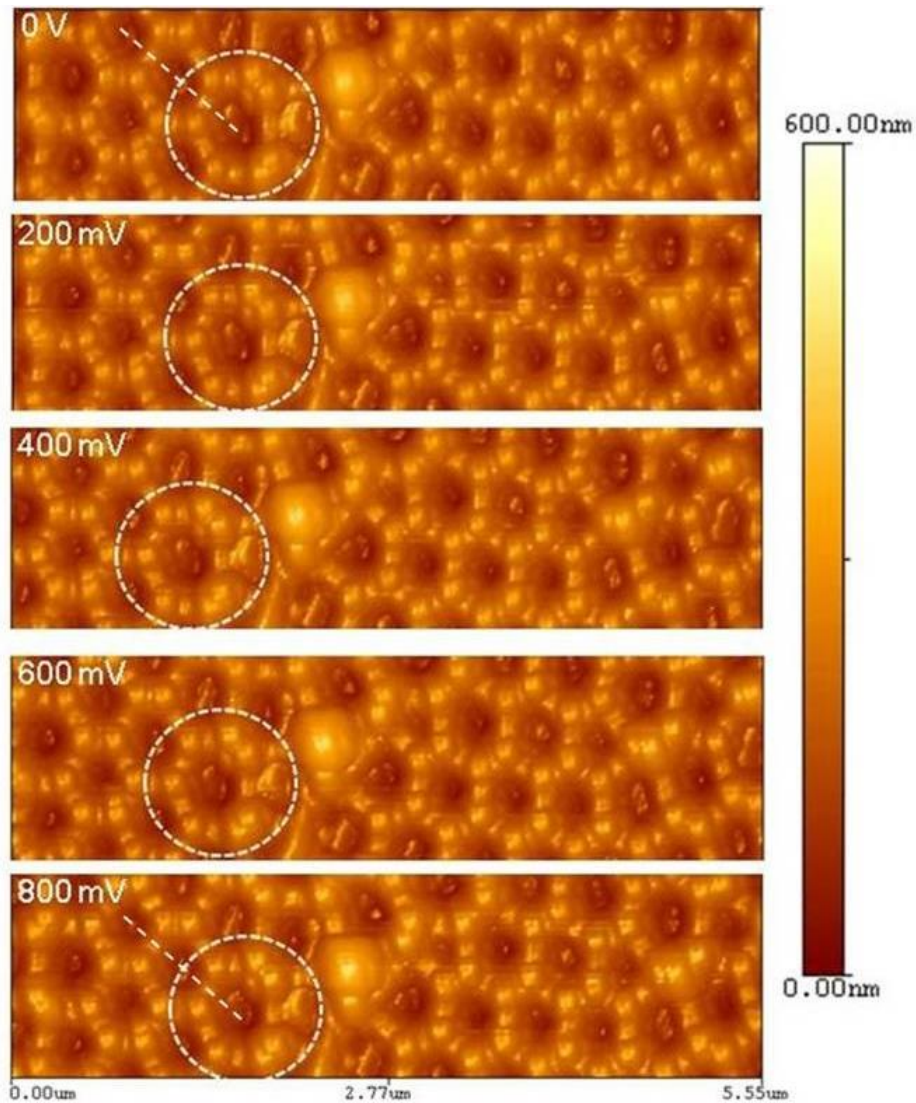


Figure 4.1. AFM height images about MNS with various electric potential energy from 0 to 800 mV.

White circles highlight the same area in various electric potential conditions and white lines are for profile checking regions. Horizontal scanning distance is 5.55 μm . The scale bar represents height level of MNS from 0 to 600 nm.

potential. Figure 4.2 shows profiles of MNS (corresponding to white lines in Figure 4.1) are changed with the electrical potential applied in comparison 0 mV electrical potential with 800 mV applied condition. As a result, the morphology of the MNS was expanded with the increase in electrical potential. To analyze the AFM height image change, alteration of over 350 nm height regions were examined with applying electrical potential. Figure 4.3 shows a percentage change of over 350 nm regions

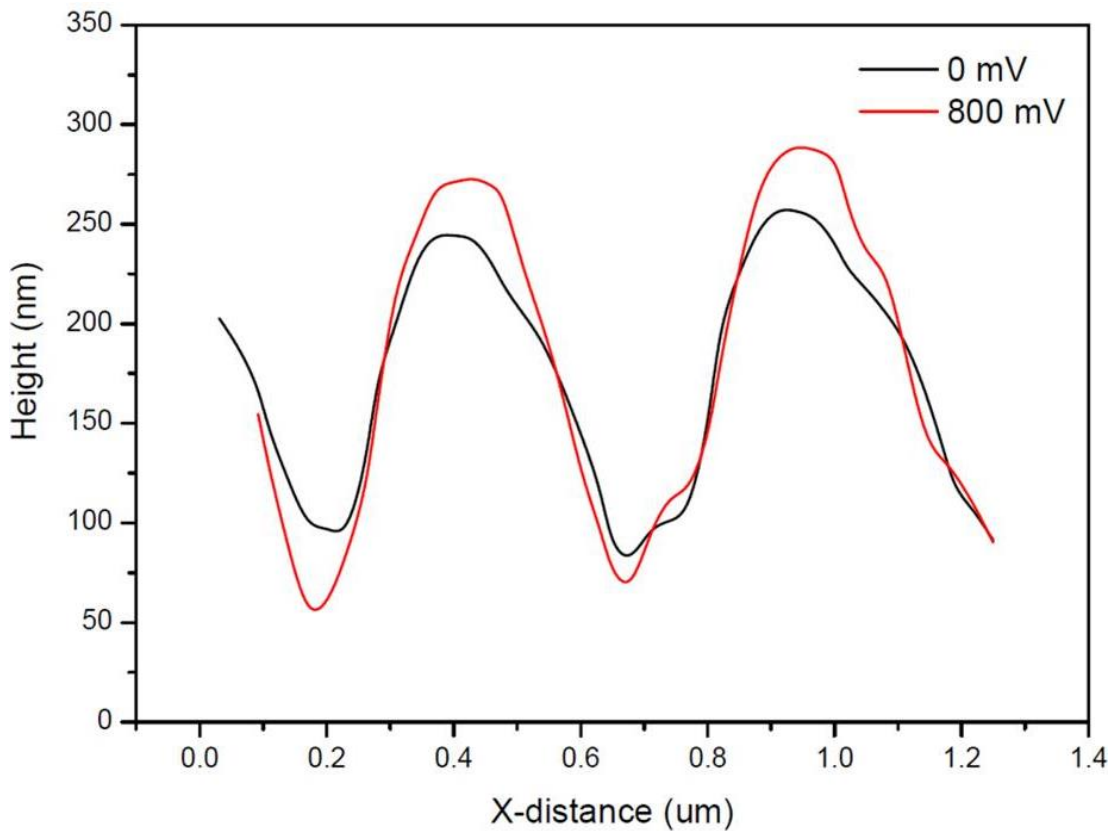


Figure 4.2. MNS profiles which are represented by white lines in Figure 2 with 0 mV and 800 mV applied electrical potential conditions.

in certain areas of MNS height image when the electrical potential increases. The percentage of over 350 nm height region was increased by increasing electrical potential.

This result indicates that the surface morphology of MNS is influenced by the electrical potential. In one of our previous studies, we have reported expansion of a piezoelectric polymer under an applied voltage ¹⁴⁷. It is interesting that the current letter showed similar effects on Ni-containing MNS. Figure 4.4 shows the corresponding AFM phase images of the MNS.

On the same scale bar, the contrast of MNS phase images change with electrical potential that was varied from 0 to 800 mV. The brighter region (phase-shift signal: over

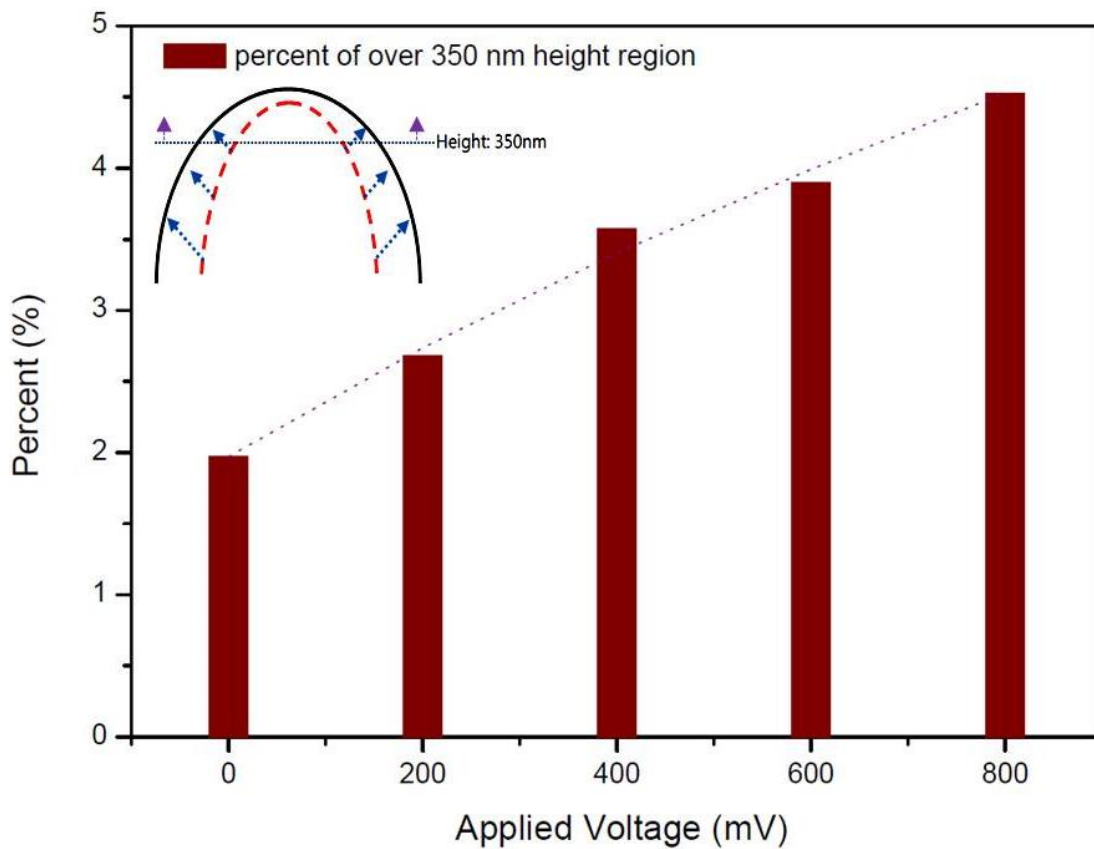


Figure 4.3. Percent of over 350 nm height region with electrical potential applying from AFM height image.

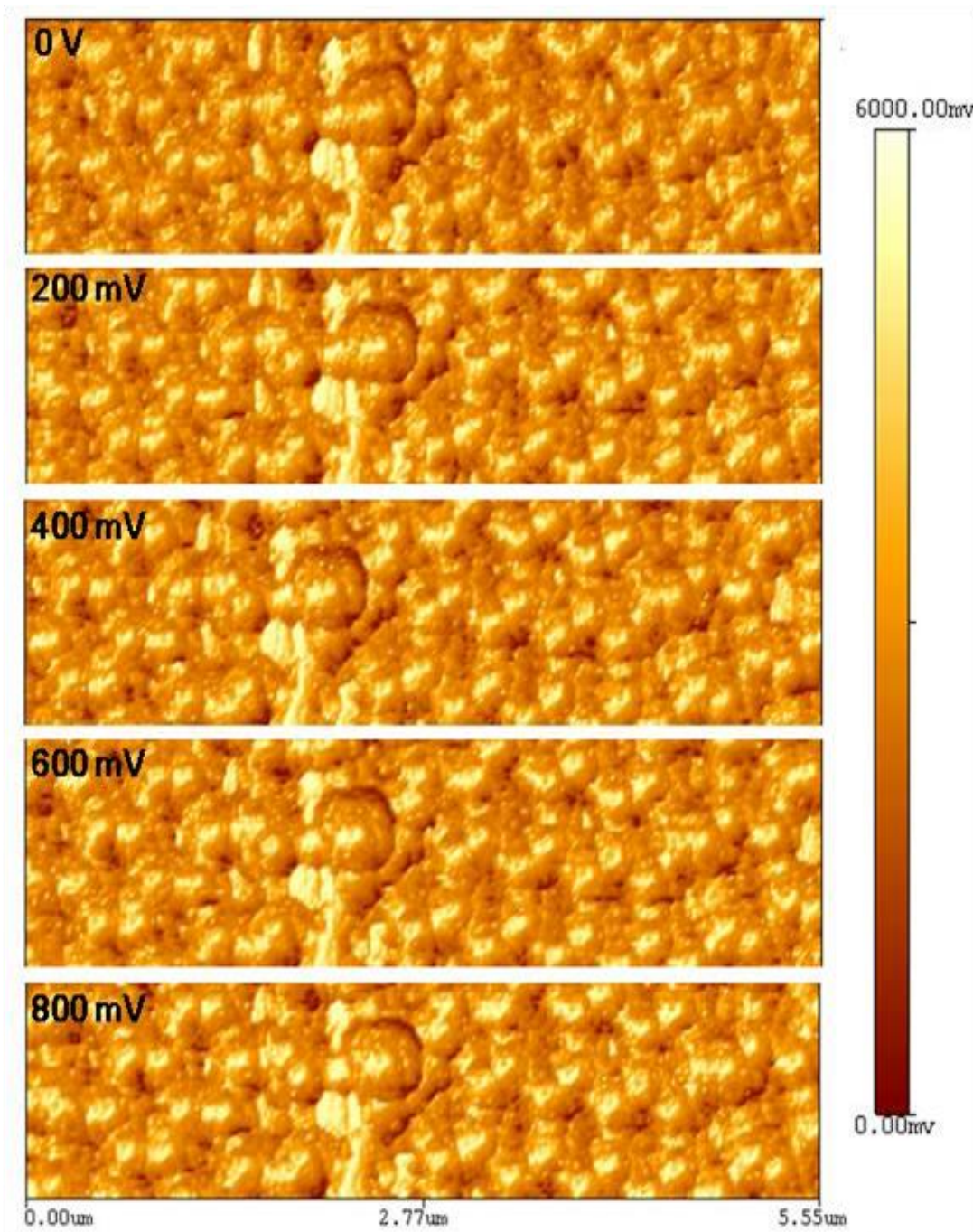


Figure 4.4. AFM phase images about MNS with various electric potential energy from 0 to 800mV. Horizontal scanning distance is 5.55 μm . The scale bar represents phase-shift signal of MNS from 0 to 6000 mV.

4000 mV) becomes larger with the increase in potential. The AFM phase images clearly show that surface property of MNS is affected by applied electrical potential and it can be related to tribological behavior of MNS. These height and phase image alterations indicate the change of contact area that is related to friction and adhesion. This will be discussed next part.

4.2. Effect of electrical potential on tribological performance

Using the force-distance AFM mode, we conducted MNS pull-off force which is represented as a characteristic parameter of the adhesion and friction experiments, and the results are shown in Figure 4.5. It is possible to identify that the pull-off force was reduced due to the existence of the pores. The white bar is that of the “flat” (no pores) surface that exhibits the highest pull-off force values. The lowest values of pull-off force are obtained from the sample with the largest pores of 350 nm, showing an 88.32% reduction in pull-off force, in comparison with the flat surface without the applied electrical potential. It is known that the pull-off force is affected

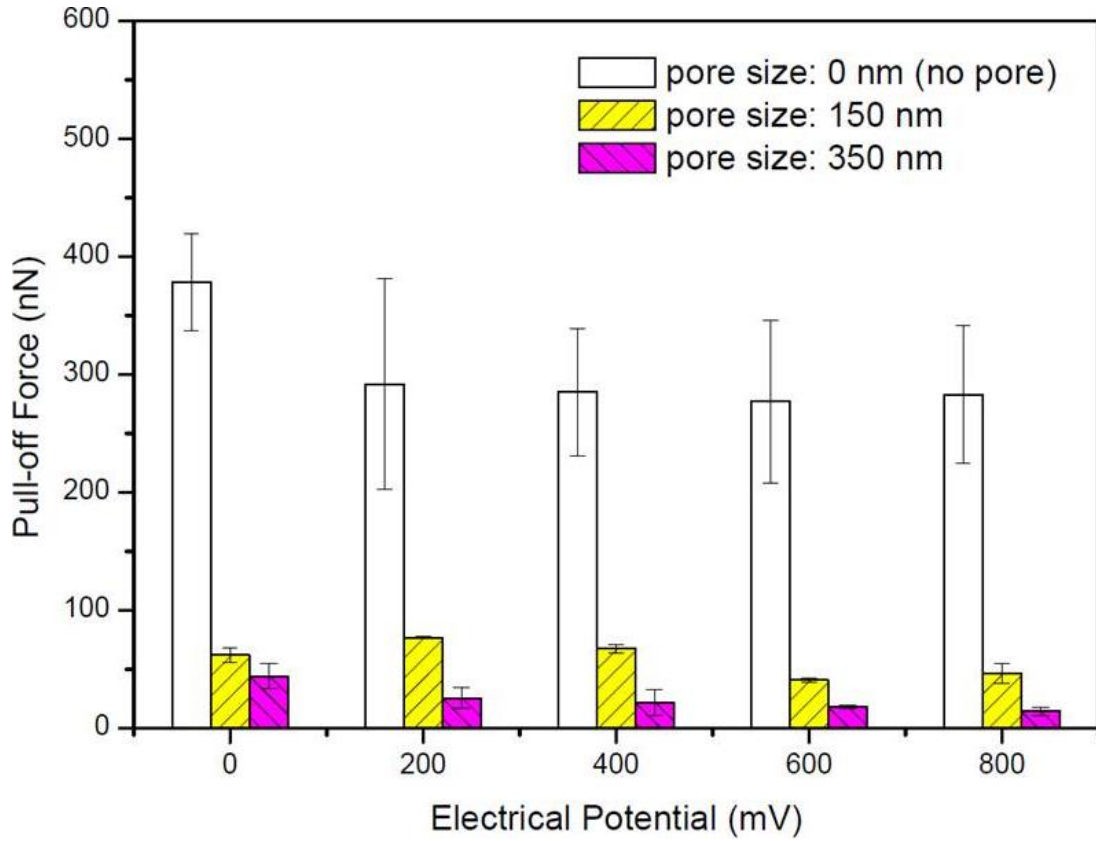


Figure 4.5. Electrical potential activated pull-off force with various MNS samples. Each bar represents average value of pull-off force and error bars show standard deviation with one sigma.

by the real contact area. A contact radius c , which is based on the Hertz contact theory¹⁴⁸, between the AFM tip and the flat (no pores) nickel surface is represented by the following equation:

$$c^3 = \frac{3PR}{4K} \quad (4-1)$$

where P is the applied load, R is the radius of tip, and K is the indentation modulus expressed by:

$$\frac{1}{K} = \frac{1-\nu_1^2}{E_1} + \frac{1-\nu_2^2}{E_2} \quad (4-2)$$

where both E_1 and E_2 are moduli of elastic, and ν_1 and ν_2 are Poisson's ratios. Those parameters (1 and 2) represent tip and surface. The Hertzian contact area A is assuming infinitely smooth surfaces.

$$A = \pi \cdot c^2 \quad (4-3)$$

When the AFM tip comes in touch with the MNS, the Hertzian contact area is set by the surface porosity of MNS ¹⁴⁹. Basically, the contact area is decreased with the increase in surface porosity based on the Hertzian contact. The inter-pore distance of MNS is about 500nm, the surface porosity for flat surface (no pore) is 0, for 150 nm pore is 8.16%, for 350 nm pores is 44.43 %. An equivalent contact area A_{eq} is represented by:

$$A_{eq} = A \cdot (1 - P.O.) \quad (4-4)$$

$$P.O. = \frac{-3\pi\left(\frac{d}{2}\right)^2}{\frac{3\sqrt{3}}{2}a^2} \quad (4-5)$$

where P.O. is surface porosity, d is the pore diameter, and a is the inter-pore distance.

The equivalent contact area is reduced by pore size enlarging which means that the surface porosity increasing without electrical potential applied (0mV). When an electrical potential is applied, the magnitude of pull-off force of MNS is gradually decreased, in Figure 4.5. According to the equation (4-1), the contact area is decreasing with increasing indentation modulus. From AFM phase image results, the brighter region which represents even higher stiffness or elastic modulus ¹⁵⁰⁻¹⁵² of MNS gradually

increased with increasing electrical potential. This means indentation modulus between the MNS and AFM tip is increasing. The contact area between AFM tip and MNS decreases with increasing electrical potential due to the stiffness of the MNS increasing. On the other hand, the equivalent contact area increases with decreasing pore size due to the porosity decreased, according to Eq. (4-4). Figure 4.1 shows that the pore size is decreased by applying electrical potential due to the unit wall expanded.

For the discussion of MNS' contact area, the increasing stiffness conflicts with the porosity decreasing under same electrical potential increased condition. Porosity-decreased works to increase the contact area, however, stiffness-increased works to decrease contact area. Overall, pull-off force decreases with increasing electrical potential. This means that stiffness factor more intensively affects to change the equivalent contact area of MNS than porosity factor. This result proves that the pull-off force could be changed by applying electrical potential into the MNS. According to Figure 4.5, the flat sample has the highest pull-off force. This indicates the more active interactions between AFM tip and the surface itself. Without any porous, the contact between the AFM tip and the surface is expected to be larger hence the high force.

Friction experiments were conducted using the AFM with LFM mode and results are shown in Figure 4.6. The flat surface (no pore) with much smoother surface profile shows lower electrical volt, i.e., friction volt than MNSs. The friction volt, overall, is decreased with the increase in electrical potential. The frictional performance which is determined by LFM mode depends on the degree of the lateral twist of an AFM tip. Surface morphology and contact area of MNS are critical parameters to determine

the friction performance of MNS with AFM. According to results of height images, the edge of the surface became much blunter rather than sharp with applying electrical potential due to the swelling of surface (inset image of figure 4.3). In this case, AFM

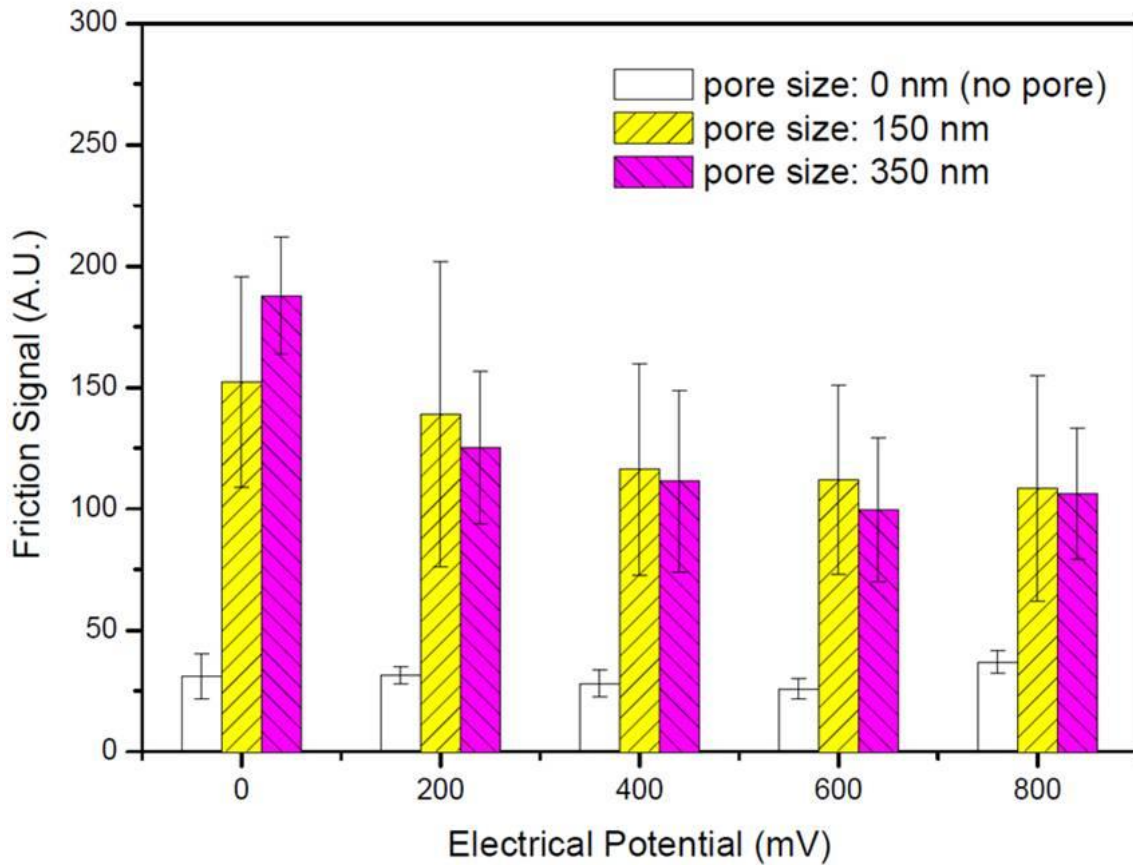


Figure 4.6. Electrical potential activated friction signal with various MNS samples. Each bar represents average value of friction signal and error bars show standard deviation with one sigma.

tip can be less twisted than before applied electrical potential into the MNS. Moreover, contact area decreasing at interface between AFM tip and MNS with increasing electrical potential could contribute to the decrease in friction. The big error bar of each data point is due to the relative size comparison between the AFM tip and sample

surface. The variation of the surface with pores will cause the high variation of the tip-surface interactions. This is correlated to our analysis in contact area.

On average, the pull-off force was non-linearly decreasing with increasing electrical potential. This is because the pore size of MNS is not the same in the scanning area. Basically, the pull-off force experiments were performed by single point of contact of the tip and target. The result of pull-off force which depends on localized pore size could show non-linear behavior with applying electrical potential due to the lack of uniformity about pore size in MNS. In comparison, friction test is relatively insensitive to localized pore size, because the friction result stems from scanning large area of surface. The conflict interaction by electrical potential increasing between porosity and stiffness is also caused that tribological behavior of the MNS decreased, non-linearly. It is possible to indicate how many percent of tribological property such as pull-off force and friction signal changed in case of the MNS which pore size is 150 nm and 350 nm. Based on 0mV applied condition, the pull-off force decreased at 800mV applied condition. In case of 150 nm pore size sample, the friction signal and pull-off force were decreased by 28.82% and 24.71%, respectively. About 350 nm pore size sample, the friction signal and pull-off force were decreased by 43.41% and 67.70%, respectively. Reduction gap appears even larger in 350 nm pore size than 150 nm pore size. This result can reveal that degree of contact area alteration depends on the pore size of MNS.

The results of pull-off force and friction performance in MNS clearly indicate that applying electrical potential into the MNS can change the surface shape, surface morphology, and material property such as stiffness which are important parameter to

determine tribological performance of MNS. We can identify that the reason of tribological behavior changing about MNS is attributed the surface condition alteration by applying electrical potential.

4.3. Effects of electrical potential on indentation modulus

To study effects of an electrical potential, nanoindentation under an applied potential was performed using the TS 75 TriboScope nanoindentation device (Hysitron, Inc.). A conical indenter tip made of diamond with a radius of about 1 μm was used. Figure 4.7 shows a SEM image of the conical indenter tip. To apply electrical potential to each metallic nanopore structure (MNS), an electrical circuit was set with the TriboScope as described in Chapter III. Current and voltage signals can also be checked by using an ampere-meter and voltage-meter with this electrical circuit. A tunable DC-mode power source was also used to apply an electrical potential into the MNSs. Using the applied load and indentation distance curve measurement function of the TriboScope, the indentation moduli of the MNSs were measured when accompanied by applied electrical potential.

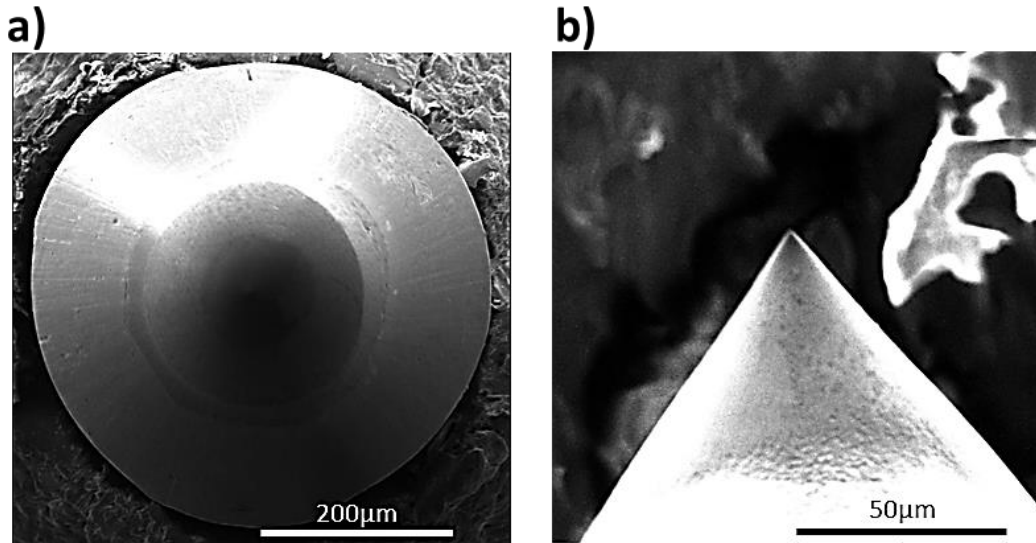


Figure 4.7. SEM images of the conical indenter tip: a) top view of the conical tip, b) side view of the conical tip.

Figure 4.8 shows the applied loads and resulting indentation depth curves of MNSs with various pore sizes. In each case, the indentation modulus was able to be measured by the slope of the unloading curve. Greater stiffness of the curve represents a greater indentation modulus. As the figure indicates, the slope of the unloading curve decreased as the pore size of the MNS increased. Moreover, the corresponding indentation depth increased with pore size increase. Increased pore size naturally leads to increased porosity of the MNS. When porosity increases, there is a corresponding decrease in the mechanical properties of materials, such as indentation modulus¹⁵³. The results of this experiment demonstrate that the indentation modulus decreased as the pore size of the MNS increased.

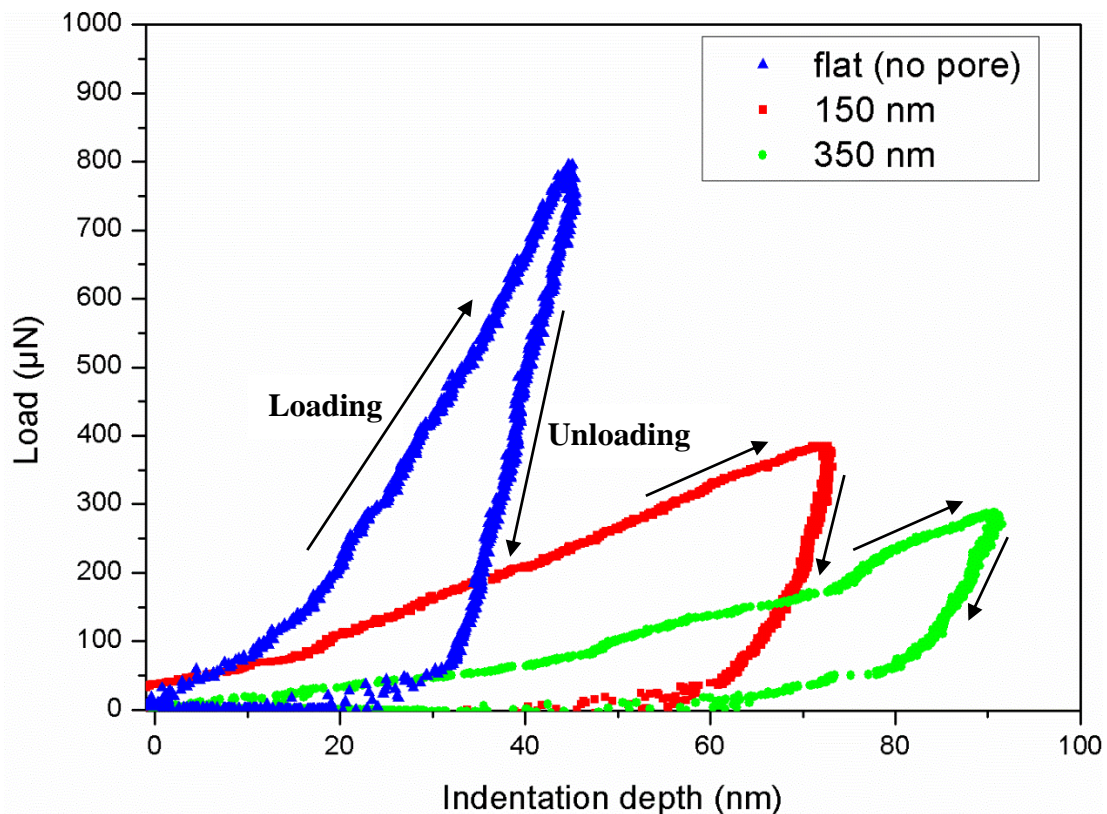


Figure 4.8. Load and indentation depth curves for MNSs with various pore sizes.

The effect of electrical potential on the indentation modulus occurred when electrical potential was applied into the MNSs during indentation experiments. Figure 4.9 shows the indentation modulus of MNSs with various pore sizes according to the applied electrical potential. As the figure shows, the indentation modulus observed without applying electrical potential (0 mV) decreased as the pore size of MNS increased. These results correlate with the load and indentation depth curve results. Moreover, the indentation modulus showed an overall trend of decreasing as the application of electrical potential increased. Results indicate that the electrical potential affects the electronic and atomic structures of surfaces in accordance with the observed

indentation modulus behavior.

As stated above, the indentation modulus is a critical factor in defining the contact area, with contact area decreasing as the indentation modulus increases. Previously, AFM phase images have been used for qualitative analysis of the effect of electrical potential application on the stiffness of MNS. As the indentation experiment indicates, the indentation modulus, which can represent the stiffness of the MNS, increased with increased application of electrical potential. This feature demonstrates that, in terms of quantitative analysis, the contact area between the tip and the MNS decreased with an increased applied electrical potential.

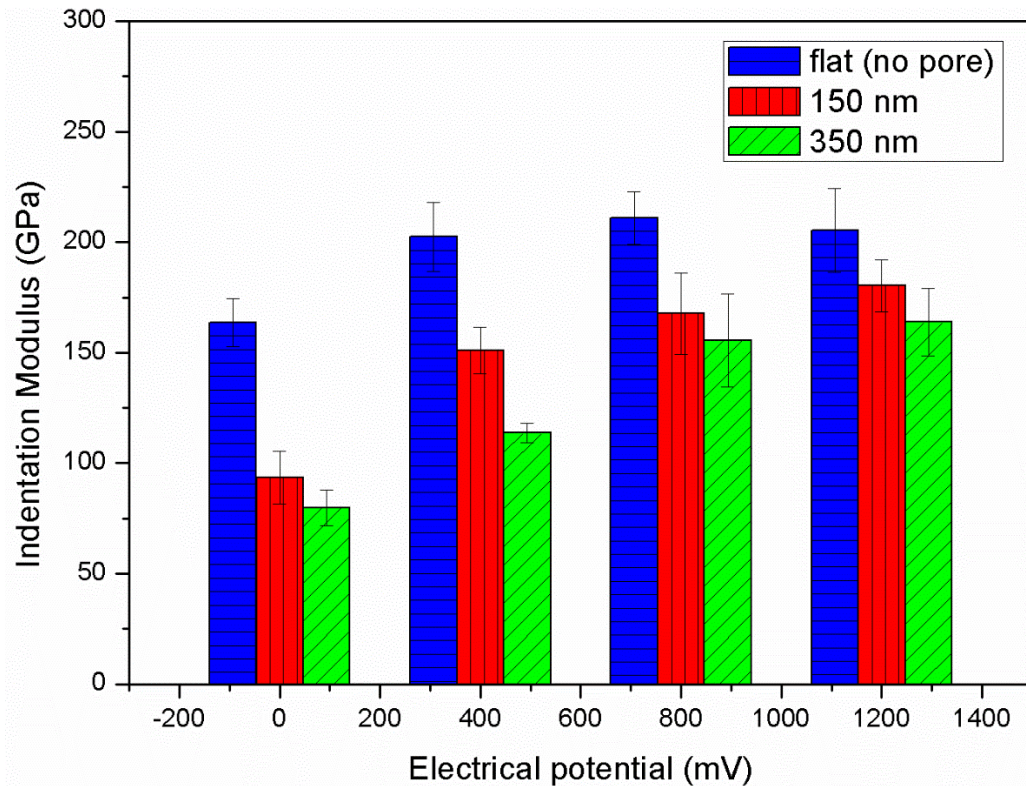


Figure 4.9. Indentation modulus against application of electrical potential in MNSs with various pore sizes.

4.4. Summary

Effects of an applied electrical potential on the surface structure and forces were studied in this chapter. Nickel-based MNS were fabricated and characterized with AFM and Triboscope. Surface morphology, tribological performance, phase distribution, and indentation modulus were evaluated. Results showed that the MNS was expanded and stiffened with the increase in electrical potential. The friction and pull-off force obtained using the AFM were found to decrease with the increase in electrical potential. The indentation modulus was dependent not only on pore size but also the amount of electrical potential applied. The contact area was altered by porosity and indentation modulus. The nickel based MNS enables the control of friction and pull-off force. This characteristic can be used to optimize pore size and amount of electrical potential applied for enhanced performance of MNS-based devices, in terms of durability and design for enhanced reliability.

CHAPTER V
SURFACE FORCE PART II:
INFLUNCE OF NANOPORES ON BACTERIA

Bacteria introduce diseases and infections to humans, by their adherence to biomaterials such as implants and surgical tools. Cell desorption is an effective step to reduce such damage. This chapter studies the effects of nanopored surface on the bacteria adhesion and repelling performance. In terms of contact area a cell on alumina nanopore structure (ANS), the bacteria accessibility on ANS can be manipulated by altering the pore size of ANS. Both the surface morphology of ANS and the shape of bacteria cell will be evaluated to determine contact area. The number of bacteria cell on the ANS will be examined before and after rotating experiment. The correlation between pore size and bacterial adhesion and repelling performance on the ANS will be determined.

5.1. Morphological characteristics

ANS were fabricated by following the described fabrication method in Chapter III. Surface images of ANS were taken using an AFM with non-contact mode. Figure 5.1 shows the AFM height images of the controlled ANS sizes: 35 nm, 55 nm, 70 nm, and 80 nm in terms of average pore diameter. For all samples, the distance from pore to pore is about 100 nm. The images show that the ANS is hexagonally highly-ordered nanopore

structure. Understanding the contact condition between bacterial cells and ANSs is important to study for bacterial adhesion. The bacterial cells were cultured on ANS with various pore sizes. The examined bacterial cells are *E. coli* strain DH5 α . *E. coli* is widely studied and one of the most understood cell systems¹⁵⁴⁻¹⁵⁸. Previous understanding is the basis of the current work. The cells of *E. coli* were extracted from -80°C storage and streaked on a Luria-Bertani (LB)

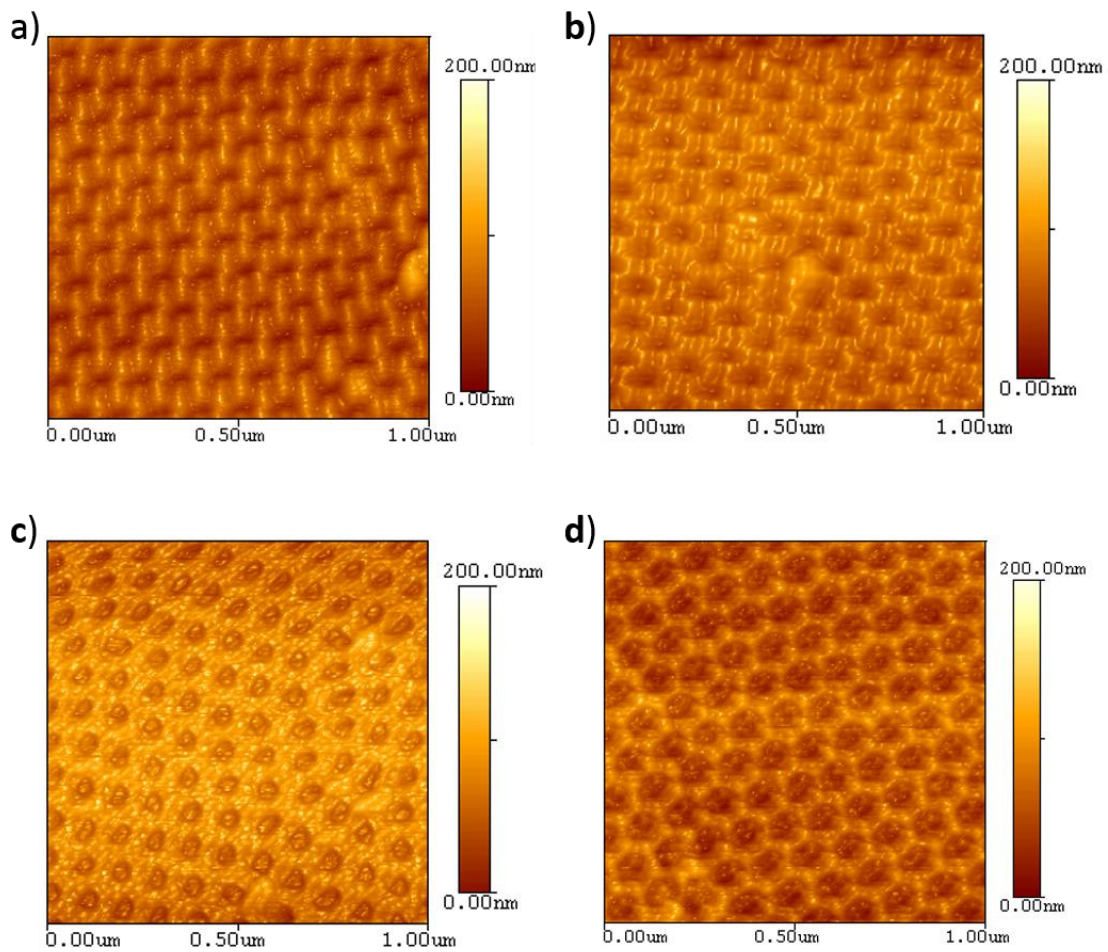


Figure 5.1. Atomic force microscope (AFM) images of alumina nanopore structure (ANS) with various pore diameters: The pore diameters are about: (a) 35 nm, (b) 55nm, (c) 70 nm, and (d) 80 nm.

based agar plate. The culture medium, liquid LB, was inoculated with individual colonies that were collected from the agar plate. The bacterial cell culturing is inoculated with optical density at 600 nm (OD_{600}) of 0.3. Cell culturing was continued with constant stirring for 24 h at 37.5 °C. For cell culturing on ANS, 40ml of the LB media were poured into Petri dishes having different pore size ANSs with 1% bacterial cells addition from the inoculum. All ANS samples were rinsed using deionized water and ethanol and then put into the Petri dish with the nanopore surface facing up. Cultured *E. coli* were kept in an incubator for 18 h at 37.5 °C. After incubating, all ANS samples were taken out from the Petri dish and rinsed using deionized water 5 times. The bottom of each ANS was cleaned using ethanol. Remaining water was absorbed by carefully touching a Kimwipe on the side of ANS.

Figure 5.2 shows the AFM images of bacteria on ANS. The image was taken using the non-contact AFM mode. Before imaging, the sample was rinsed using deionized water and then air dried. As the figure shows, the bacterial cells are on the top surface of the ANS. From the AFM height image (figure 5.2.a), the parallel cross section shape with ANS surface of single bacterial cell looks like ellipse. A white circle highlighted a single bacterial cell was zoomed in at figure 5.2.b. The bacterial cells are covering several nanopore of the ANS. The phase image of AFM (figure 5.2.c and 5.2.d) clearly indicates that the elliptical shaped objects are bacterial cells due to them having a darker region which represents even lower stiffness. The surface of ANS which is made by ceramic (alumina) generally has a greater stiffness than bacterial cells. These AFM images show that a bacterial cell, which has elliptical shape, is attached on the ANS.

According to the AFM images, it is possible to simplify the contact model between bacterial cell and ANS.

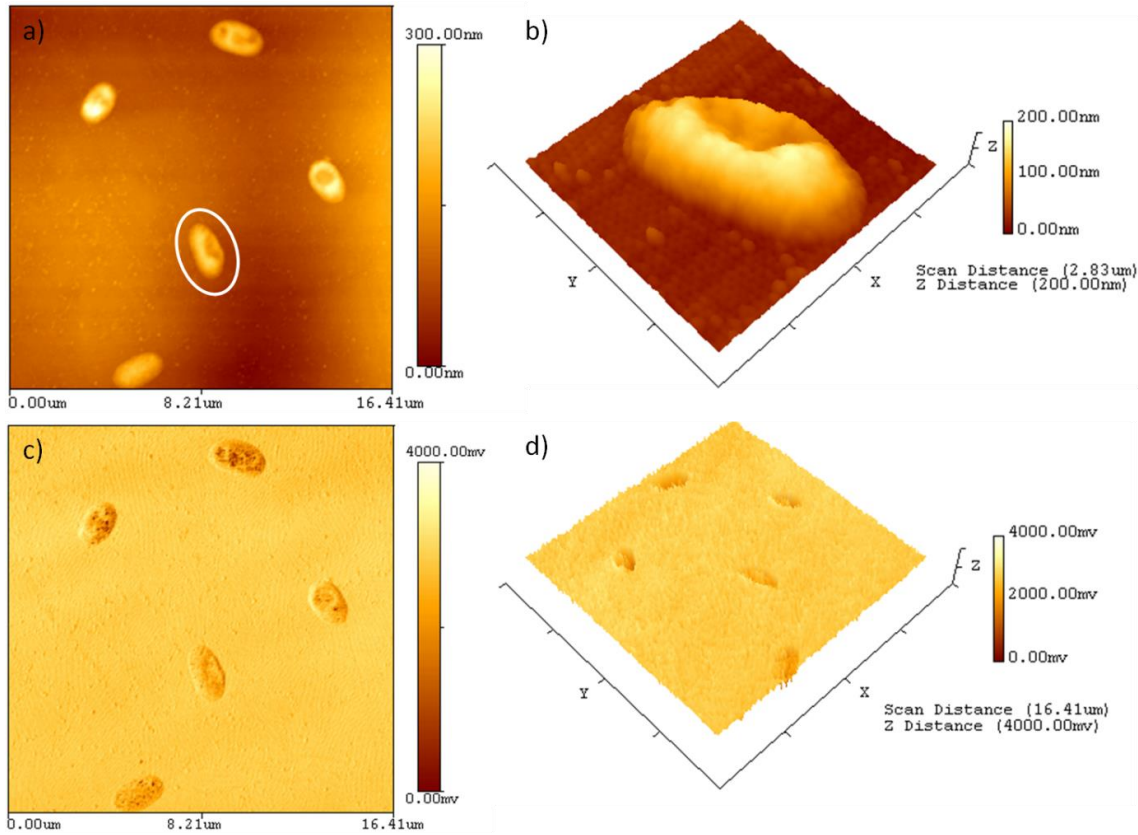


Figure 5.2. Atomic force microscope (AFM) images of bacterial cells on alumina nanopore structure (ANS, pore diameter: 55 nm) (a) 2-dimensional height mode AFM image of bacterial cells on the ANS, (b) zoomed in 3-dimensional height mode AFM image of single bacterial cell on the ANS, (c) 2-dimensional phase mode AFM image of bacterial cells on the ANS, and (d) 3-dimensional phase mode AFM image of bacterial cells on the ANS.

5.2. Contact area calculation between bacteria and ANS

Based on the AFM images, a contact area between a bacterial cell and ANS can

be calculated. A relative contact model ¹⁴⁹, which is about between AFM tip and ANS, was used to calculate the contact area. In order to calculate the contact area, the porosity of ANS should be considered. As illustrated in figure 5.3, the contact area could be defined by hexagonal shape unit area which is extracted from the AFM height image with connection six center of pore in ANS. The contact area is determined by the following equations:

$$f(r) = 1 - \frac{3\pi r^2}{\left(6 \times \frac{\sqrt{3}}{4} l^2\right)} \quad (@ l = 100 \text{ nm}) = 1 - \frac{\pi r^2}{8660.25} \quad (5-1)$$

$$F(r) = S \times f(r) \quad (5-2)$$

where $f(r)$ is a ratio of unit area, l is the pore to pore (interpore) distance, r is the radius of a pore, S is bottom area of bacteria, and $F(r)$ is the contact area. The interpore distance ' l ' is fixed with 100 nm among all ANS samples. The contact area is simply determined by multiplying ' $f(r)$ ' and ' S '. Based on the bacteria images taken on the ANS, the bottom area of bacterial cell ' S ' can be expressed by:

$$S = \pi ab \quad (5-3)$$

a measurement of semi-minor axis of bacteria cell is expressed by ' a ' and a measurement of semi-major axis of bacteria cell is expressed by ' b '. The average value of ' a ' and ' b ' are 0.25 μm and 1 μm , respectively. The bottom area of single bacterial cell is about 0.79 μm^2 . The contact condition between a bacterial cell and the ANS is

identified by AFM images and contact area calculations.

As shown in Table 5.1, the contact area between bacterial cell and the ANS decreased with the increasing pore size. This result clearly indicates that ANS having larger pore size is rarely in contact with bacterial cells.

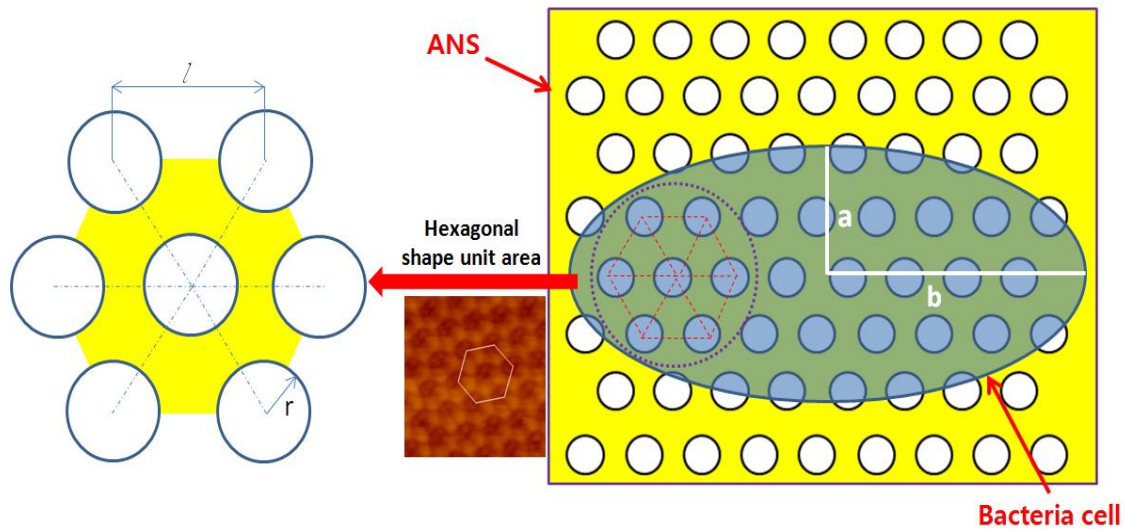


Figure 5.3. Schematic diagram to define the contact area between a bacterial cell and alumina nanopore structure (ANS). The extracted atomic force microscope (AFM) image of ANS (pore diameter: 80 nm) shows the hexagonal shape unit area.

Table 5.1. Average (Avg) pore diameter of alumina nanopore structure (ANS) and the corresponding Contact area with unit area ratio.

Avg. Pore Diameter (nm)	Avg. Pore Diameter (stdv)	Unit area ratio	Contact area (μm^2)
0 (no pore)	0	1.00	0.79
35	2.877	0.89	0.7
55	2.747	0.73	0.57
70	2.76	0.56	0.44
80	2.714	0.42	0.33

5.3. Number of bacterial cells on ANS

Figure 5.4 shows the represented optical microscope images (color converted: black and white) of bacterial cells on ANS. The black color represents adhered bacterial cells on ANS. The top images are taken before conducting repelling experiment with various ANS's pore size and the bottom images are taken after performed repelling experiment.

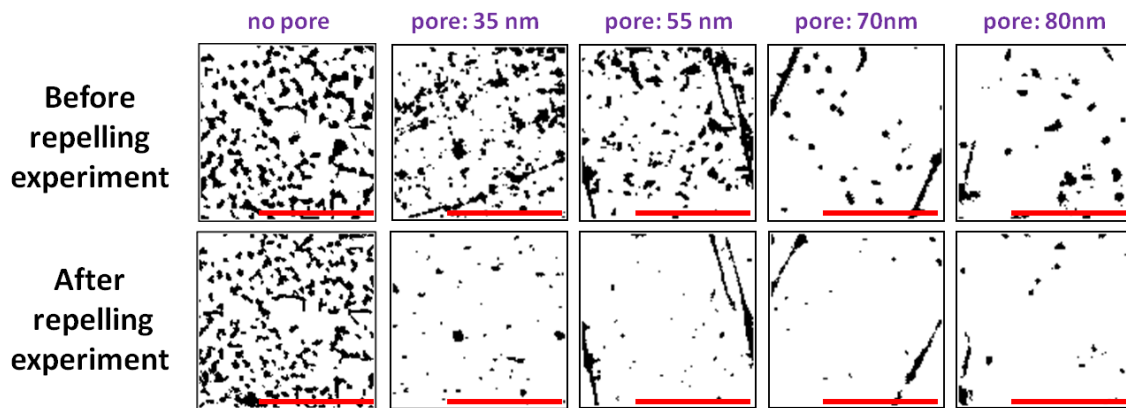


Figure 5.4. Optical microscope images of bacterial cells on the alumina nanopore structure (ANS) with various pore diameters. Black color represents bacterial cells. Top images stem from before repelling experiment and bottom images stem from after repelling experiment. The scale bar in each image represents 100 μm .

As shown in this figure, the adhered bacterial cells are decreased with the increasing the pore size in case of 'before repelling'. The other interesting result is that the adhered bacterial cells are mostly removed by the repelling experiment from all ANS samples, but there is slightly reduced number of bacterial cells after the repelling experiment on the samples without pores. In order to understand the adhesion

mechanism of bacterial cells on the ANS both in case of ‘before repelling’ and ‘after repelling’, the contact condition between bacterial cells and ANS needs to be considered.

5.4. Analysis of bacterial adhesion and repelling force

As shown in figure 5.4, the number of adhered bacterial cells decreased with increasing pore size in the first case ‘before repelling’. The numbers of adhered bacterial cells are fewer in number when the contact area of the bacterial cell decreases. In order to study the adhesion of bacterial cells to the ANS with various contact area, the percentage of adhered bacterial cells on the ANS was measured by optical microscope with the ‘ImageJ’ software. To calculate the percentage of bacterial cells, the total area covered by bacterial cells were divided by the sampling area of the ANS: the size of the unit area is 150 μm x 150 μm . As stated above, the bacterial cells were represented as a black color while the ANS surface were typified by white color in figure 5.4. The total area of bacterial cells were figured out by summing all black color area (bacterial cells). On the cultured sample surface, 6 regions were chosen and evaluated for number of adhered cells. Table 5.2 shows the statistical data result of the adhered bacterial cells on the ANS.

Figure 5.5 shows how many bacterial cells are on the ANS in terms of percentage (%) and contact angle via pore size of ANS. The figure represents two main results: the rectangular shape data point represents the ‘before repelling’ condition and the circular data point indicates the ‘after repelling’. The result of before repelling

Table 5.2. Percentage of adhered bacterial cells before and after repelling experiment on various pore size of the ANS

Pore size (nm)	Before repelling experiment		After repelling experiment	
	Avg. percentage of adhered bacteria cells (%)	Stdv	Avg. percentage of adhered bacteria cells (%)	Stdv
0 (no pore)	25.07	6.14	23.62	5.25
30	17.37	3.25	2.65	0.62
55	16.56	4.41	4.09	1.85
70	6.78	2.52	2.41	0.91
80	5.64	1.69	2.92	1.80

clearly shows that the percentage of bacterial cells decreased almost linearly with increase in the pore size. As the inset in figure 5.5 shows, the contact area between the bacteria and the ANS decrease with increasing the pore size of ANS. This means that the adhered cells decreased with the decrease in the contact area. The 0.33 μm^2 , 0.44 μm^2 , 0.57 μm^2 , 0.7 μm^2 , and 0.79 μm^2 contact area showed 5.64 %, 6.78 %, 16.56 %, 17.37 % and 25.07 % cultured bacterial cell on ANS, respectively. This result confirms that a large contact area can lead to the increase in probability for bacteria to grab the ANS surface during cell culturing.

As a result of the ‘after repelling’ condition, the percentage of bacterial cells is dramatically decreased between no pore and 35 nm pore size ANS, and there is no visible difference in the percentage of bacterial cells via contact area. It has been reported that a substrate which has low surface energy will have a high contact angle in deionized water ¹⁵⁹. This means that the contact angle can represent the degree of surface energy of a substrate. From the contact angle measurement on the ANS in figure 5.5, it is noted that the surface energy of the ANS decreased with increasing pore size. As

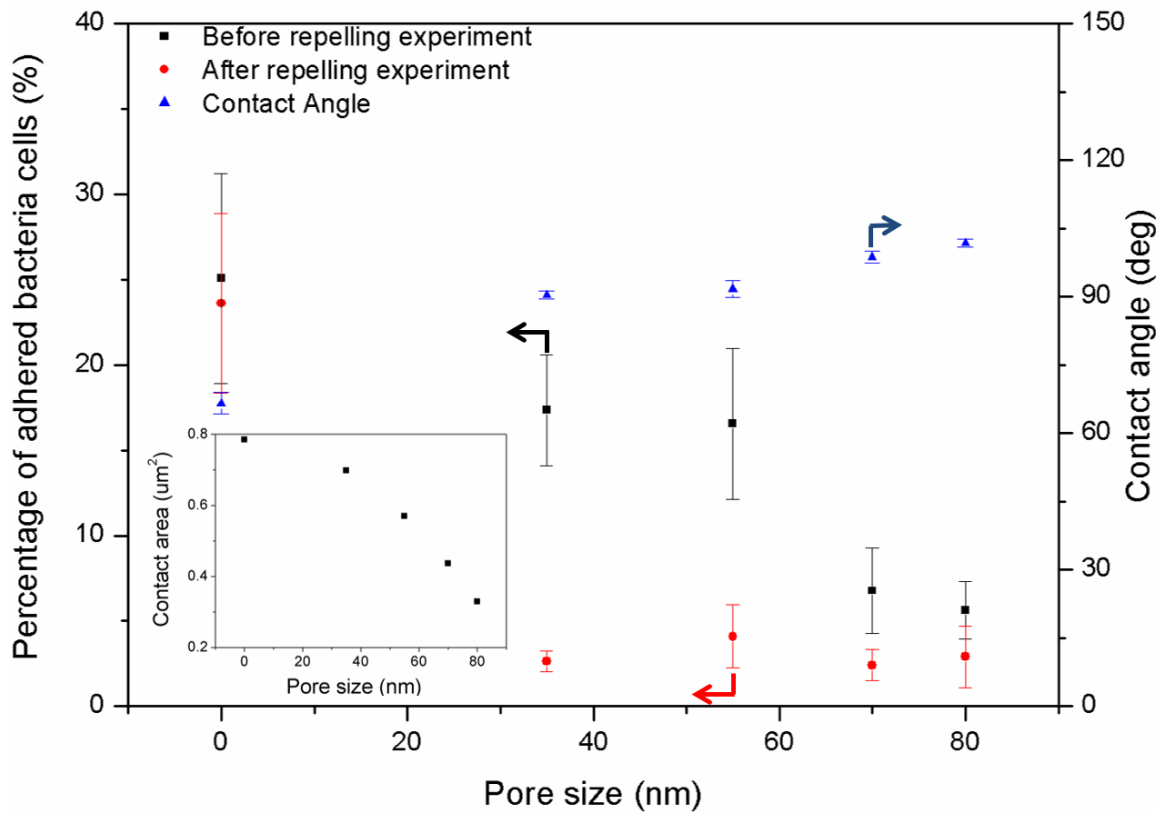


Figure 5.5. Percentage of adhered bacterial cells on alumina nanopore structure (ANS) and the contact angle via pore size. The inset graph shows a relation between the pore size and the contact area. The contact area decreased with pore size increase. Left side y-axis represents the result of bacteria repelling experiment. Right side y-axis indicates the result of contact angle measurement. Arrows designate each assigned y-axis. Error bars show standard deviation with one sigma.

discussed above, increasing the pore size represents decreasing the contact area. In other words, the contact angle decreased with increasing contact area.

This contact angle trend shows opposing results on the percentage of adhered bacterial cells. There is the contact angle decrease significantly between 0 nm (no pore) and 35 nm pore size; except that, there are slight increases of the contact angle with an

increase in the pore size. As mentioned, there is no significant difference in the percentage of adhered bacterial cells between 35 nm and 80 nm pore size after the repelling experiment: the 66.62 degree, 90.41, 91.71, 98.70, and 101.83 degree contact angle condition showed 23.62 %, 2.65 %, 4.09 %, 2.41 %, and 2.92 % bacterial cell on ANS, respectively. It appears that the bacterial adhesion, which is against the repelling force relates to the surface energy which is represented by the contact angle. A combination of a larger contact area and a smaller contact angle can make surface hold more bacterial cells. This is because of not only the capability for additional contact area between bacterial cells and the ANS, but also the high surface energy as represented by a low contact angle. The gap between the “before repelling” and “after repelling” experiment, in figure 5.5, indicates how many bacterial cells are removed by the repelling experiment. The 0 nm (no pore), 35 nm, 55nm, 70 nm, and 80 nm pore size show that the percentages of repelled bacterial cells are about 5.80 %, 84.76 %, 75.29 %, 64.54 %, and 48.27 % respectively.

According to the results of the percentage of adhered bacterial cells, the adhesive strength of bacterial cells is the combination of the capability of the contact area and the surface energy. Specifically, the initial adhered bacterial cells can be mainly predicted by the contact area between the bacterial cell and the ANS and the bacteria’s repelling performance can be primarily determined by the surface energy of the ANS. The strength of bacterial adhesion depends heavily on the surface energy of a substrate. A substrate that has low surface energy can easily repel the bacterial cells from its own surface.

5.5. Summary

This chapter discussed that the performances of bacterial adhesion and repelling were affected by the existence of the contact area between the cell and the surface of ANS. The ANS were fabricated using a two-step aluminum anodizing method. In order to study the repelling performance, a centrifugal experiment was conducted. After the repelling experiment, the percentages of adhered bacterial cells were measured. The initial existence of cultured bacterial cells on ANS and the strength of bacterial adhesion on ANS were examined with various pore sizes. The bacterial cells were cultured on ANS with different pore sizes. Contact angles were measured and the contact area between a bacterial cell and the ANS was calculated for analyzing the mechanism of bacterial adhesion. It was found that ANS can reduce the initial existence of cultured bacterial cells and the strength of bacterial adhesion compared to a smooth surface. ANS can have a less accessible area than a smooth surface due to the pores. It means that the ANS has bacteria repelling behavior. This study suggests that ANS can be successfully designed for biocompatible material which can restrict bacterial adhesion, and can improve medical treatment as a biomaterial with discussed two critical parameters: contact angle and contact area.

CHAPTER VI

ELECTROCHEMICAL PROPERTIES OF NANOPORE STRUCTURES AND THEIR INFLUENCE ON ION-TRANSFER*

The electrochemical performances of the nickel based hexagonally ordered self-organized metallic nanopore structure (MNS) are investigated by various pore diameters in this chapter. The experiments for Cyclic Voltametry (CV) and Electrochemical Impedance Spectroscopy (EIS) measurements are conducted by electro-potential stat using the MNS to investigate the performance of energy store and ion transfer. This chapter will discuss about our study that reveals the critical parameters affecting electrochemical property of the MNS.

6.1. Morphological analysis

The surface morphology of MNS is observed using the FESEM which was described in Chapter III. Figure 6.1 shows the MNS with different pore sizes. As shown in the Figure 6.1.a through 6.1.c, the average pore diameters are 168 nm, 253 nm, and 348 nm. These images clearly show that all MNSs are highly ordered in nanoscale hexagonal shape. The oblique angle view of Figure 6.1.c of 348 nm pore MNS is in Figure 6.1.d. The thickness of those pore walls is about 300 nm.

* Part of this chapter reproduced with permission from “Enhanced-Ion Transfer via Metallic-Nanopore Electrodes” by Sunghan Kim, et al., Journal of The Electrochemical Society, Vol.161 (10), A1475-A1479, 2014 (Copyright © 2014, The Electrochemical Society)

6.2. Cyclic voltammetry (CV) study

The CV measurement has been widely used for kinetics study in electrochemical reactions⁸¹⁻⁸³. The CV diagrams represent ion formation in electrode and migration to electrolyte and vice versa. The behavior of ion transfer between an electrode and an electrolyte dominates to the formation of a CV diagram in terms of fat vs thin. The current peak of a CV diagram depends on the formation of electrochemical double layer, which includes ions^{160, 161}. The CV diagrams

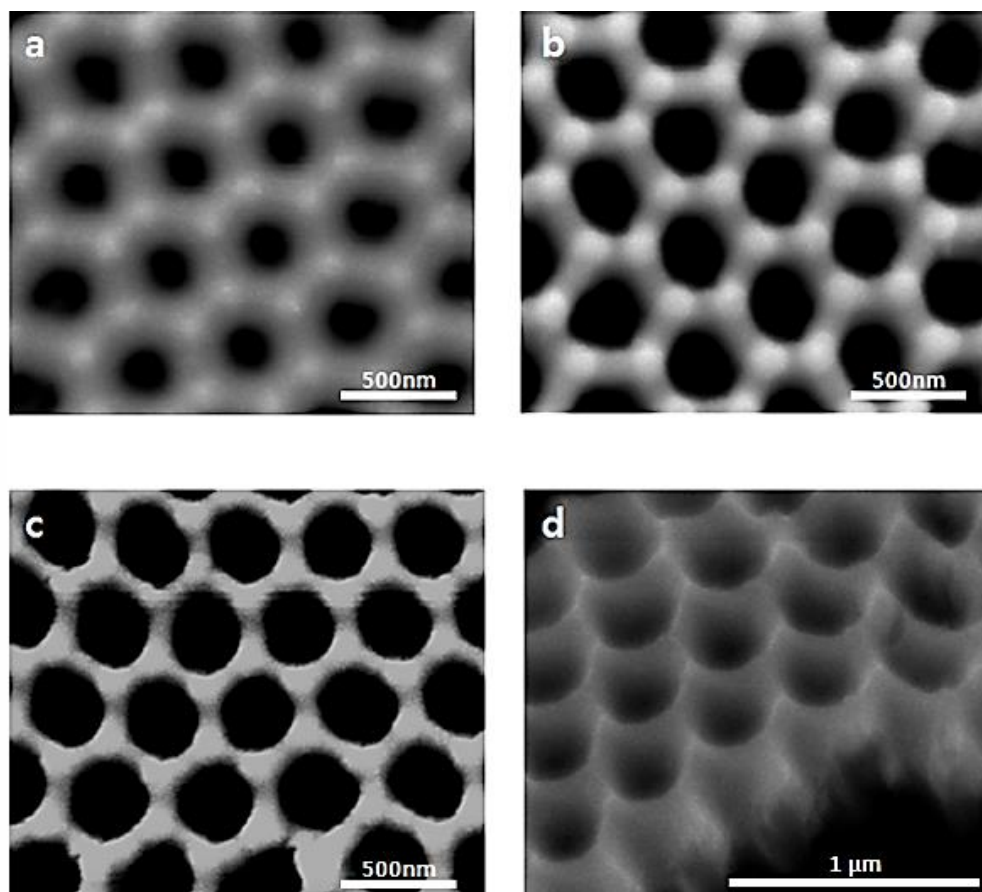


Figure 6.1. SEM images of MNS with various pore diameters: the pore diameter are about (a) 168 nm, (b) 253 nm, (c) 348 nm. The cross section view of 348 nm pore size MNS is on image (d).

are obtained using the three-electrodes-electrochemical setup. The anodic and cathodic limits shown in the CV diagrams were produced in an ionic liquid during the electrochemical reaction on electrodes^{84, 162}. Figure 6.2 shows CV result from different pore diameter sample of MNS: 168 nm, 253nm, and 348 nm. As shown in the figure, all MNS samples exhibit two pairs of redox peaks: oxidation peak and reduction peak. These redox peaks are related to the electrochemical reaction between the MNS and electrolyte¹⁶³. Once the nickel based MNS has contact with aqueous alkali electrolyte, it is covered with a nickel hydroxide^{164, 165}.

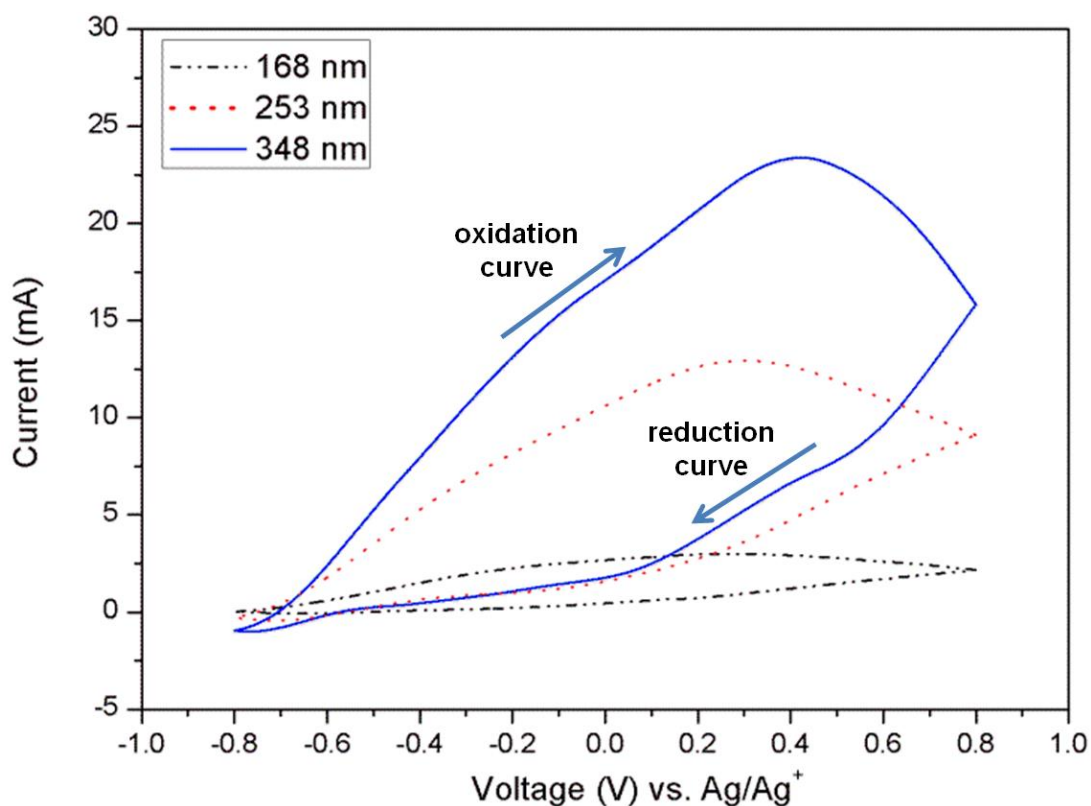
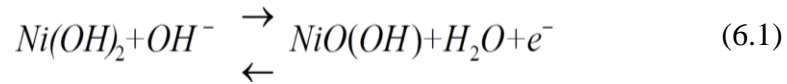


Figure 6.2. Cyclic voltammetry curves of MNS with various pore size: 168 nm, 253 nm, and 348 nm 1M potassium hydroxide (KOH) as an electrolyte.

oxidation and reduction peaks correspond to following electrochemical reaction ¹⁶⁶ :



Both the amplitude of oxidation and reduction peaks increase with increasing the MNS pore diameter. The MNS of 168 nm, 253 nm, and 348 nm pore sizes has the oxidation peak currents at 3.00 mA, 13.4 mA, and 23.7 mA, respectively. The 168 nm, 253 nm, and 348 nm pore size MNS have the reduction peaks at -4.2×10^{-4} mA, -4.3×10^{-1} mA, and -1.00 mA, respectively. The figure clearly shows that the behavior of ion transfer is influenced by the pore diameter of MNS. This study demonstrated that how the effective surface area affect electrochemical reaction behavior. The oxidation current increases with increasing pore diameter. Details will be discussed below. The pore diameter of highly ordered MNS can affect to the surface area alteration. At this case, the increase in pore size leads to the surface area increasing and reduces the resistance of MNS for electro chemical reaction, eventually. This will be discussed in the following.

6.3. Identifying electrochemical double layer on MNS

Understanding the fundamental mechanisms of electrochemical double layer is the first step for analysis. For energy storage applications, it is important to understand the Faradaic reactions as well as electrochemical double layer. It has been reported that the shape of a CV diagram reflects Faradaic reaction and electrochemical double layer ^{167, 168}. According to the study by Lee et. al., fast redox reaction accompanied Faradaic

reaction indicates the electrical potential dependent capacitance alteration from the CV curve. Wang et. al. referred that the charging and discharging process of electrochemical double layer shows the corresponding current peak of the electrical potential in the CV curve. According to our CV results shown in Figure 6.2, there are three different shapes observed. The structure of 168 nm pore size has the narrowest shape while the 348 nm the fattest. The area inside the CV circle represents the amount of energy stored.¹⁶⁹. As shown in the figure, the MNS with 348 nm pore diameter can store the most energy among all. The mechanism of energy storage is related to the ion transfer. There is an advantage to enhance the energy store of the nanopore electrode in Faradaic reaction¹⁷⁰. The density of energy can be increased in the nanopore electrode due to Faradaic reaction, i.e., fast redox reaction for pseudo-capacitance¹⁷¹. An electrochemical double layer is generated at the interface between metal electrode and electrolyte¹⁷²⁻¹⁷⁴. The ion transfer which is the main driving force for electrochemical reaction takes place at the electrochemical double layer. The stern-model is currently used for explanation about the electrochemical double layer and this model. The stern-model stated that there is a stern layer which composed mostly cations nearby electrode through diffusion¹⁷⁵. Based on our results obtained on MNS, a schematic diagram of the electrochemical double layer is illustrated as shown in Figure 6.3. The stern plane is formed parallel adjacent to the interface. By the stern plane, the electrochemical double layer is divided by two layers: stern and diffusive mobile layers¹⁷⁶.

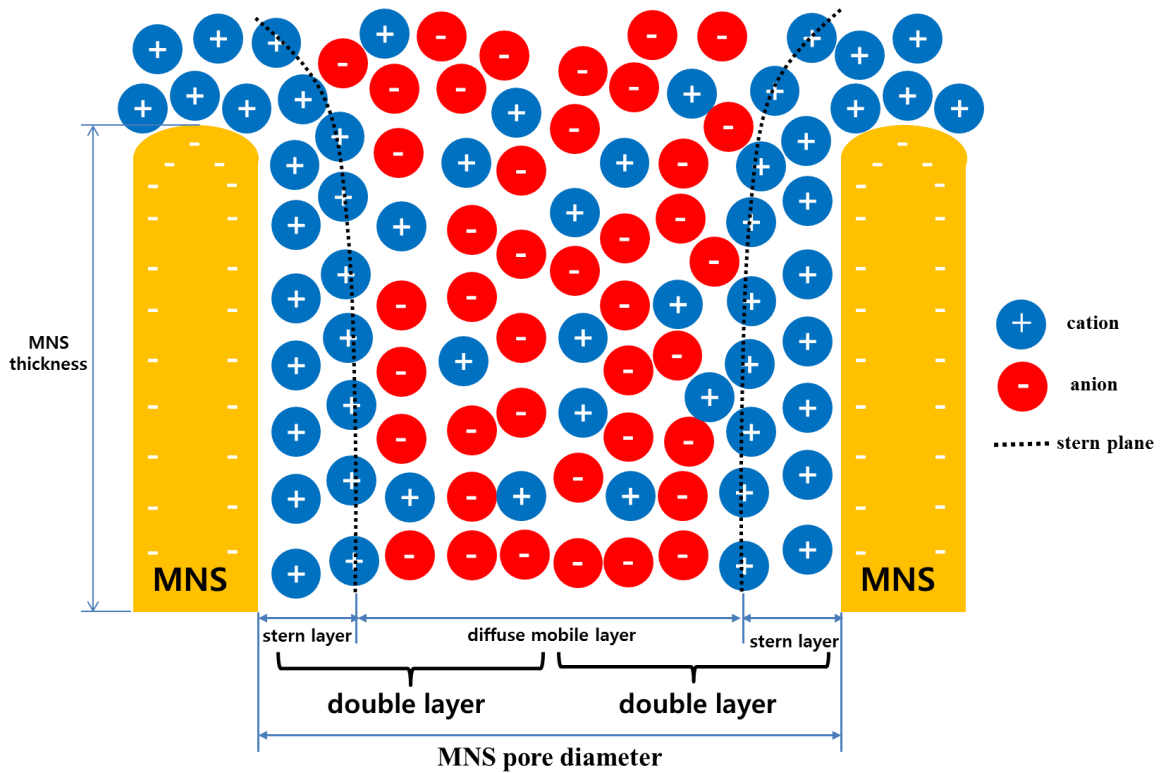


Figure 6.3. Schematic diagram of electrochemical double layer at the MNS and electrolyte interface.

The ions, mostly cations, are adhered to the interface and hardly moved at the stern layer. At the diffusive mobile layer, the ions are not attracted to the surface but freely movable, i.e. mobile. As shown in the figure, the MNS looks like three-dimensional shapes and the ion accessible surface area at the interface depends on the pore diameter and the thickness of MNS.

6.4. Calculation effective surface area

The effective surface area (ESA) was calculated in order to understand the electrochemical reaction under the condition of various surface areas. For a specific

sized electrode, the performance of its energy storage depends on the total surface area. A large total surface area of an electrode enhances the ion transfer and thus the capacitance improvement. Furthermore, the ESA become a critical and universal factor as a unit parameter to estimate the energy storage capacity when comparing electrodes of different sizes. Figure 6.4 shows the schematic diagram of the ESA for electrochemical reaction on the MNS. Here this study defines an ESA as the hexagonal shape that is extracted from SEM image by connecting 6 center point of each pore. The ESA of the MNS is represented by the following equation:

$$\Gamma(r) = -3\pi r^2 + 6\pi h r + \frac{3\sqrt{3}}{2} d^2 \quad (6.2)$$

$$\Gamma'(r) = -6\pi r + 6\pi h \quad (6.3)$$

where Γ is ESA, d is the interpore distance of pore to pore, r is the radius of the pore, and h is the thickness of MNS. Both the interpore distance and the thickness of MNS are fixed as a constant value among all MNS samples. The value of interpore distance ' d ' and the thickness ' h ' is 500 nm and 300 nm, respectively. In case where of both ' h ' and ' d ' are constants, the only variable of equation (2) is ' r '. Using the first and second derivative form from an original equation (2), it is possible to determine that the function has a locally maximum or minimum value at given critical point. From the equations (3), the Γ (ESA) has the maximum area when the radius ' r ' is equal to its thickness ' h '. The value of Γ (ESA) and total surface area of each sample are shown in table 6.1. In this table, the Γ (ESA) increases with increasing pore diameters. Among

three types of pore diameters, 348 nm pore diameter sample has the largest area of $134.81 \times 10^4 \text{ nm}^2$. The total surface areas of each MNS are calculated as ‘apparent area of working electrode (0.25cm^2)’ multiply

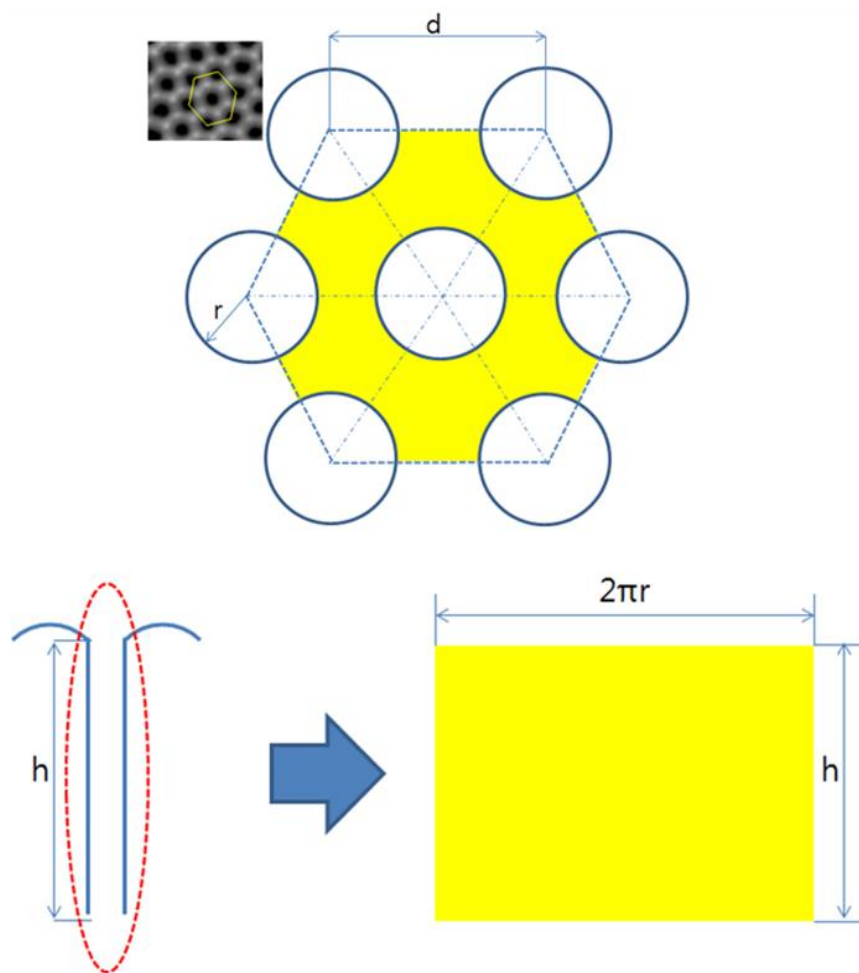


Figure 6.4. Schematic diagram of the effective surface area (Γ : ESA) for electrochemical reaction on the MNS.

by ‘the ratio of each Γ (ESA) to unit area of hexagonal shape (64.95×10^4)’. Increasing the Γ (ESA) leads to the increase in total surface area of MNS, eventually, it affects to enhance the ion transfer and energy store.

Table 6.1. Calculated effective surface area (Γ : ESA) and corresponding total surface area of MNS with various pore diameters.

pore diameter (nm)	radius 'r' (nm)	effective surface area $\Gamma(r)$ (nm ²)	total surface area (cm ²)
0 (no pore)	0	64.95×10^4	0.25
168	84	105.80×10^4	0.41
253	126.5	121.40×10^4	0.47
348	174	134.81×10^4	0.52

6.5. Electrochemical impedance spectroscopy (EIS) analysis

In order to understand the impedance data of MNS, the Nyquist plot was obtained. The Nyquist plot can be used to determine electrochemical resistance through the plotted semi-circle diameter. Figure 6.5 is the Nyquist plots of MNS with various pore sizes. As shown in the figure, the radius of each curve decreases with the increasing pore diameter. This means that the total impedance decreases as the pore diameter increases. The inset in figure 6.5 shows the Nyquist plot of a flat surface as a reference, the curve radius of the flat sample is much larger than that of any MNS's. As shown in Table 6.1, the increasing pore diameter leads to the expansion of the Γ (ESA). The main reason of decreasing impedance relates to increased Γ (ESA) of MNS. The increasing Γ (ESA) enhances the electrochemical reaction¹⁷⁷. According to the inset graph of figure 6.5, the Γ (ESA) continues to increase with the increasing pore diameter until the value of the radius is the same as the thickness. This means that the increasing surface area is favorable for ion transfer while the Γ (ESA) is the optimized dimension.

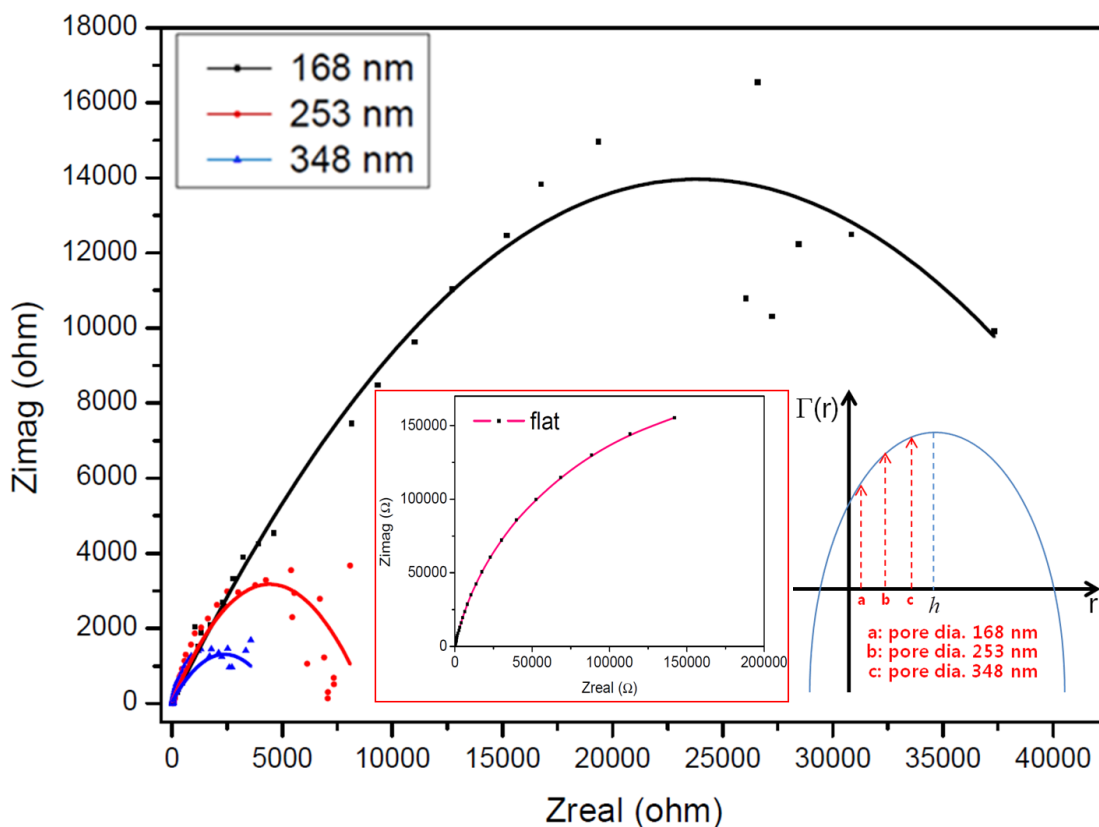


Figure 6.5. Electrochemical impedance spectroscopy (EIS) data with Nyquist plots of MNS with various pore size: 168 nm, 253 nm, and 348 nm in the 1M potassium hydroxide (KOH) as an electrolyte.

Figure 6.6 shows both Bode impedance plots and bode phase plots. The Bode impedance plots (Figure. 6.6.a) show that the impedance of MNS decreases as pore size increases. Moreover, the Bode phase plots (Figure. 6.6.b) show that the magnitude of depression angle increases with the increasing pore size. All EIS results clearly indicate that a larger Γ (ESA) of the MNS is desirable for enhanced electrochemical reaction resulting effective ion transfer.

These EIS results were obtained on samples with small pore size (radius less than thickness) are shown in figures 6.5 and 6.6. A parameter, i.e., Γ (ESA), was found

to be important for ion transfer. This was evidenced when the pore size was smaller than thickness. Since the ESA is an extrinsic property, i.e., volume related, it is important to find out the range of its usefulness. To answer the question, will the Γ (ESA) still works when the pore size is larger than the thickness, EIS experiment was conducted by aluminum-based micropore structure instead of MNS. Since there are two issues: fabricating issue and identifying universal validity of ESA. The first fabrication issue is from clogging. In the case of MNE, the pore-to-pore distance is about 500nm. To fabricate the MNE with a larger radius (r) than its thickness (h), the deposition depth should be smaller than 250 nm (half of pore to pore distance). However, as figure 6.7 shows, the pore diameter of the MNE is not the same as its substrate (porous alumina structure) because the nickel molecules are gradually covered and clogged to its original pore shape. It is difficult to control the pore radius during the deposition. Thus, the possible deposition depth, which is smaller than pore radius, is much smaller than 250 nm. As the thickness of MNE decrease, the MNE's shape cannot be firmly maintained and it is difficult to do an experiment using them. The second is that the hypothesis about universal validity of ESA definition is based on the geometry and dimension. To prove this, the behavior of ESA dependent electrochemical reaction should be identified by different scale.

Larger pores on an aluminum substrate were successfully fabricated using a simple punch method. The interpore distance is 500 μm and pore diameters are larger than its thickness (25 μm): 120 μm , 240 μm , and 350 μm . EIS experiment was performed by same experimental conditions with MNS EIS experiment.

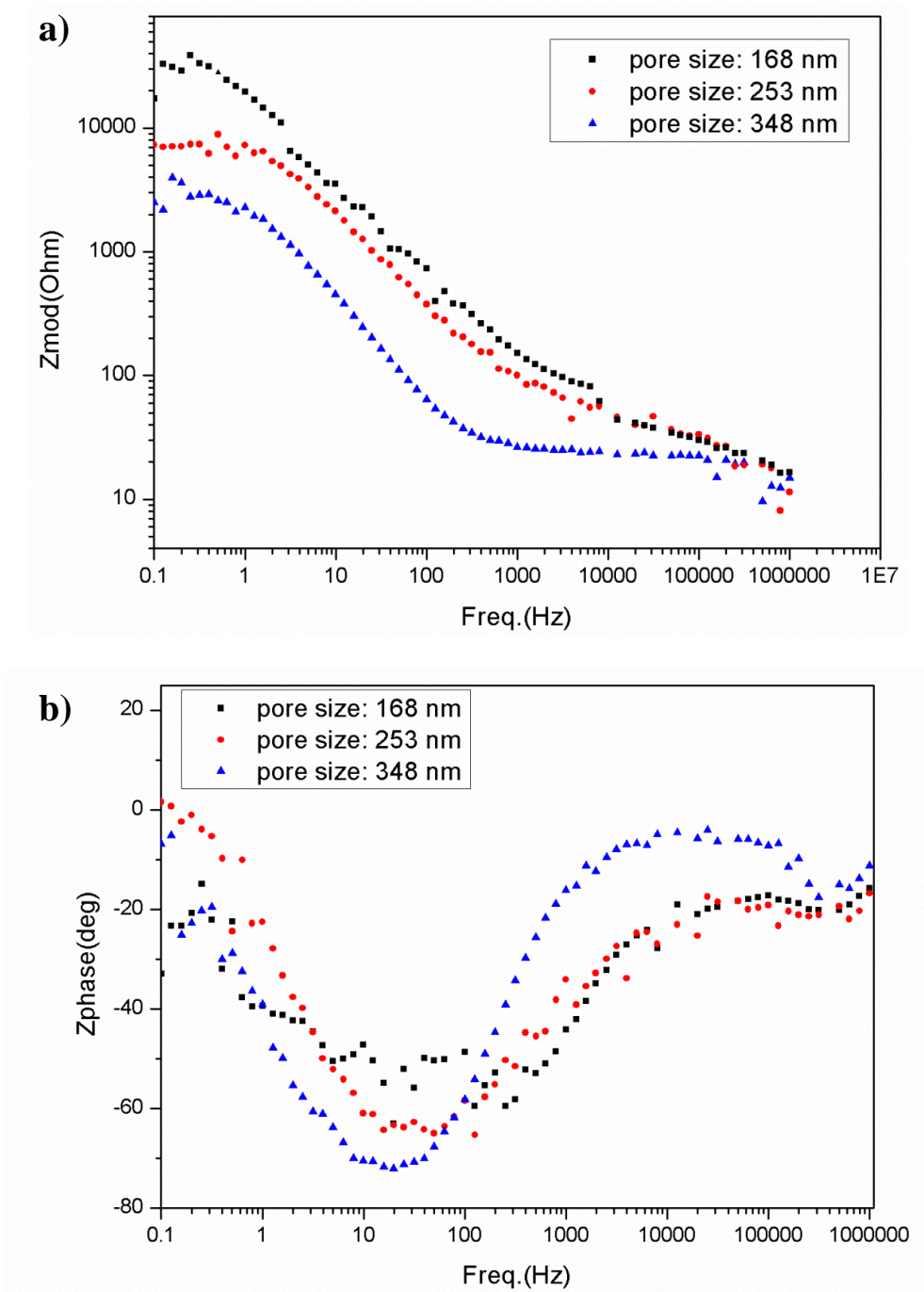


Figure 6.6. Electrochemical impedance spectroscopy (EIS) data with both a) bode impedance plots and b) bode phase plots of the MNS with various pore diameters: 168 nm, 253 nm, and 348 nm.

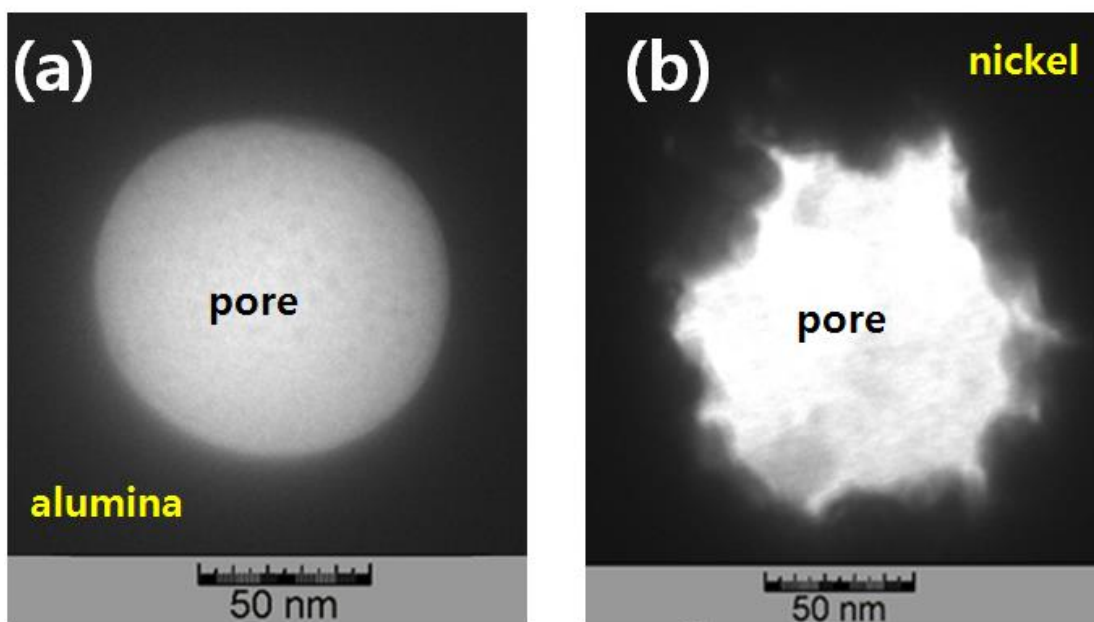


Figure 6.7. TEM images of single pore in (a) porous alumina and (b) MNE.

Figure 6.8 shows that the radius of each curve increases with the pore diameter increasing. This means that the total impedance increases with the increase of pore diameter. In other words, the electrochemical reaction is decreased by reduced ion transfer with increasing pore diameter. This is because the Γ (ESA) is decreased as increasing pore radius of metallic micropore electrode when the pore size is larger than the thickness. As shown in the inset graph of figure 6.8, the Γ (ESA) keeps decreasing as pore radius increasing after the point of 'h'; thickness of electrode. The represented image of metallic micropore structure is shown at the bottom of figure 6.8 (scale bar is 300 μm). The 120 μm , 240 μm , and 350 μm diameters show that the values of Γ (ESA) are $64.39 \times 10^4 \mu\text{m}^2$, $57.04 \times 10^4 \mu\text{m}^2$, and $44.34 \times 10^4 \mu\text{m}^2$, respectively.

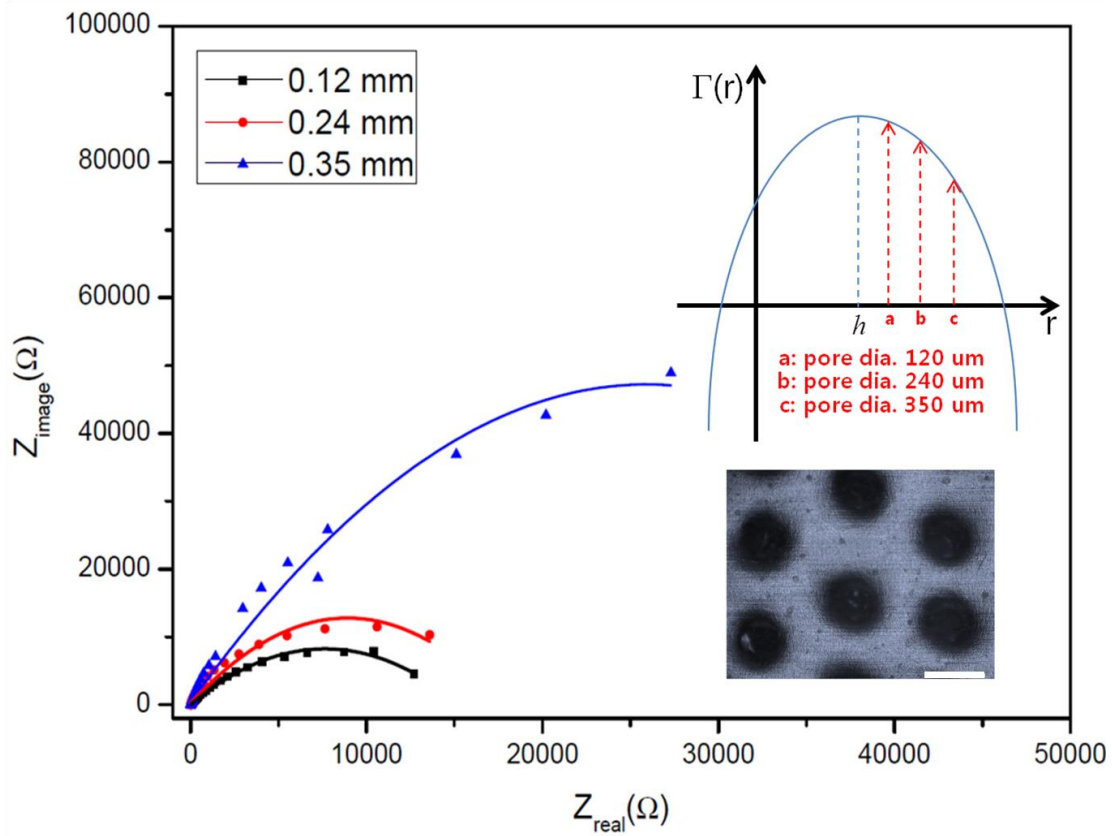


Figure 6.8. Nyquist plots of aluminum based metallic micropore electrode with various pore size: 120 μm , 240 μm , and 350 μm in the 1M potassium hydroxide (KOH) as an electrolyte. (Inset image scale bar: 300 μm).

As discussed above, a new parameter, Γ (ESA) was proposed that is critical for ion transfer. The value of Γ (ESA) depends on the relation between the thickness and pore diameter. When the pore size is the same as its thickness, the value of surface area is optimized. The Γ (ESA) keeps increasing with increasing pore radius when the range of radius is smaller than thickness. When the range of MNS pore radius is larger than its thickness, then the Γ (ESA) keeps decreasing with increasing pore radius. Ion transfer can be optimized through Γ (ESA). The Γ (ESA) can be optimized through design of the

MNS structure with dimensions such as interpore distance 'd' and the thickness 'h'. The pore radius cannot be larger than the half of interpore distance 'd'. The direct evidence of effects of Γ (ESA) on ion transfer can be seen in Figure 6.9. It shows current-voltage characteristics of MNS with various pore diameters. The current-voltage curves are obtained with a 1M sodium chloride (NaCl) electrolyte. The scan rate is 100mVs^{-1} and scan range is from -1.5 V to 1.0 V. As shown, the improvement of electrical current generation is a result of increasing the pore diameter of MNS. This result also clearly shows that the performance of ion transfer is enhanced by increasing Γ (ESA) of MNS.

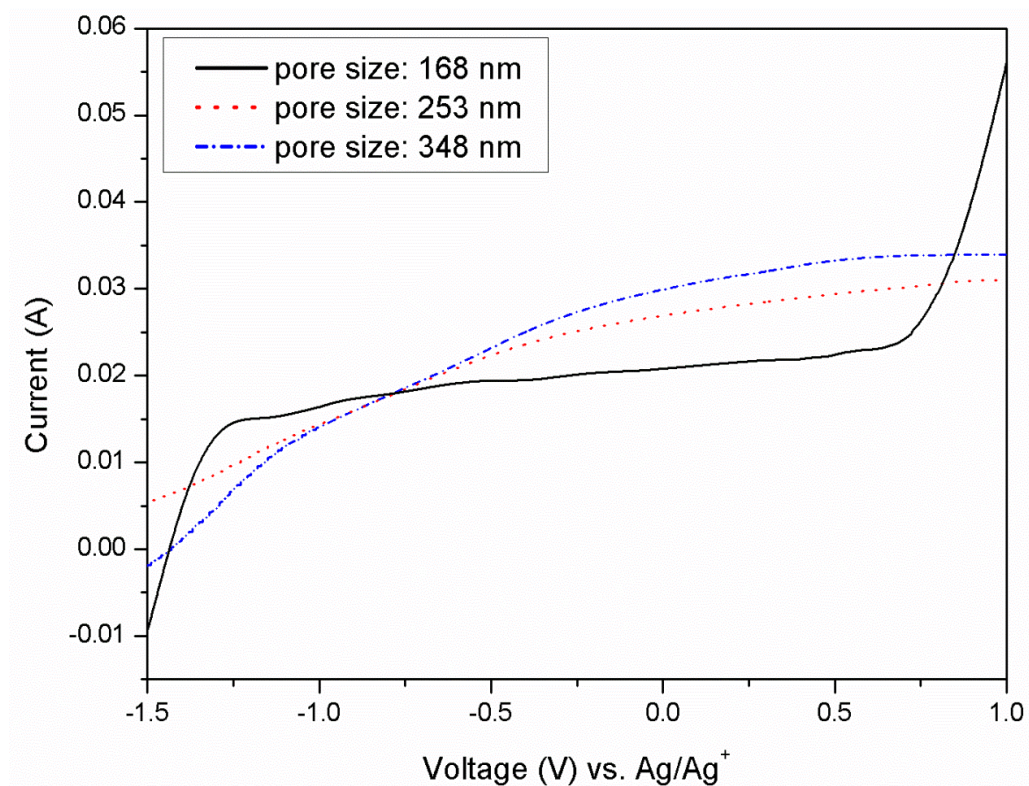


Figure 6.9. Observed current-voltage curves of the MNS with various pore diameters: 168 nm, 253 nm, and 348 nm in the 1M sodium chloride (NaCl) electrolyte.

6.6. Summary

In this chapter, the highly ordered self-assembled nickel-based metallic-nanopore structure (MNS) was studied for the application in ion transfer. Using two step aluminum anodizing and E-beam evaporating, the various pore sizes of MNS were fabricated and their electrochemical behaviors were examined. Results clearly indicated that the behavior of ion transfer was influenced by the pore diameter of MNS. This study revealed the critical parameter that can affect to electrochemical property of the MNS. The effective surface area (ESA) was derived as the critical parameter to optimize the design for ion transfer. Increased ESA enhanced the electrochemical reaction of the MNS as the electrode. As discussed, the MNS is able to control the electrochemical reaction performance further it is desirable to design of enhanced ion transfer electrode or membrane for energy devices.

CHAPTER VII

(ELECTRO-)WETTING BEHAVIOR

The wettability and electrowettability of nanopore structures are examined in this chapter. Using a droplet shape measurement system, the contact angle between water droplet and metallic nanopore structures with various pore size will be evaluated. In order to analyze the wettability of MNS in terms of contact angle, wetting model will be established. The electrowetting effect on MNS will be investigated by applying electrical potential into the MNS from 0 V to 20 V. The correlation between contact angle and pore size of MNS can be used as a critical parameter for understanding surface wettability/electrowettability.

7.1. Wettability of MNS via pore size

The wettability was characterized by contact angle measurement with a water droplet on the top surface of the MNS. The fabricating method of MNSs and experimental details for wettability were described in Chapter III. In order to understand the fundamental wettability of MNSs, the contact angle between a water droplet (2 μ l) and a given MNS was investigated as a base study. A nickel-based MNSs were used with various pore sizes, in terms of diameter 154 nm, 258 nm, and 379 nm, as shown in the scanning electron microscope (SEM) images in Figure 7.1. A substrate with low surface energy including high contact angle with deionized water is hardly wetted, and vice versa¹⁵⁹. This means that the contact angle reflects the degree of wettability of a

substrate. By investigating the MNS's contact angle in terms of pore size, it is possible

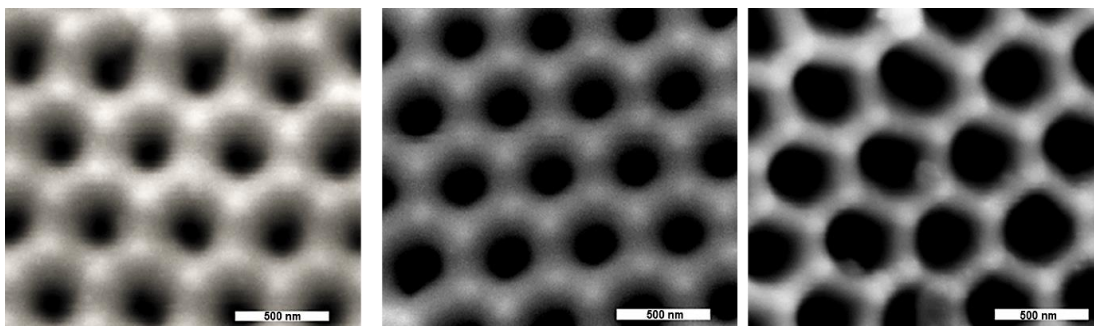


Figure 7.1. SEM images of MNS with various pore sizes: (a) 154 nm pore size, (b) 258 nm pore size, and (c) 379 nm pore size.

to understand the behavior of wettability in the MNS. Figure 7.2 represents the behavior of contact angles in terms of a MNS's pore size. MNSs with pore sizes of 0 nm (no pore), 154 nm, 258 nm, and 379 nm presents contact angles of 84.5° , 95.0° , 106.5° , and 120.0° , respectively. As Figure 7.2 illustrates, increases in pore size led to the increases in contact angle. This indicate that the wettability of a MNS depends on its pore size.

These results agree with the published data^{178, 179}.

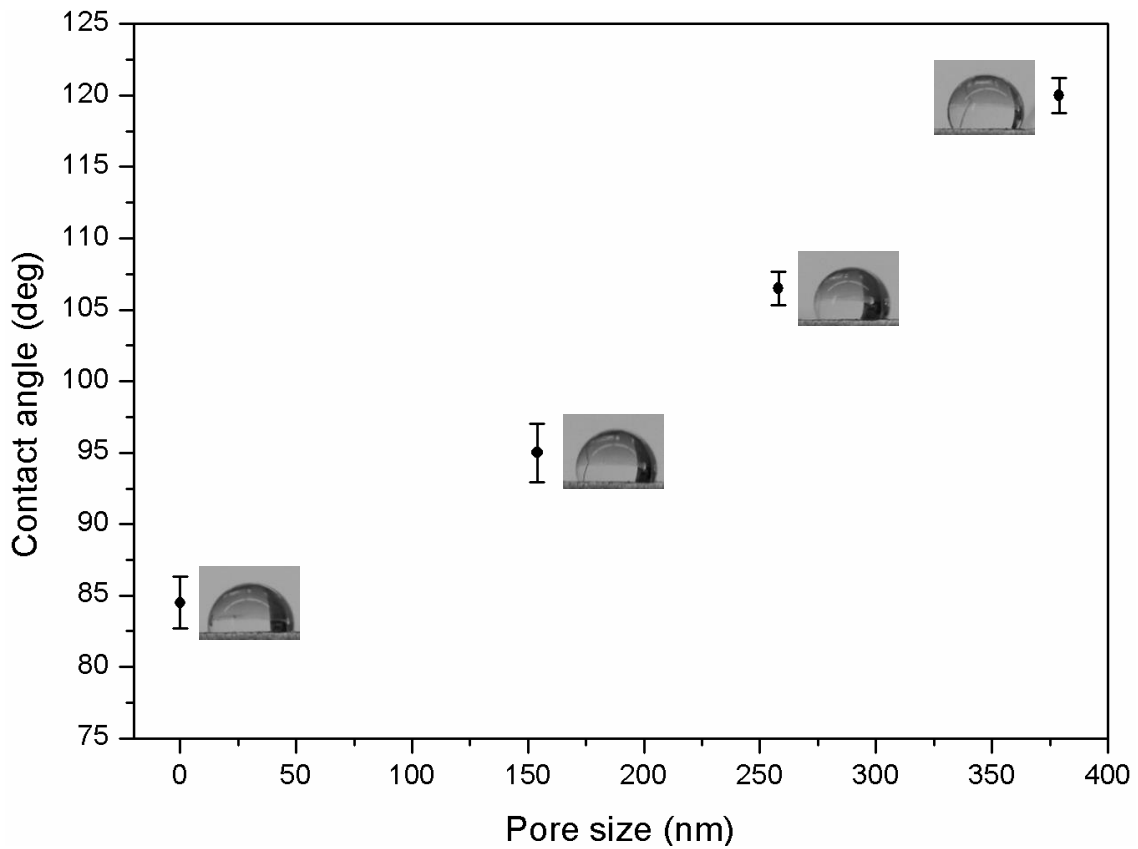


Figure 7.2. Intrinsic contact angle of MNS with 2ul water droplet on top surface of MNS. Error bars show standard deviation with one sigma. Error bars show standard deviation with one sigma.

7.2. Numerical analysis of wettability on MNS

By using the energy balance concept, it is possible to solve the wettability of heterogeneous surfaces¹⁸⁰. Based on both the energy balance concept and Young's equation, the wetting model for MNS can be defined with geometrical factors of a liquid droplet on MNSs. In order to establish a basic wetting model for MNS, the surface net energy of a flat surface (a nonporous surface with no texture) should be considered. By combining the surface net energy on both the flat surface and the MNS, the following final equilibrium equation can be obtained^{181, 182}:

$$\cos\theta^* = \frac{[(S_1^* + f_{l-s})\cos\theta + S_2 - S_2^* - f_{l-v}]}{S_1} \quad (7.1)$$

where θ^* is the apparent contact angle between a MNS and liquid droplet, S_1 is the area of liquid-solid interface on a flat surface, S_1^* is the area of liquid-solid interface on a MNS, f_{l-s} is the area of liquid-solid from a nanopore shape, θ is the intrinsic contact angle between a flat surface and liquid droplet, S_2 is the area of liquid-vapor interface on a flat surface, S_2^* is the area of liquid-vapor interface on a MNS, and f_{l-v} is the area of liquid-vapor in a nanopore shape. All these variables can be verified by using the geometry of a liquid droplet on a surface. Figure 7.3 shows the geometry of a liquid droplet on a surface. S_1 , S_1^* , S_2 , and S_2^* can be defined from Figure 7.3.a and 7.3.b:

$$S_1 = 2r \cos\left(\theta - \frac{\pi}{2}\right) \quad (7.2)$$

$$S_1^* = 2r^* \cos\left(\theta^* - \frac{\pi}{2}\right) \quad (7.3)$$

$$S_2 = 2r\theta \quad (7.4)$$

$$S_2^* = 2r^*\theta^* \quad (7.5)$$

where r is the liquid droplet radius on a flat surface (nonporous), r^* is the radius of a liquid droplet on a MNS. It is possible to resolve f_{l-s} and f_{l-v} from Figure 7.3.c:

$$f_{l-s} = z\left(\frac{2h+a-d}{a}\right)2r^* \cos\left(\theta^* - \frac{\pi}{2}\right) \quad (7.6)$$

$$f_{l-v} = \left(\frac{d}{a}\right) 2r^* \cos\left(\theta^* - \frac{\pi}{2}\right) \quad (7.7)$$

where z is the shape correction factor, a is the pore-to-pore distance (interpore distance), d is the pore diameter, and h is the absorption depth of a liquid droplet in the pore.

Figure 7.3.d represents the unit area of the MNS. The real shape of the MNS is the crown shape. Due to the shape difference between the schematic model and actual features, the shape correction factor ‘ z ’ should be considered to calculate the f_{l-s} . Figure 7.4 shows the geometric difference between the actual shape and the schematic model of

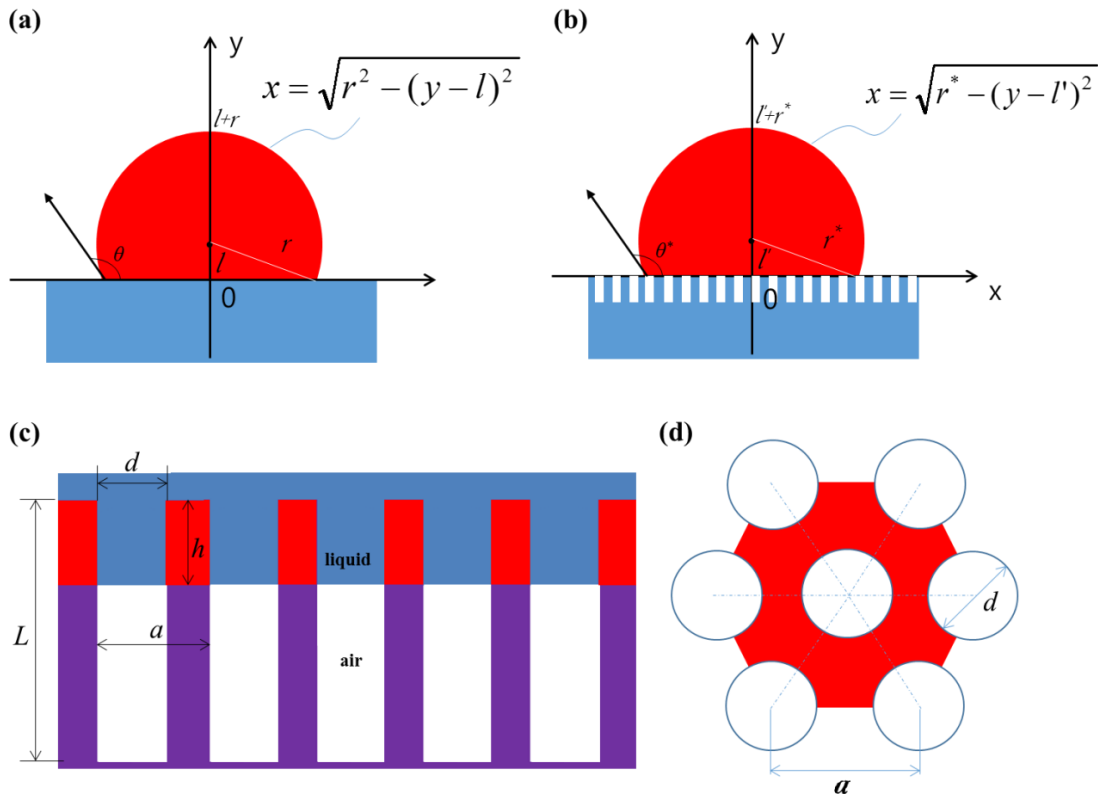


Figure 7.3. Schematic diagram of a liquid droplet’s geometries (a) on a flat nonporous surface, (b) on a MNS, and (c) in a MNS; (d) represents the unit area of the MNS.

a MNS. The shape correction factor ‘ z ’ can be determined under the assumption that the length of the outline of the crown shape is the same as the length of the outline of the triangle shape by:

$$z = \frac{2(h - t) + \sqrt{(a - d)^2 + 4t^2}}{a - d + 2h} \quad (7.8)$$

where t is the distance from the top to the bottom of the crown shape. As Figure 7.4.a shows, the height value of t is about 300 nm. It is assumed that the value is fixed for all other pore size structures.

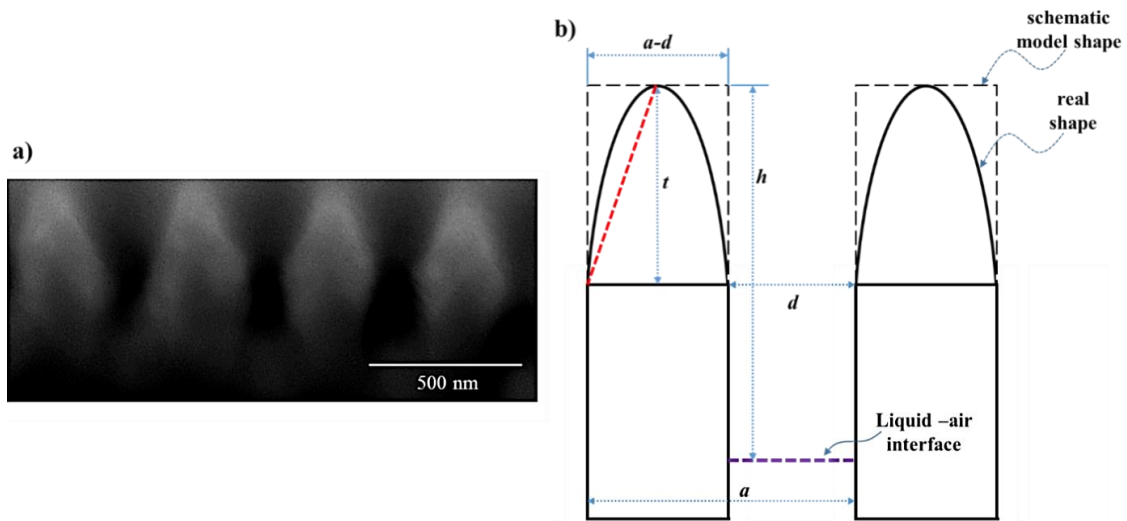


Figure 7.4. SEM image and schematic diagram for calculating the area of the liquid-solid interface at the nanopore shape and the area of liquid-vapor interface in the nanopore shape. The SEM image in a) shows a cross-section of a MNS, and b) is the geometry of cross-section of a pore shape.

The absorption depth of the liquid droplet in the pore can be expressed under the assumption that the size of the single pore is much smaller than the size of the liquid droplet ¹⁸³:

$$h = \frac{4L\gamma \cos\theta}{P_0 d + 4\gamma \cos\theta} \quad (7.9)$$

where P_0 is atmospheric pressure, γ is the surface tension of the surface, and L is the pore depth. In order to determine f_{l-v} , it is assumed that the liquid-air interface is flat. The variables of d , P_0 , γ , L , θ , and a are all known values. Using the above equations (7.2) through (7.9), it is possible to set the equation (7.1) as a function of θ^* , r^* , and r . In order to determine θ^* , the r^* and r should be verified with the volume conditions of liquid droplets. The volume conditions are determined from figure 7.3 and figure 7.4:

$$V_{flat} = \pi \left(-\frac{(r \sin(\theta - \frac{\pi}{2}))^3}{3} + r^3 \sin(\theta - \frac{\pi}{2}) + \frac{2r^3}{3} \right) \quad (7.10)$$

$$V_{nanopore} = \pi \left(-\frac{(r^* \sin(\theta^* - \frac{\pi}{2}))^3}{3} + r^{*3} \sin(\theta^* - \frac{\pi}{2}) + \frac{2r^{*3}}{3} \right) + \alpha \left(\pi \left(\frac{d}{2} \right)^2 h \right) \frac{3}{\left(\frac{3\sqrt{3}}{2} a^2 \right)} \pi (r^* \cos(\theta^* - \frac{\pi}{2}))^2 \quad (7.11)$$

$$\alpha = \frac{a^2 h + 2d^2 (h - t)}{3hd^2} \quad (7.12)$$

where V_{flat} is the volume of a liquid droplet on a flat nonporous surface, $V_{nanopore}$ is the

volume of a liquid droplet on a MNS, and α is the volume correction factor. The α is used to determine the volume difference between the schematic model and the crown shape of the actual model. The volume of liquid droplets on both a flat nonporous surface and a MNS are the same and thus have a constant value of $2\mu l$. Wettability behavior on a MNS can be verified by calculating the θ^* , which can be numerically solved (using Matlab). All known variables are shown in Table 7.1.

Table 7.1. Value of variables for determining the contact angle of a MNS

P_0 (N/m ²)	a (m)	L (m)	θ (degree)	t (m)	γ (N/m)	V (m ³)
101300	500×10^{-9}	1000×10^{-9}	84.5	300×10^{-9}	1.77	2.0×10^{-9}

Figure 7.5 shows the results of a simulation of the contact angle between a liquid droplet and a MNS with various pore sizes. There are discrepancies between the simulation and experiment results, but both conditions showed a consistent contact angle alteration trend as pore size increases. The surface energy variation due to oxidation effect or surface irregularities could be the major reason for the discrepancies between simulation and experiments results^{178, 184}. The deviation between simulation and experiment results is almost identical across all pore sizes. This indicates that the surface energy variation affected error occurrence in a linear manner. The simulation results could be compensated for by using the surface energy variation as an external parameter.

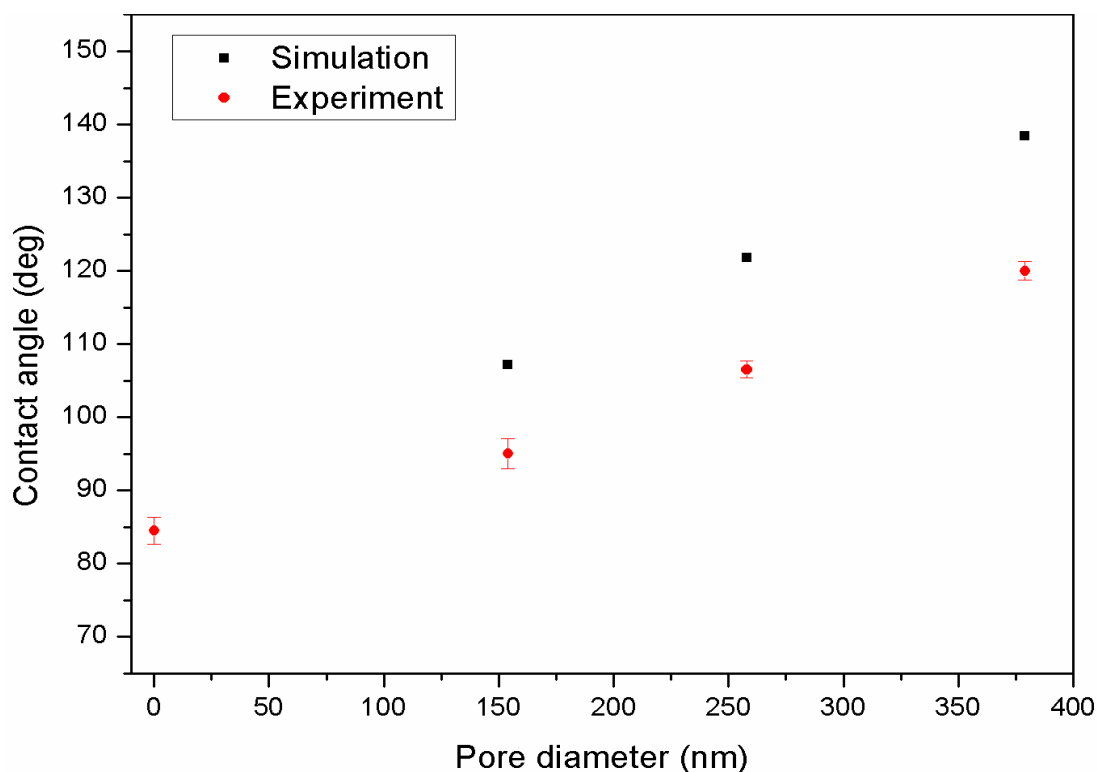


Figure 7.5. Comparison of the simulation and experiment results for contact angle determination across various pore sizes.

7.3. Electrowettability of MNS via pore size

It has been reported that the contact angle of a liquid droplet on a substrate decreases with the increase of an applied electrical potential¹²⁴. The results obtained on MNS seem to be in agreement. Figure 7.6 shows the contact angle alteration when an electrical potential was applied on the MNSs. As shown in the figure, MNSs with larger pore diameters displayed lower contact angles, with and without externally applied electrical potential. Furthermore, the contact angle decreased as the electrical potential increased from 0 V to 20 V, regardless of substrate. The decreasing trend of the contact angle, however, is different from result of flat (no pore) surface depending on the pore

sizes of the MNSs. By comparing the contact angles under 0 V and 20 V condition, the 0 nm (no pore), 150 nm, 250 nm, and 350 nm pore sizes showed that the percentage of decreased contact angles are about 20.28 %, 10.57 %, 12.27 %, and 12.68 % respectively. No saturation section occurred in contact angle behavior on the 0 nm (no pore) MNS, while the 379 nm MNS was saturated by increasing the electrical potential. These behaviors indicate that the electrowettability of MNSs can be controlled by their pore size. This issue will be analyzed in the next section.

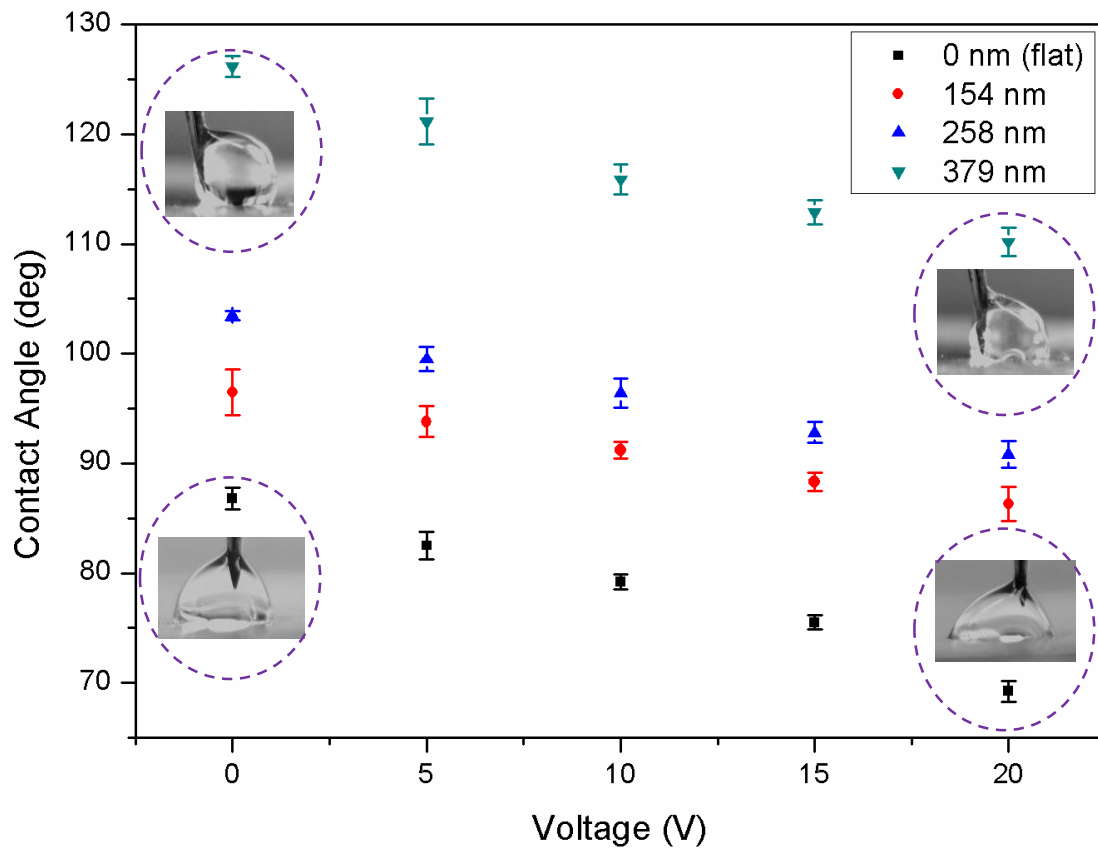


Figure 7.6. The contact angle alteration with applying electrical potential in various pore size of MNS. Error bars show standard deviation with one sigma.

The correlation between surface energy and contact angle has been defined in Young's equation ¹⁸⁵, the Cassie-Baxter model ¹²³, and the Wenzel model ¹⁸⁶. Young–Lippmann's equation is widely used to understand electrowettability ¹³⁶⁻¹³⁸. In electrowetting conditions, the wettability between a liquid droplet and hydrophobic surface can be altered from the Cassie-Baxter model to the Wenzel model by applying electrical potential ^{139, 187, 188}. These typical models are useful in predicting and comprehending the performance of any given surface's wetting/electrowetting performance. However, it is insufficient to use these equations to explain the behavior of MNSs due to the highly-ordered pores. To understand the inherent wetting/electrowetting behavior of MNSs, a new model is needed that takes into account the effect of pore structure. As stated in Chapter I, the typical electrowetting equation follows the Young–Lippmann model:

$$\cos\theta_e = \cos\theta_0 + \frac{1}{2} \frac{C}{\gamma} V^2 \quad (7.13)$$

where θ_e is the contact angle, θ_0 is the contact angle without any externally applied electrical potential, C is the capacitance of the dielectric layer, γ is the surface tension between the substrate and liquid droplet, and V is the applied electrical potential. The equation (7.13) has been widely used for understanding the electrowetting of a flat substrate. If the substrate is fixed, the main variable of equation (7.13) is the value of the applied electrical potential. The value of $\cos\theta$, according to equation (7.13), keeps increasing with increasing electrical potential on a smooth surface. In the case of MNSs,

the contact angle was saturated by increasing electrical potential, as discussed earlier. This means that, with respect to electrowetting behavior, MNSs do not follow the common Young–Lippmann model. In order to verify a modified electrowetting equation for MNSs, the effect of highly-ordered pore structures should be considered and examined. Based on both MNSs’ contact angle behavior and the Young–Lippmann model, the MNS’s modified electrowetting equation can be formulated as below:

$$\Psi = \cos\theta_0 + c_1V^2 - \kappa(V - \alpha)^2 + \beta \quad (7.14)$$

where Ψ is $\cos\theta_e$, θ_0 is the intrinsic contact angle (without externally applied electrical potential) of MNS and θ_0 depends on the pore size of MNS, c_1 is the constant which relates to both the capacitance of the dielectric layer and the surface tension of the MNS (in this case c_1 is about 6.786×10^{-4} ($1/V^2$), and V is the applied electrical potential, and κ ($1/V^2$), α (V) and β are coefficients which correspond to the pore size of the MNS. Table 7.2 shows the value of the coefficients κ , α , and β via pore size of MNS. The obtained coefficients: κ , α , and β indicated

Table 7.2. Value of κ , α and β coefficients for determining the MNS’s modified electrowetting equation in terms of pore size of MNS.

pore size (nm)	κ	α	β
0 (no pore)	0	0	0
154 ± 11	7.32E-04	6.92	2.87E-02
258 ± 12	8.44E-04	8.56	5.59E-02
379 ± 10	1.08E-03	10.74	1.09E-01

that each coefficient increased with pore size increases in a linear manner. By using this relation, it is possible to generalize the coefficients in terms of pore diameter of PMNs.

The coefficients can be determined as following equations:

$$\kappa = f_1(d) = (15.58 \times 10^2)d + 4.75 \times 10^{-4} \quad (7.15)$$

$$\alpha = f_2(d) = (17.01 \times 10^6)d + 4.26 \quad (7.16)$$

$$\beta = f_3(d) = (35.91 \times 10^4)d - 0.03 \quad (7.17)$$

where d is pore diameter of a PMN. Using the above equations (7.15) through (7.17), the Ψ can be determined by:

$$\Psi = \cos\theta_0 + c_1V^2 - f_1(d)(V - f_2(d))^2 + f_3(d) \quad (7.18)$$

According to equation (7.18) the electrowetting equation for a PMN can be generalized as a function of θ_0 , V and d .

$$\Psi = F(\theta_0, V, d) \quad (7.19)$$

As shown in figure 7.7, the experimental results of Ψ correspond to the calculation results using the modified electrowetting equation involving applied electrical potential. In the figure, each single dot represents the result of experiment values, while each dashed line shows data that was calculated based on the MNS's modified electrowetting equation. The experimental result of Ψ for the 0 nm (no pore) sample fits well into Young–Lippmann's electrowetting model, while the experimental

results for the other samples match the modified electrowetting equation for MNS. This indicates that the modified electrowetting equation, which considered the pore structure of a given MNS, can properly identify a MNS's electrowettability behavior.

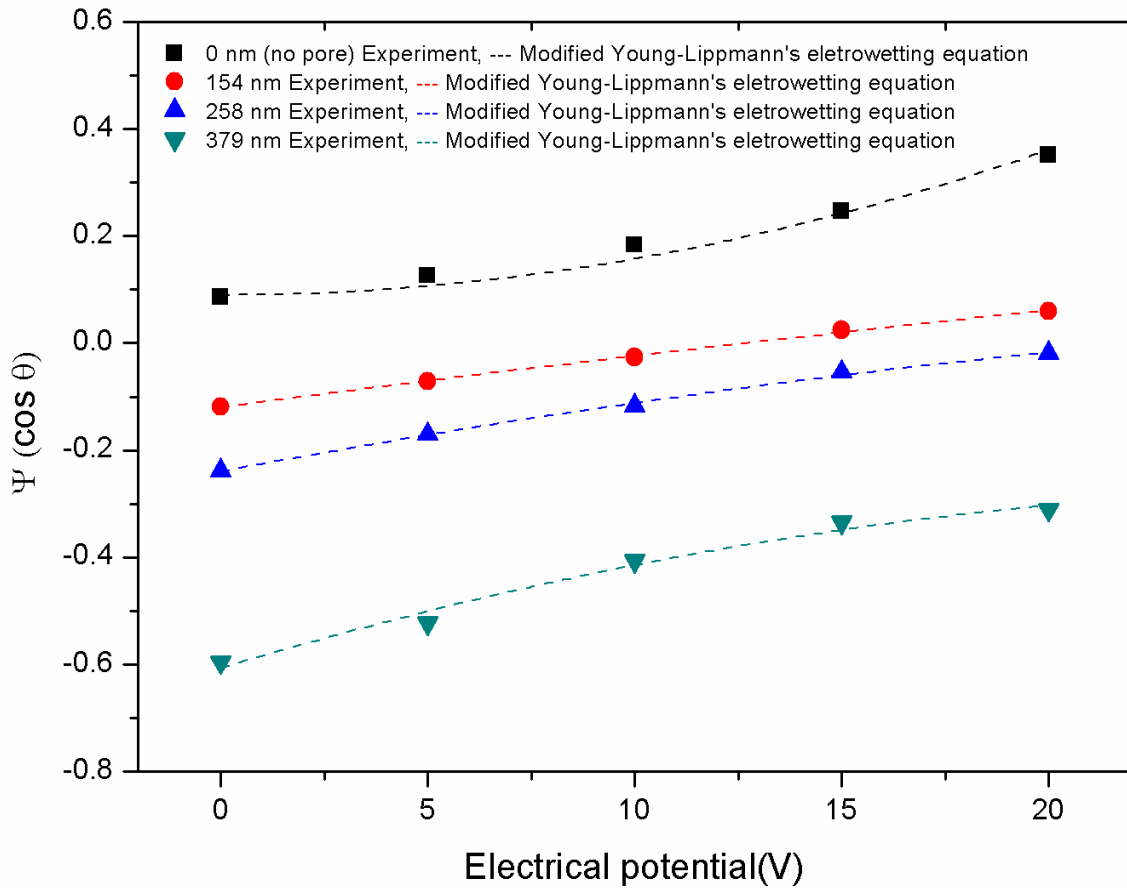


Figure 7.7. $\Psi (\cos \theta)$ using contact angle of water droplet on the MNS as a function of the applied electrical potential. Each solid dot represents the results from experiments and each dash line demonstrates the calculated results by using modified electrowetting equation for MNS.

As stated above, the intrinsic contact angle and the electrowetting behavior are altered by the pore formed on the MNS's surface. The results show that the specific electrowetting behavior of any given MNS is affected by its pore size. In order to verify

the contact angle alteration with externally applied electrical potential, the specifics of the wetting mechanism on the interface between the water droplet and the MNS should be determined. The flat surface (no pore) and MNS demonstrate different wettability mechanisms at the interface. Figure 7.8 shows a schematic electrowetting mechanism on both a flat surface and a MNS. In the case of the flat surface, a water droplet can fully cover the top flat surface without any air gap between the water droplet and the surface. With externally applied electrical potential, the water droplet can be spread across the electrically-charged flat surface as in Figure 7.8.a¹⁸⁹. In contrast, an air gap exists between the surface of a MNS and a water droplet. Due to this air gap, the water droplet can be absorbed into the pore by applying an electrical potential. As shown in Figure 7.8.b, the electrically-charged nickel-coated MNS structure can drag the water droplet into the pore under applied electrical potential. Buijnsters et al. explained that the wetting behavior of water droplets on porous structures was affected by compressed air in the pore¹⁷⁸. The compressed air can prevent the water droplet's full absorption into the pore structure. The pore diameter of a MNS mainly affects the volume of air compression and it determines the depth of water droplet penetration (h)^{183, 190}. A schematic diagram of the electrowetting balance model is proposed in Figure 7.8.c based on the results obtained for MNSs.

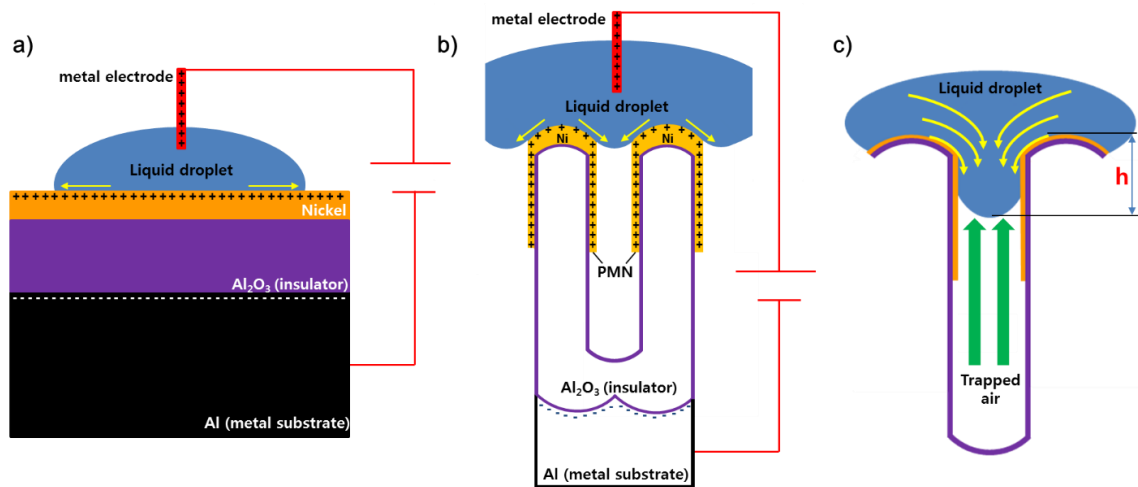


Figure 7.8. Schematic expression the electrowetting mechanism of MNS. a) electrowetting experiment on flat (no pore) surface, b) electrowetting experiment on MNS surface, and c) the electrowetting balance model at the pore.

When the electrical potential was applied between the water droplet on the MNS and the aluminum substrate, the water droplet was able to be absorbed into the pore. Increases in the electrical potential can result in increased absorption of a water droplet into the pore. However, due to the presence of trapped air, the water droplet cannot be fully absorbed into the pore. The trapped air acts as a basis of resistance to absorption to repel the water droplet. These absorbing and repelling forces reach a balance to maintain a state of equilibrium. Once the repelling force is the same as the absorbing force, the water droplet will no longer be absorbed into the pore. It is possible to calculate the balanced value of ' h ' by using equations (7.9) and (7.13). Figure 7.9 shows the ' h ' alteration with applying electrical potential on the PMNs. As the figure shows, the value of ' h ' increased with increasing the application of electrical potential.

This study found that the contact angle saturation progressively decreased as externally applied electrical potential increased. This behavior is based on the equilibrium mode. According to the electrowetting results, the length of the absorbing liquid droplet on the MNS can be manipulated by controlling the pore size, pore depth, and the electrical potential. By using the MNS as a template, it may be feasible to fabricate nanopillar structures having various pillar lengths by applying electrical potential.

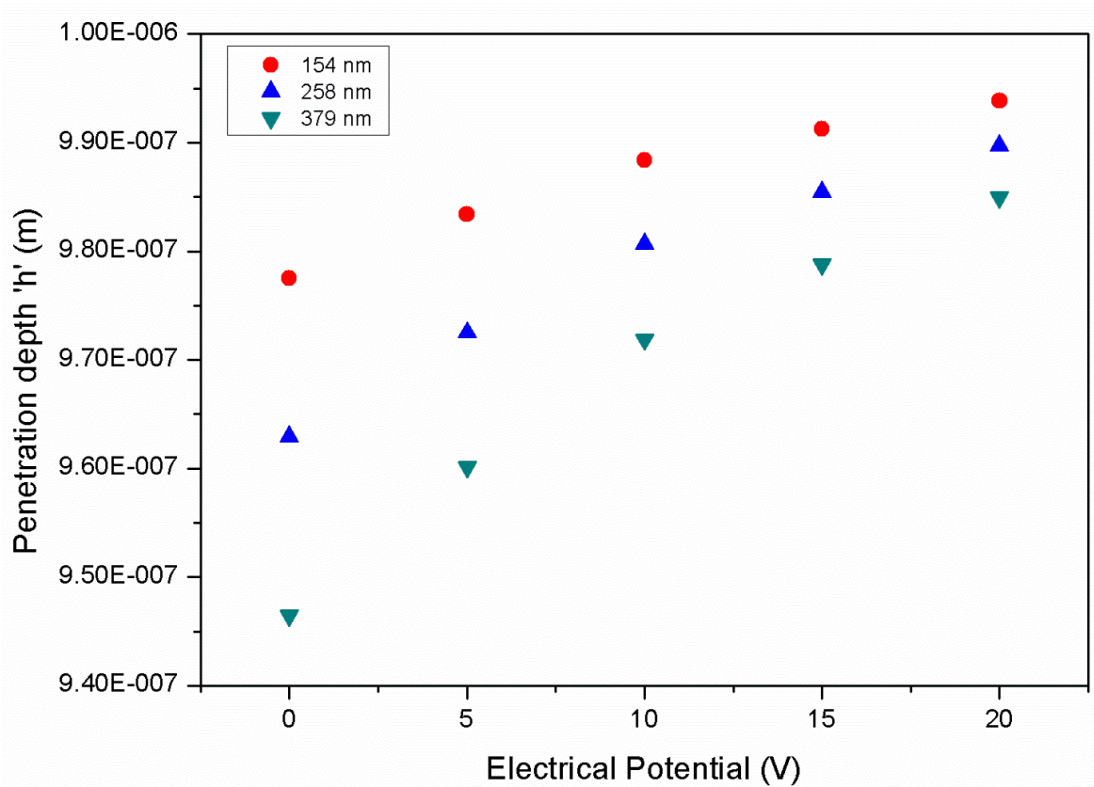


Figure 7.9. The depth of water droplet penetration with applying electrical potential for various pore size of MNS.

Not only was the contact angle altered, but the contact diameter between the water droplet and the surface also changed when an electrical potential was applied to the MNS. Figure 7.10 plots the contact diameter against the applied electrical potential. In contrast with the contact angle behavior, the contact diameter increased in all substrates as an increased electrical potential was applied. As a general rule, when the contact angle decreases, the contact diameter increases. The contact diameter behavior of MNSs also follows this general trend. As shown in Figure 7.10, the contact diameter decreased with increasing pore diameters, while the contact angle increased with increasing pore diameters. The behavior of contact diameter against the electrical potential shows saturation with increasing pore size. A remarkable feature of the electrowetting of the MNS is that the water droplet does not spread much across the surface. The smaller the pore size of the MNS, the more widely a water droplet spreads: the 0nm (no pore), 154 nm, 258 nm, and 379 nm pore sizes demonstrated increasing contact diameters of 22.03%, 14.19%, 9.18% and 7.22% on MNS respectively.

This signifies that a water droplet on a MNS is mostly absorbed into the pore when electrical potential is applied. Moreover, the capillary force of the pore can prevent the water droplet from spreading across the MNS's surface, as indicated by the 'rose petal effect'^{190, 191}. Thus, it is possible to retain hydrophobic properties of a MNS's surface by applying electrical potential for electrowetting.

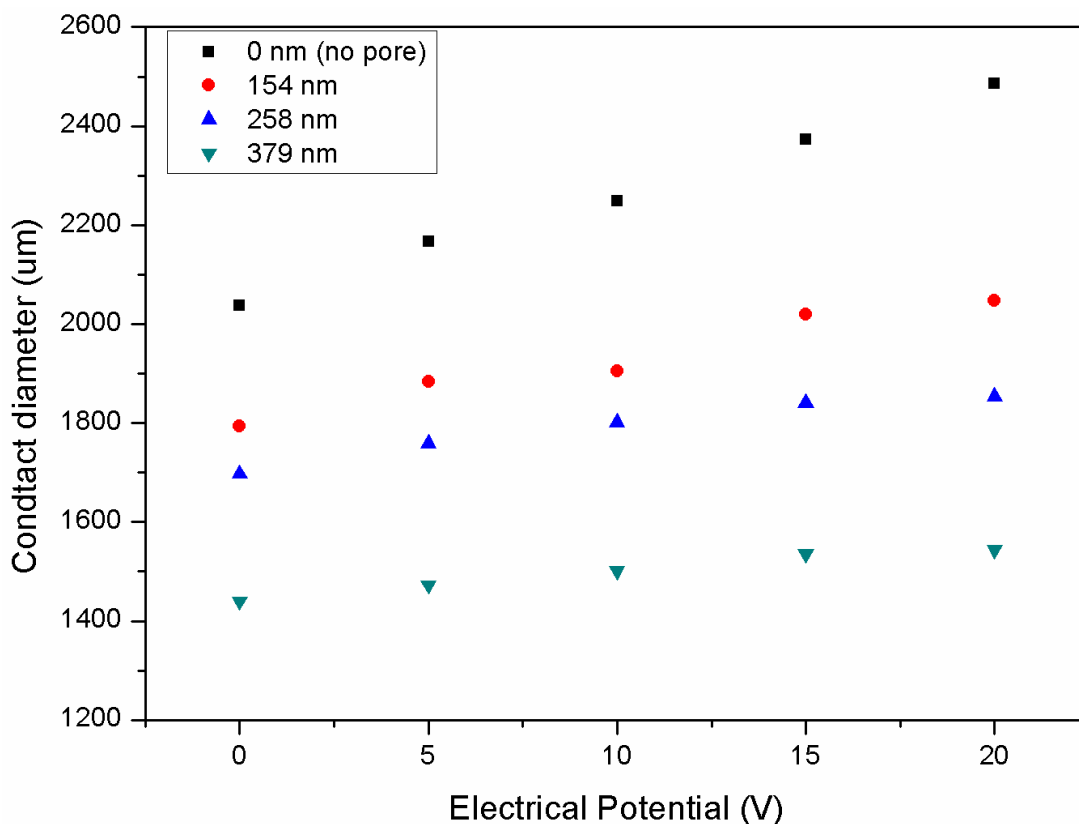


Figure 7.10. The plot of contact diameter against the applied electrical potential with various pore size.

This result contradicts the general electrowetting effect in which wettability is manipulated from the Cassie-Baxter model to the Wenzel model when an electrical potential is applied between a liquid droplet and a substrate. Further research is needed for more in-depth analysis of this behavior to identify critical factors for manipulating the electrowettability of MNS structures.

7.4. Summary

In this chapter, the wetting dynamics of an initial droplet on a MNS were firstly examined to determine the intrinsic contact angle. The wetting model was established to

simulate intrinsic contact angle on a MNS. Subsequently, electrowetting studies were conducted by analyzing the behavior of the contact angle and the contact diameter. By measuring the contact angle on a MNS while applying an electrical potential, it was possible to see how the electrical potential affects the surface wettability. This study sought to determine the wettability and electrowettability mechanism of MNSs, using a droplet shape measurement system to evaluate the contact angle.

Wettability/electrowettability were primarily characterized by contact angle. It was found that both the wettability/electrowettability of MNS depended on its pore size. The energy balance among water droplet, surface, and air was altered by pore size of MNS. It provides that the shape of pore can manipulate the contact phenomena for determining wettability/electrowettability. This study offers a guide to the functional wetting/electrowetting behavior of MNSs with various pore sizes.

CHAPTER VIII

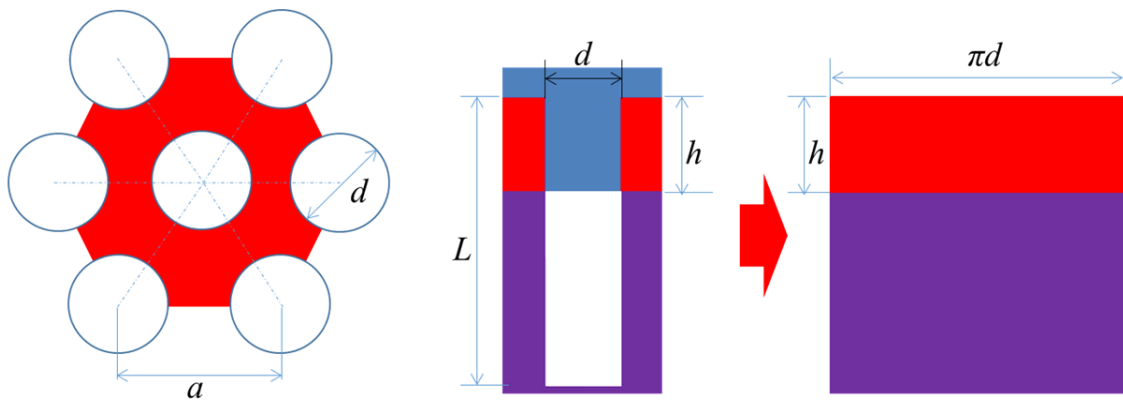
CONCLUSIONS AND FUTURE WORKS

8.1. Conclusions

This research investigated the properties of textured surfaces through experimental and theoretical analysis approaches. In order to understand the physical interactions between environmental entities and the textured surfaces, metallic and oxidic nanopores structured were focused. Metallic nanopore structures (MNSs) were studied to examine the effect of electrical potential on surface forces, electrochemical performances, and wettability/electrowettability. Alumina nanostructures (ANSs) were studied to explore the interfacial interaction between bacteria and a nanoporous surface. Effects of applied electrical potential on surface morphology and tribological performance of MNSs were performed using an AFM. Indentation modulus of MNSs were also investigated by a Triboscope with applied electrical potentials. The mechanisms of adhesion of *E. coli* cells on ANSs were examined using a bacteria repelling experiment method. Electrochemical Impedance Spectroscopy (EIS) and Cyclic Voltametry (CV) experiments of MNSs were conducted using an electro potential stat in 1M KOH as an electrolyte. The wettability/electrowettability of MNSs with various pore sizes were investigated using a liquid droplet shape measurement system. The wetting model was contrived to simulate the wettability of MNS in terms of contact angle.

Research results indicated that surface properties, including surface forces,

electrochemical performances, and wettability/electrowettability, depended on the nature of contact. A universal contact model is proposed in order to understand and predict the behavior of a textured surface. Specifically, the contact between the environment (air, liquid, and (quasi-) solid) and a textured surface can be classified into three characteristic modes. These modes depend on a geometrical parameter, i.e., the breadth (h), at the interface. When the value of h is equal to zero, contact occurs only on the top surface, and no contact in the pore. If the contact involves full contact with the pore, the value of h is same as the pore depth (L). The value of h will exist between zero and L if the contact involves partial contact with the pore. All these classifications represent ways of determining contact modes: mode I stands for contact via $h=0$; mode II stands for contact via $h=L$; and mode III stands for contact via $0<h<L$. Figure 8.1 illustrates each mode of contact with nanopore structures.



Mode I → contact on top surface, $h=0$

Mode II → contact on top surface & full contact in pore, $h=L$

Mode III → contact on top surface & partial contact in pore, $0<h<L$

Figure 8.1. Various contact modes in nanopore structures.

The above model can be applied to the designated conditions and applications discussed in the thesis: The contact area for mode I with surface force dominate; effective surface area (ESA) for mode II with desirable electrochemical performance; and areas of liquid-solid and liquid-vapor interface for mode III with wettability. Surface forces decreased with decreasing the contact area in case of mode I. Increase of the ESA enhanced electrochemical performances under mode II. The wettability/eletrowettability were controlled by areas of each interface as mode III. All contact modes are controlled by the pore size of the nanopore structure. The upshot is that the requisite geometrical factor can be represented by contact phenomena in terms of contact mode, and the crucial design factor for all contact modes is the feature size of nanopore structures.

The discovery of the parameter h is applicable to other textured surfaces. Despite the materials and types of surface textures, the contact area and/or geometry is a critical factor. The value of h can provide proper approaching way to analyze the properties of textured surface via each contact mode. Once the contact mode is decided, each surface properties can be identified by proposed design factors: contact area, ESA, and areas of each interface.

The findings in this study can provide an understanding of the characterization of surface properties and support the conceptual design of nanopore structures for particular applications. The requisite geometrical factors and specific design factors can be used for optimization of surface properties for specific applications. Having an understanding of the interrelationship of nanostructures/surface properties/device performance will enhance future design and optimization of new devices.

8.2. Future works

Based on the findings of this research, the following future tasks are recommended:

- 1) Use other materials-based nanopore structures: This research focused two specific types of nanopore structures: nickel-based metallic nanopore structures and alumina-based oxidic nanopore structures. This study found that surface properties are mainly affected by surface morphology (i.e., shape and topography). In order to confirm this effect in a wider range of materials, surface properties in other types of materials should be investigated.
- 2) Investigate other surface properties: This research considered three major surface properties: surface force, electrochemical performance, and wettability/electrowettability. Other surface-related properties include plasmonic properties, photonic properties, and surface fluidics such as the coffee ring effect. Exploring other surface properties would be helpful for extending the scope of this study.
- 3) Establish a simulation model for analyzing surface properties: A wetting model of a nanopore structure for numerical analysis was demonstrated in this study. Establishing simulation models for surface forces, electrochemical performances, and electrowettability will be beneficial for anticipating the behavior of surface properties with respect to their applications.

REFERENCES

1. Yu, J. et al. Nanoporous metals by dealloying multicomponent metallic glasses. *Chemistry of Materials* 20, 4548-4550 (2008).
2. Wang, L., Imura, M. & Yamauchi, Y. Tailored synthesis of various Au nanoarchitectures with branched shapes. *CrystEngComm* 14, 7594-7599 (2012).
3. Liddicoat, P.V. et al. Nanostructural hierarchy increases the strength of aluminium alloys. *Nature communications* 1, 63 (2010).
4. Mulero, R., Prabhu, A.S., Freedman, K.J. & Kim, M.J. Nanopore-Based Devices for Bioanalytical Applications. *Journal of the Association for Laboratory Automation* 15, 243-252 (2010).
5. Kim, M.J., Wanunu, M., Bell, D.C. & Meller, A. Rapid Fabrication of Uniformly Sized Nanopores and Nanopore Arrays for Parallel DNA Analysis. *Advanced Materials* 18, 3149-3153 (2006).
6. Hajiaboli, A.R., Cui, B., Kahrizi, M. & Truong, V.-V. Optical properties of thick metal nanohole arrays fabricated by electron-beam and nanosphere lithography. *physica status solidi (a)* 206, 976-979 (2009).
7. Chen, J. et al. Gold nanohole arrays for biochemical sensing fabricated by soft UV nanoimprint lithography. *Microelectronic Engineering* 86, 632-635 (2009).
8. Gleiter, H. Nanostructured materials: basic concepts and microstructure. *Acta Materialia* 48, 1-29 (2000).
9. Gleiter, H. Nanostructured materials: state of the art and perspectives. *Nanostructured Materials* 6, 3-14 (1995).
10. Wilde, G. *Nanostructured Materials*. (Elsevier, Amsterdam; 2009).
11. Hwang, H.-D. et al. Effect of water drying conditions on the surface property and morphology of waterborne UV-curable coatings for engineered flooring. *Journal of Industrial and Engineering Chemistry* 15, 381-387 (2009).
12. Khorasani, M., Mirzadeh, H. & Kermani, Z. Wettability of porous polydimethylsiloxane surface: morphology study. *Applied Surface Science* 242, 339-345 (2005).
13. Park, M.S., Kang, Y.M., Wang, G.X., Dou, S.X. & Liu, H.K. The effect of morphological modification on the electrochemical properties of SnO₂ nanomaterials. *Advanced Functional Materials* 18, 455-461 (2008).

14. Patterson, N. et al. Controlled fabrication of nanopores using a direct focused ion beam approach with back face particle detection. *Nanotechnology* 19, 235304 (2008).
15. Penmatsa, V., Kawarada, H. & Wang, C. Fabrication of carbon nanostructures using photo-nanoimprint lithography and pyrolysis. *Journal of Micromechanics and Microengineering* 22, 045024 (2012).
16. Schiff, H. et al. Fabrication of polymer photonic crystals using nanoimprint lithography. *Nanotechnology* 16, S261-S265 (2005).
17. Wu, M.-Y., Krapf, D., Zandbergen, M., Zandbergen, H. & Batson, P.E. Formation of nanopores in a SiN/SiO₂ membrane with an electron beam. *Applied Physics Letters* 87, 113106 (2005).
18. Lo, C.J., Aref, T. & Bezryadin, A. Fabrication of symmetric sub-5 nm nanopores using focused ion and electron beams. *Nanotechnology* 17, 3264-3267 (2006).
19. Schiff, H., Bellini, S., Pielele, U. & Gobrecht, J. Sustained polymer membranes fabricated by nanoimprint lithography. *Journal of Micro/Nanolithography, MEMS, and MOEMS* 5, 011010-011010-011015 (2006).
20. Zheng, H. et al. Electron beam-assisted healing of nanopores in magnesium alloys. *Scientific reports* 3 (2013).
21. Woldering, L.A., Otter, A.B., Husken, B.H. & Vos, W.L. Focused ion beam milling of nanocavities in single colloidal particles and self-assembled opals. *Nanotechnology* 17, 5717 (2006).
22. Hwang, S.-K., Jeong, S.-H., Hwang, H.-Y., Lee, O.-J. & Lee, K.-H. Fabrication of highly ordered pore array in anodic aluminum oxide. *Korean Journal of Chemical Engineering* 19, 467-473 (2002).
23. Masuda, H. & Fukuda, K. Ordered Metal Nanohole Arrays Made by a Two-Step Replication of Honeycomb Structures of Anodic Alumina. *Science* 268, 1466-1468 (1995).
24. Choi, H.-G. et al. Fabrication of Nanopattern by Nanoimprint Lithography for the Application to Protein Chip. *Biochip Journal* 3, 76 (2009).
25. Vix-Guterl, C. et al. Electrochemical energy storage in ordered porous carbon materials. *Carbon* 43, 1293-1302 (2005).
26. Albrecht, T. Nanobiotechnology: A new look for nanopore sensing. *Nature nanotechnology* 6, 195-196 (2011).

27. Whitney, A.V., Myers, B.D. & Van Duyne, R.P. Sub-100 nm Triangular Nanopores Fabricated with the Reactive Ion Etching Variant of Nanosphere Lithography and Angle-Resolved Nanosphere Lithography. *Nano Letters* 4, 1507-1511 (2004).
28. Förch, R. in *Surface Design: Applications in Bioscience and Nanotechnology* 55-80 (Wiley-VCH Verlag GmbH & Co. KGaA, 2009).
29. Popat, K.C. et al. Influence of nanoporous alumina membranes on long-term osteoblast response. *Biomaterials* 26, 4516-4522 (2005).
30. Ferraz, N., Carlsson, J., Hong, J. & Ott, M.K. Influence of nanoporesize on platelet adhesion and activation. *Journal of Materials Science: Materials in Medicine* 19, 3115-3121 (2008).
31. Holmberg, K. Reliability aspects of tribology. *Tribology International* 34, 801-808 (2001).
32. Bhushan, B. Micro/nanotribology and its applications to magnetic storage devices and MEMS. *Tribology International* 28, 85-96 (1995).
33. Liu, H. & Bhushan, B. Nanotribological characterization of molecularly thick lubricant films for applications to MEMS/NEMS by AFM. *Ultramicroscopy* 97, 321-340 (2003).
34. Xie, G., Ding, J., Liu, S., Xue, W. & Luo, J. Interfacial properties for real rough MEMS/NEMS surfaces by incorporating the electrostatic and Casimir effects-a theoretical study. *Surface and Interface Analysis* 41, 338-346 (2009).
35. Tsukruk, V.V. & Bliznyuk, V.N. Adhesive and Friction Forces between Chemically Modified Silicon and Silicon Nitride Surfaces. *Langmuir* 14, 446-455 (1998).
36. Hochbaum, A.I. & Aizenberg, J. Bacteria pattern spontaneously on periodic nanostructure arrays. *Nano letters* 10, 3717-3721 (2010).
37. Epstein, A., Hochbaum, A., Kim, P. & Aizenberg, J. Control of bacterial biofilm growth on surfaces by nanostructural mechanics and geometry. *Nanotechnology* 22, 494007 (2011).
38. Edwards, K.J. & Rutenberg, A.D. Microbial response to surface microtopography: the role of metabolism in localized mineral dissolution. *Chemical Geology* 180, 19-32 (2001).

39. Mokrushina, A.V., Heim, M., Karyakina, E.E., Kuhn, A. & Karyakin, A.A. Enhanced hydrogen peroxide sensing based on Prussian Blue modified macroporous microelectrodes. *Electrochemistry Communications* 29, 78-80 (2013).
40. Palm, R., Kurig, H., Tõnurist, K., Jänes, A. & Lust, E. Electrical double layer capacitors based on 1-ethyl-3-methylimidazolium tetrafluoroborate with small addition of acetonitrile. *Electrochimica Acta* 85, 139-144 (2012).
41. Guo, P., Song, H. & Chen, X. Electrochemical performance of graphene nanosheets as anode material for lithium-ion batteries. *Electrochemistry Communications* 11, 1320-1324 (2009).
42. Liu, H., Zhai, J. & Jiang, L. Wetting and anti-wetting on aligned carbon nanotube films. *Soft Matter* 2, 811-821 (2006).
43. Lai, Y. et al. Designing Superhydrophobic Porous Nanostructures with Tunable Water Adhesion. *Advanced Materials* 21, 3799-3803 (2009).
44. Ressine, A., Ekström, S., Marko-Varga, G. & Laurell, T. Macro-/nanoporous silicon as a support for high-performance protein microarrays. *Analytical chemistry* 75, 6968-6974 (2003).
45. Chow, T.S. Wetting of rough surfaces. *J. Phys.: Condens. Matter* 10, 445 (1998).
46. Hertz, H. in *Journal für die reine und angewandte Mathematik (Crelle's Journal)*, Vol. 1882 156 (1882).
47. Johnson, K.L., Kendall, K. & Roberts, A.D. Surface Energy and the Contact of Elastic Solids. *Proceedings of the Royal Society A: Mathematical, Physical and Engineering Sciences* 324, 301-313 (1971).
48. Derjaguin, B.V., Muller, V.M. & Toporov, Y.P. Effect of contact deformations on the adhesion of particles. *Journal of Colloid and Interface Science* 53, 314-326 (1975).
49. Young, T. An Essay on the Cohesion of Fluids. *Philosophical Transactions of the Royal Society of London* 95, 65-87 (1805).
50. Cassie, A.B.D. & Baxter, S. Wettability of porous surfaces. *Transactions of the Faraday Society* 40, 546-551 (1944).
51. Wenzel, R.N. Surface Roughness and Contact Angle. *The Journal of Physical and Colloid Chemistry* 53, 1466-1467 (1949).

52. Cottrell, F.G. Der Reststrom bei galvanischer Polarisation, betrachtet als ein Diffusionsproblem. *Z. Phys. Chem.* 42, 385 (1903).
53. Randles, J.E.B. A cathode ray polarograph. Part II.-The current-voltage curves. *Transactions of the Faraday Society* 44, 327-338 (1948).
54. Howlett, P.C., MacFarlane, D.R. & Hollenkamp, A.F. High Lithium Metal Cycling Efficiency in a Room-Temperature Ionic Liquid. *Electrochemical and Solid-State Letters* 7, A97 (2004).
55. Beitollahi, H., Raof, J.-B. & Hosseinzadeh, R. Fabrication of a nanostructure-based electrochemical sensor for simultaneous determination of N-acetylcysteine and acetaminophen. *Talanta* 85, 2128-2134 (2011).
56. Mazloum-Ardakani, M., Beitollahi, H., Amini, M.K., Mirkhalaf, F. & Mirjalili, B.-F. A highly sensitive nanostructure-based electrochemical sensor for electrocatalytic determination of norepinephrine in the presence of acetaminophen and tryptophan. *Biosensors and Bioelectronics* 26, 2102-2106 (2011).
57. Banerjee, S. et al. Electrochemistry at the Edge of a Single Graphene Layer in a Nanopore. *ACS Nano* 7, 834-843 (2012).
58. Zhou, Y. et al. Fluid-shear method to evaluate bacterial adhesion to glass surfaces. *Journal of Applied Physics* 112, 014703 (2012).
59. Rocha, A., Hahn, M. & Liang, H. Critical fluid shear stress analysis for cell-polymer adhesion. *J Mater Sci* 45, 811-817 (2010).
60. Choi, D., Hwang, W. & Yoon, E. Improved lateral force calibration based on the angle conversion factor in atomic force microscopy. *Journal of microscopy* 228, 190-199 (2007).
61. Oliver, W.C. & Pharr, G.M. An improved technique for determining hardness and elastic modulus using load and displacement sensing indentation experiments. *Journal of materials research* 7, 1564-1583 (1992).
62. King, R.B. Elastic analysis of some punch problems for a layered medium. *International Journal of Solids and Structures* 23, 1657-1664 (1987).
63. Ahn, J.-H., Jeon, E.-c., Choi, Y., Lee, Y.-H. & Kwon, D. Derivation of tensile flow properties of thin films using nanoindentation technique. *Current applied physics* 2, 525-531 (2002).

64. Yan, J., Karlsson, A.M. & Chen, X. Determining plastic properties of a material with residual stress by using conical indentation. *International journal of solids and structures* 44, 3720-3737 (2007).
65. Hay, J.C., Bolshakov, A. & Pharr, G. A critical examination of the fundamental relations used in the analysis of nanoindentation data. *Journal of Materials Research* 14, 2296-2305 (1999).
66. Johnson, K.L. *Contact mechanics*. (Cambridge university press, 1987).
67. Flemming, H.C. Biofouling in water systems – cases, causes and countermeasures. *Appl Microbiol Biotechnol* 59, 629-640 (2002).
68. Shi, X. & Zhu, X. Biofilm formation and food safety in food industries. *Trends in Food Science & Technology* 20, 407-413 (2009).
69. Flemmig, T.F. & Beikler, T. Control of oral biofilms. *Periodontology* 2000 55, 9-15 (2011).
70. Zimmerli, W., Trampuz, A. & Ochsner, P.E. Prosthetic-Joint Infections. *New England Journal of Medicine* 351, 1645-1654 (2004).
71. Lentino, J.R. Prosthetic Joint Infections: Bane of Orthopedists, Challenge for Infectious Disease Specialists. *Clinical Infectious Diseases* 36, 1157-1161 (2003).
72. Kurtz, S.M. et al. Infection burden for hip and knee arthroplasty in the United States. *The Journal of arthroplasty* 23, 984-991 (2008).
73. Targarona, E.M., Balagué, C., Knook, M.M. & Trías, M. Laparoscopic surgery and surgical infection. *British Journal of Surgery* 87, 536-544 (2000).
74. Ironside, J.W. et al. Variant Creutzfeldt-Jakob disease: prion protein genotype analysis of positive appendix tissue samples from a retrospective prevalence study. *Bmj* 332, 1186-1188 (2006).
75. Keith R Milner, C.A.S. Fibroblast response is enhanced by poly(L-lactic acid) nanotopography edge density and proximity. *Int J Nanomedicine* 2, 201-211 (2007).
76. Milner, K.R., Snyder, A.J. & Siedlecki, C.A. Sub-micron texturing for reducing platelet adhesion to polyurethane biomaterials. *Journal of Biomedical Materials Research Part A* 76A, 561-570 (2006).

77. Epstein, A.K., Hochbaum, A.I., Kim, P. & Aizenberg, J. Control of bacterial biofilm growth on surfaces by nanostructural mechanics and geometry. *Nanotechnology* 22, 494007 (2011).
78. Jiang, X. et al. Bacterial Adhesion on Honeycomb-Structured Poly(L-Lactic Acid) Surface with Ag Nanoparticles. *Journal of Biomedical Nanotechnology* 8, 791-799 (2012).
79. Xu, L.-C. & Siedlecki, C.A. Submicron-textured biomaterial surface reduces staphylococcal bacterial adhesion and biofilm formation. *Acta Biomaterialia* 8, 72-81 (2012).
80. Koh, L.B., Rodriguez, I. & Venkatraman, S.S. The effect of topography of polymer surfaces on platelet adhesion. *Biomaterials* 31, 1533-1545 (2010).
81. Bond, A.M. & Feldberg, S.W. Analysis of simulated reversible cyclic voltammetric responses for a charged redox species in the absence of added electrolyte. *The Journal of Physical Chemistry B* 102, 9966-9974 (1998).
82. Nicholson, R.S. Theory and Application of Cyclic Voltammetry for Measurement of Electrode Reaction Kinetics. *Analytical Chemistry* 37, 1351-1355 (1965).
83. Carriedo, G.A. The use of cyclic voltammetry in the study of the chemistry of metal-carbonyls: An introductory experiment. *Journal of Chemical Education* 65, 1020 (1988).
84. McEwen, A.B., Ngo, H.L., LeCompte, K. & Goldman, J.L. Electrochemical Properties of Imidazolium Salt Electrolytes for Electrochemical Capacitor Applications. *Journal of The Electrochemical Society* 146, 1687-1695 (1999).
85. MacFarlane, D.R., Meakin, P., Sun, J., Amini, N. & Forsyth, M. Pyrrolidinium Imides: A New Family of Molten Salts and Conductive Plastic Crystal Phases. *The Journal of Physical Chemistry B* 103, 4164-4170 (1999).
86. Wang, Q., Moser, J.-E. & Grätzel, M. Electrochemical Impedance Spectroscopic Analysis of Dye-Sensitized Solar Cells. *The Journal of Physical Chemistry B* 109, 14945-14953 (2005).
87. Song, H.-K., Jung, Y.-H., Lee, K.-H. & Dao, L.H. Electrochemical impedance spectroscopy of porous electrodes: the effect of pore size distribution. *Electrochimica Acta* 44, 3513-3519 (1999).
88. Chamas, M. et al. Electrochemical impedance characterization of FeSn₂ electrodes for Li-ion batteries. *Electrochimica Acta* 56, 6732-6736 (2011).

89. Mokrushina, A.V., Heim, M., Karyakina, E.E., Kuhn, A. & Karyakin, A.A. Enhanced hydrogen peroxide sensing based on Prussian Blue modified macroporous microelectrodes. *Electrochemistry Communications* 29, 78-80 (2013).
90. Siinor, L., Siimenson, C., Lust, K. & Lust, E. Mixture of 1-ethyl-3-methylimidazolium tetrafluoroborate and 1-ethyl-3-methylimidazolium iodide: A new potential high capacitance electrolyte for EDLCs. *Electrochemistry Communications* 35, 5-7 (2013).
91. Palm, R., Kurig, H., Tõnurist, K., Jänes, A. & Lust, E. Electrical double layer capacitors based on 1-ethyl-3-methylimidazolium tetrafluoroborate with small addition of acetonitrile. *Electrochimica Acta* 85, 139-144 (2012).
92. Abe, T., Fukuda, H., Iriyama, Y. & Ogumi, Z. Solvated Li-ion transfer at interface between graphite and electrolyte. *Journal of The Electrochemical Society* 151, A1120-A1123 (2004).
93. Taberna, P.-L., Mitra, S., Poizot, P., Simon, P. & Tarascon, J.-M. High rate capabilities Fe₃O₄-based Cu nano-architected electrodes for lithium-ion battery applications. *Nature materials* 5, 567-573 (2006).
94. Yamada, Y., Iriyama, Y., Abe, T. & Ogumi, Z. Kinetics of lithium ion transfer at the interface between graphite and liquid electrolytes: effects of solvent and surface film. *Langmuir* 25, 12766-12770 (2009).
95. Opallo, M. & Lesniewski, A. A review on electrodes modified with ionic liquids. *Journal of Electroanalytical Chemistry* 656, 2-16 (2011).
96. Pan, G., Xia, X., Cao, F., Tang, P. & Chen, H. Fabrication of porous Co/NiO core/shell nanowire arrays for electrochemical capacitor application. *Electrochemistry Communications* 34, 146-149 (2013).
97. Hasan, M., Jamal, M. & Razeeb, K.M. Coaxial NiO/Ni nanowire arrays for high performance pseudocapacitor applications. *Electrochimica Acta* 60, 193-200 (2012).
98. Kim, K.-S. & Park, S.-J. Synthesis and electrochemical performance of well-balanced mesopore/micropore contained carbons by activation-free method. *Electrochemistry Communications* 22, 89-92 (2012).
99. Shen, L. et al. In situ growth of Li₄Ti₅O₁₂ on multi-walled carbon nanotubes: novel coaxial nanocables for high rate lithium ion batteries. *Journal of Materials Chemistry* 21, 761-767 (2011).

100. Lanyon, Y.H. et al. Fabrication of nanopore array electrodes by focused ion beam milling. *Analytical chemistry* 79, 3048-3055 (2007).
101. Kondrat, S., Kornyshev, A., Stoeckli, F. & Centeno, T. The effect of dielectric permittivity on the capacitance of nanoporous electrodes. *Electrochemistry Communications* 34, 348-350 (2013).
102. Bian, X. et al. Nanocomposite of MoS₂ on ordered mesoporous carbon nanospheres: A highly active catalyst for electrochemical hydrogen evolution. *Electrochemistry Communications* 22, 128-132 (2012).
103. Frackowiak, E. Carbon materials for supercapacitor application. *Physical Chemistry Chemical Physics* 9, 1774-1785 (2007).
104. Lee, S.W., Gallant, B.M., Byon, H.R., Hammond, P.T. & Shao-Horn, Y. Nanostructured carbon-based electrodes: bridging the gap between thin-film lithium-ion batteries and electrochemical capacitors. *Energy & Environmental Science* 4, 1972-1985 (2011).
105. Nishihara, H. et al. Investigation of the Ion Storage/Transfer Behavior in an Electrical Double-Layer Capacitor by Using Ordered Microporous Carbons as Model Materials. *Chemistry-A European Journal* 15, 5355-5363 (2009).
106. Xu, F. et al. Fast ion transport and high capacitance of polystyrene-based hierarchical porous carbon electrode material for supercapacitors. *Journal of Materials Chemistry* 21, 1970-1976 (2011).
107. Jia, F., Yu, C., Ai, Z. & Zhang, L. Fabrication of nanoporous gold film electrodes with ultrahigh surface area and electrochemical activity. *Chemistry of Materials* 19, 3648-3653 (2007).
108. Jia, F., Yu, C., Deng, K. & Zhang, L. Nanoporous metal (Cu, Ag, Au) films with high surface area: general fabrication and preliminary electrochemical performance. *The Journal of Physical Chemistry C* 111, 8424-8431 (2007).
109. Zhang, J., Liu, P., Ma, H. & Ding, Y. Nanostructured porous gold for methanol electro-oxidation. *The Journal of Physical Chemistry C* 111, 10382-10388 (2007).
110. Squires, T.M. & Quake, S.R. Microfluidics: Fluid physics at the nanoliter scale. *Reviews of modern physics* 77, 977 (2005).
111. Fürstner, R., Barthlott, W., Neinhuis, C. & Walzel, P. Wetting and self-cleaning properties of artificial superhydrophobic surfaces. *Langmuir* 21, 956-961 (2005).

112. Rossi, A.M., Wang, L., Reipa, V. & Murphy, T.E. Porous silicon biosensor for detection of viruses. *Biosensors and Bioelectronics* 23, 741-745 (2007).
113. Bao, S., TANG, K., Kvithyld, A., Engh, T. & Tangstad, M. Wetting of pure aluminium on graphite, SiC and Al₂O₃ in aluminium filtration. *Transactions of Nonferrous Metals Society of China* 22, 1930-1938 (2012).
114. Cao, L., Jones, A.K., Sikka, V.K., Wu, J. & Gao, D. Anti-icing superhydrophobic coatings. *Langmuir* 25, 12444-12448 (2009).
115. Cao, L., Price, T.P., Weiss, M. & Gao, D. Super water-and oil-repellent surfaces on intrinsically hydrophilic and oleophilic porous silicon films. *Langmuir* 24, 1640-1643 (2008).
116. Haeberle, S. & Zengerle, R. Microfluidic platforms for lab-on-a-chip applications. *Lab on a Chip* 7, 1094-1110 (2007).
117. Nguyen, D.D., Tai, N.-H., Lee, S.-B. & Kuo, W.-S. Superhydrophobic and superoleophilic properties of graphene-based sponges fabricated using a facile dip coating method. *Energy & Environmental Science* 5, 7908-7912 (2012).
118. Lai, Y. et al. Transparent superhydrophobic/superhydrophilic TiO₂-based coatings for self-cleaning and anti-fogging. *Journal of Materials Chemistry* 22, 7420-7426 (2012).
119. Zhang, F. & Low, H.Y. Anisotropic wettability on imprinted hierarchical structures. *Langmuir* 23, 7793-7798 (2007).
120. Choi, J.H. et al. Hydrophilic dots on hydrophobic nanopatterned surfaces as a flexible gas barrier. *Langmuir* 25, 7156-7160 (2009).
121. Blossey, R. Self-cleaning surfaces [mdash] virtual realities. *Nat Mater* 2, 301-306 (2003).
122. Fujii, T., Sato, H., Tsuji, E., Aoki, Y. & Habazaki, H. Important Role of Nanopore Morphology in Superoleophobic Hierarchical Surfaces. *The Journal of Physical Chemistry C* 116, 23308-23314 (2012).
123. Cassie, A. & Baxter, S. Wettability of porous surfaces. *Transactions of the Faraday Society* 40, 546-551 (1944).
124. Mugele, F. & Baret, J.-C. Electrowetting: from basics to applications. *Journal of Physics: Condensed Matter* 17, R705 (2005).

125. Yamaguchi, S., Morimoto, K., Fukuda, J. & Suzuki, H. Electrowetting-based pH- and biomolecule-responsive valves and pH filters. *Biosensors and Bioelectronics* 24, 2171-2176 (2009).
126. Kwon, G. et al. On-Demand Separation of Oil-Water Mixtures. *Advanced Materials* 24, 3666-3671 (2012).
127. Yi, U.-C. & Kim, C.-J. Characterization of electrowetting actuation on addressable single-side coplanar electrodes. *Journal of Micromechanics and Microengineering* 16, 2053 (2006).
128. Chang, J.-h., Choi, D.Y., Han, S. & Pak, J.J. Driving characteristics of the electrowetting-on-dielectric device using atomic-layer-deposited aluminum oxide as the dielectric. *Microfluidics and Nanofluidics* 8, 269-273 (2010).
129. Kuiper, S. & Hendriks, B. Variable-focus liquid lens for miniature cameras. *Applied physics letters* 85, 1128-1130 (2004).
130. Heikenfeld, J. et al. Electrofluidic displays using Young–Laplace transposition of brilliant pigment dispersions. *Nature Photonics* 3, 292-296 (2009).
131. Yokomaku, H., Satoh, W., Fukuda, J. & Suzuki, H. Electrowetting on gold electrodes with microscopic three-dimensional structures for microfluidic devices. *Journal of applied physics* 104, 064910 (2008).
132. Manukyan, G., Oh, J., Van Den Ende, D., Lammertink, R. & Mugele, F. Electrical switching of wetting states on superhydrophobic surfaces: a route towards reversible Cassie-to-Wenzel transitions. *Physical review letters* 106, 014501 (2011).
133. McHale, G., Herbertson, D., Elliott, S., Shirtcliffe, N. & Newton, M. Electrowetting of nonwetting liquids and liquid marbles. *Langmuir* 23, 918-924 (2007).
134. Oh, J., Manukyan, G., Van den Ende, D. & Mugele, F. Electric-field-driven instabilities on superhydrophobic surfaces. *EPL (Europhysics Letters)* 93, 56001 (2011).
135. Herbertson, D.L., Evans, C.R., Shirtcliffe, N.J., McHale, G. & Newton, M.I. Electrowetting on superhydrophobic SU-8 patterned surfaces. *Sensors and Actuators A: Physical* 130, 189-193 (2006).
136. Revilla, R.I. et al. Electrowetting Phenomenon on Nanostructured Surfaces Studied by Using Atomic Force Microscopy. *The Journal of Physical Chemistry C* 116, 14311-14317 (2012).

137. Berge, B. Electrowetting and wetting of insulator films by water. *Comptes Rendus De L Academie Des Sciences Serie Ii* 317, 157-163 (1993).
138. Quinn, A., Sedev, R. & Ralston, J. Contact angle saturation in electrowetting. *The journal of physical chemistry B* 109, 6268-6275 (2005).
139. Zhu, L. et al. Electrowetting of aligned carbon nanotube films. *The Journal of Physical Chemistry B* 110, 15945-15950 (2006).
140. Masuda, H. & Fukuda, K. Ordered metal nanohole arrays made by a two-step replication of honeycomb structures of anodic alumina. *Science* 268, 1466-1468 (1995).
141. Jessensky, O., Müller, F. & Gösele, U. Self-organized formation of hexagonal pore arrays in anodic alumina. *Applied Physics Letters* 72, 1173-1175 (1998).
142. Kim, S. et al. Fabrication of Metal Nanohoneycomb Structures and Their Tribological Behavior. *Advanced Composite Materials* 17, 101-110 (2008).
143. Drummond, C. Electric-field-induced friction reduction and control. *Physical review letters* 109, 154302 (2012).
144. Park, J.Y., Ogletree, D.F., Thiel, P.A. & Salmeron, M. Electronic Control of Friction in Silicon pn Junctions. *Science* 313, 186 (2006).
145. Sweeney, J. et al. Control of Nanoscale Friction on Gold in an Ionic Liquid by a Potential-Dependent Ionic Lubricant Layer. *Physical Review Letters* 109, 155502 (2012).
146. Goujon, F., Ghoufi, A., Malfreyt, P. & Tildesley, D.J. The kinetic friction coefficient of neutral and charged polymer brushes. *Soft Matter* 9, 2966-2972 (2013).
147. Wang, K., Lee, H., Cooper, R. & Liang, H. Time-resolved, stress-induced, and anisotropic phase transformation of a piezoelectric polymer. *Appl. Phys. A* 95, 435-441 (2009).
148. Hertz, H. Ueber die Berührung fester elastischer Körper. *Journal für die reine und angewandte Mathematik* 92, 156-171 (1882).
149. Choi, D. et al. Dependence of adhesion and friction on porosity in porous anodic alumina films. *Scripta Materialia* 58, 870-873 (2008).
150. Thomann, G.B.a.Y. Characterization of the Morphologies and Nanostructures of Blends of Poly(styrene)-block-poly(ethene-co-but-1-ene)-block-poly(styrene)

with Isotactic and Atactic Polypropylenes by Tapping-Mode Atomic Force Microscopy. *Langmuir* 14 (1998).

151. Bryan B. Sauer, R.S.M., and Richard R. Thomas Tapping Mode AFM Studies of Nano-Phases on Fluorine-Containing Polyester Coatings and Octadecyltrichlorosilane Monolayers. *Langmuir* 14 (1998).
152. M. R. Vanlandingham, R.F.E., and J. W. Gillespie Relationships between Stoichiometry, Microstructure, and Properties for Amine-Cured Epoxies. *Journal of Applied Polymer Science* 71 (1999).
153. Ishizaki, K., Komarneni, S. & Nanko, M. in *Porous Materials 1-11* (Springer, 1998).
154. Ong, Y.-L., Razatos, A., Georgiou, G. & Sharma, M.M. Adhesion Forces between *E. coli* Bacteria and Biomaterial Surfaces. *Langmuir* 15, 2719-2725 (1999).
155. Fällman, E. et al. Optical tweezers based force measurement system for quantitating binding interactions: system design and application for the study of bacterial adhesion. *Biosensors and Bioelectronics* 19, 1429-1437 (2004).
156. Beloin, C., Houry, A., Froment, M., Ghigo, J.-M. & Henry, N. A short-time scale colloidal system reveals early bacterial adhesion dynamics. *PLoS biology* 6, e167 (2008).
157. Pourshafie, M.R., Marklund, B.-I. & Ohlson, S. Binding interactions of *Escherichia coli* with globotetraosylceramide (globoside) using a surface plasmon resonance biosensor. *Journal of microbiological methods* 58, 313-320 (2004).
158. Agladze, K., Wang, X. & Romeo, T. Spatial periodicity of *Escherichia coli* K-12 biofilm microstructure initiates during a reversible, polar attachment phase of development and requires the polysaccharide adhesin PGA. *Journal of bacteriology* 187, 8237-8246 (2005).
159. Blossey, R. Self-cleaning surfaces—virtual realities. *Nature materials* 2, 301-306 (2003).
160. Tanahashi, I., Yoshida, A. & Nishino, A. Electrochemical Characterization of Activated Carbon-Fiber Cloth Polarizable Electrodes for Electric Double-Layer Capacitors. *Journal of The Electrochemical Society* 137, 3052-3057 (1990).
161. Ren, X. & Pickup, P.G. Ion transport in polypyrrole and a polypyrrole/polyanion composite. *The Journal of Physical Chemistry* 97, 5356-5362 (1993).

162. MacFarlane, D., Meakin, P., Sun, J., Amini, N. & Forsyth, M. Pyrrolidinium imides: a new family of molten salts and conductive plastic crystal phases. *The Journal of Physical Chemistry B* 103, 4164-4170 (1999).
163. Jeong, H. et al. Enhancing the Charge Transfer of the Counter Electrode in Dye-Sensitized Solar Cells Using Periodically Aligned Platinum Nanocups. *Small* 8, 3757-3761 (2012).
164. Weininger, J.L. & Breiter, M.W. Effect of Crystal Structure on the Anodic Oxidation of Nickel. *Journal of The Electrochemical Society* 110, 484-490 (1963).
165. Fleischmann, M., Korinek, K. & Pletcher, D. The oxidation of organic compounds at a nickel anode in alkaline solution. *Journal of Electroanalytical Chemistry and Interfacial Electrochemistry* 31, 39-49 (1971).
166. Skowronski, J. & Wazny, A. Nickel Foam-based Ni(OH)₂/NiOOH Electrode as Catalytic System for Methanol Oxidation in Alkaline Solution. *Journal of New Materials for Electrochemical Systems* 9, 345 (2006).
167. Lee, S.W. et al. High-power lithium batteries from functionalized carbon-nanotube electrodes. *Nature Nanotechnology* 5, 531-537 (2010).
168. Wang, H. & Pilon, L. Physical interpretation of cyclic voltammetry for measuring electric double layer capacitances. *Electrochimica Acta* 64, 130-139 (2012).
169. Kalu, E., Nwoga, T., Srinivasan, V. & Weidner, J. Cyclic voltammetric studies of the effects of time and temperature on the capacitance of electrochemically deposited nickel hydroxide. *Journal of power sources* 92, 163-167 (2001).
170. Biesheuvel, P., Fu, Y. & Bazant, M.Z. Diffuse charge and Faradaic reactions in porous electrodes. *Physical Review E* 83, 061507 (2011).
171. Kim, Y.-T., Tadai, K. & Mitani, T. Highly dispersed ruthenium oxide nanoparticles on carboxylated carbon nanotubes for supercapacitor electrode materials. *Journal of Materials Chemistry* 15, 4914-4921 (2005).
172. Chapman, D.L. LI. A contribution to the theory of electrocapillarity. *The London, Edinburgh, and Dublin Philosophical Magazine and Journal of Science* 25, 475-481 (1913).
173. Helmholtz, H.v. Studien über elektrische Grenzschichten. *Annalen der Physik* 243, 337-382 (1879).

174. Gouy, M. Sur la constitution de la charge électrique à la surface d'un électrolyte. *J. Phys. Theor. Appl.* 9, 457-468 (1910).
175. Stern, O. Zur theorie der elektrolytischen doppelschicht. *Zeitschrift für Elektrochemie und angewandte physikalische Chemie* 30, 508-516 (1924).
176. Chang, C. & Yang, R.-J. Computational analysis of electrokinetically driven flow mixing in microchannels with patterned blocks. *Journal of Micromechanics and Microengineering* 14, 550 (2004).
177. Yoon, C.H., Vittal, R., Lee, J., Chae, W.-S. & Kim, K.-J. Enhanced performance of a dye-sensitized solar cell with an electrodeposited-platinum counter electrode. *Electrochimica Acta* 53, 2890-2896 (2008).
178. Buijnsters, J.G., Zhong, R., Tsyntaru, N. & Celis, J.P. Surface wettability of macroporous anodized aluminum oxide. *ACS applied materials & interfaces* 5, 3224-3233 (2013).
179. Leese, H., Bhurtun, V., Lee, K.P. & Mattia, D. Wetting behaviour of hydrophilic and hydrophobic nanostructured porous anodic alumina. *Colloids and Surfaces A: Physicochemical and Engineering Aspects* 420, 53-58 (2013).
180. Johnson Jr, R.E. & Dettre, R.H. Contact angle hysteresis. III. Study of an idealized heterogeneous surface. *The Journal of Physical Chemistry* 68, 1744-1750 (1964).
181. Kim, D., Kim, J. & Hwang, W. Prediction of contact angle on a microline patterned surface. *Surface science* 600, L301-L304 (2006).
182. Zu, Y., Yan, Y., Li, J. & Han, Z. Wetting behaviours of a single droplet on biomimetic micro structured surfaces. *Journal of Bionic Engineering* 7, 191-198 (2010).
183. Ran, C., Ding, G., Liu, W., Deng, Y. & Hou, W. Wetting on Nanoporous Alumina Surface: Transition between Wenzel and Cassie States Controlled by Surface Structure. *Langmuir : the ACS journal of surfaces and colloids* 24, 9952-9955 (2008).
184. Yang, J. et al. Intermediate wetting states on nanoporous structures of anodic aluminum oxide surfaces. *Thin Solid Films* (2014).
185. Young, T. An essay on the cohesion of fluids. *Philosophical Transactions of the Royal Society of London*, 65-87 (1805).

186. Wenzel, R.N. Surface roughness and contact angle. *The Journal of Physical Chemistry* 53, 1466-1467 (1949).
187. Yokomaku, H., Satoh, W., Fukuda, J. & Suzuki, H. Electrowetting on gold electrodes with microscopic three-dimensional structures for microfluidic devices. *Journal of Applied Physics* 104 (2008).
188. Herbertson, D.L., Evans, C.R., Shirtcliffe, N.J., McHale, G. & Newton, M.I. Electrowetting on superhydrophobic SU-8 patterned surfaces. *Sensors and Actuators A: Physical* 130–131, 189-193 (2006).
189. Quilliet, C. & Berge, B. Electrowetting: a recent outbreak. *Current Opinion in Colloid & Interface Science* 6, 34-39 (2001).
190. Mateo, J.N. et al. Wetting behavior of polymer coated nanoporous anodic alumina films: transition from super-hydrophilicity to super-hydrophobicity. *Nanotechnology* 22, 035703 (2011).
191. Feng, L. et al. Petal Effect: A Superhydrophobic State with High Adhesive Force. *Langmuir* 24, 4114-4119 (2008).